

Design and Construction of a Low-Temperature Scanning Tunneling Microscope for Spectroscopic Applications on Model Catalysts

vorgelegt von
Dipl.-Phys.
Stefan Ulrich
aus Wolfsburg

von der Fakultät II – Mathematik und Naturwissenschaften
der Technischen Universität Berlin
zur Erlangung des akademischen Grades

Doktor der Naturwissenschaften
- Dr.rer.nat -
genehmigte Dissertation

Promotionsausschuss

Vorsitzender: Prof. Dr. Michael Lehmann

Gutachter: Prof. Dr. Hans-Joachim Freund

Gutachter: Prof. Dr. Mario Dähne

Tag der wissenschaftlichen Aussprache: 24.Oktober 2012

Berlin 2013

D 83

In Erinnerung an meine Eltern

Die vorliegende Dissertation wurde im Zeitraum Juni 2004 bis August 2008 in der Abteilung Chemische Physik am Fritz-Haber-Institut der Max-Planck-Gesellschaft unter der Anleitung von Herrn Prof. Dr. H.-J. Freund angefertigt.

Zusammenfassung

Im Mittelpunkt dieser Arbeit steht die Funktionalisierung der Oberflächen dünner Oxid-Filme, synthetisiert auf leitenden, kristallinen Trägern, sowohl intrinsisch als Konsequenz des Filmwachstums als auch extrinsisch durch kontrolliertes Einbringen von Adsorptionszentren. Die Oberflächen werden mittels Rastertunnelmikroskopie, Rastertunnelspektroskopie und Leitfähigkeits-Konturbildern untersucht. Zusätzlich werden Resultate von Modellrechnungen basierend auf der Dichte-Funktional Theorie präsentiert.

Eine neue Messapparatur wurde entwickelt und in Betrieb genommen. Besondere Berücksichtigung findet dabei die Kombination von tiefen Temperaturen und einem außergewöhnlich guten Zugang zur Probe. Hohe thermische Stabilität und geringer Kryogenkonsum ermöglichen Untersuchungen an derselben Probe über lange Zeiträume hinweg. Des weiteren erlaubt die Apparatur das schrittweise Hinzufügen weiterer Analysemöglichkeiten bei unveränderter Probenposition im Mikroskop.

Es wurden signifikante Veränderungen in der Oberflächenmorphologie während der Oxidation von gestuftem NiAl(16 14 1) im Vergleich zum üblichen NiAl(1 1 0) Substrat beobachtet. Die regelmäßige Sequenz von (1 1 0) Terrassen ist zugunsten von großen, trigonalen Ebenen aufgehoben, deren durchschnittliche Größe von Verspannungen im Alumina-Film aufgrund der Gitterfehlpassung bestimmt wird. Die asymmetrische Anordnung der mittleren Stufen-ausrichtung gegenüber den Reflexionsdomänen des Aluminiumoxides führen hierbei zu einem besonders effizienten Spannungsabbau für eine Richtung. Daraus ergibt sich die bevorzugte Bildung einer bestimmten Domäne.

Des weiteren wird ein zweidimensionales, poröses System vorgestellt ($\text{SiO}_2/\text{Mo}(1\ 1\ 2)$), das in der Lage ist, den Zugang bestimmter atomarer Spezies zu einer reaktiven Oberflächenregion via Nano-Poren in der innerten obersten Lage zu kontrollieren. Wir demonstrieren die größenabhängige Adsorptionscharakteristik des ultra-dünnen SiO_2 -Films auf $\text{Mo}(1\ 1\ 2)$ für Pd, Ag und Au Atome. Während Pd Atome in der Lage sind, die Öffnungen in der obersten Silica Schicht ohne nennenswerte Barriere zu durchdringen, erfahren Ag Atome eine mäßige und Au Atome eine unüberwindbare Barriere an der Oxidoberfläche. Die Penetrationswahrscheinlichkeit korreliert dabei nicht mit der effektiven Größe des Atoms, sondern ist von der elektronischen Struktur abhängig. Dabei hat Pd mit unbesetztem Valenz-s-Orbital eine geringe Penetrationsbarriere, während Ag und Au mit besetztem s-Zustand eine erhebliche Repulsion erfahren, was zu einer erhöhten Aktivierungsenergie für den Durchtritt führt. Im Falle von Ag kann die Barrierenhöhe zeitweise durch die Promotion des Ag 5s-Elektrons in das Substrat verringert werden. Der Molybdän-getragene Silica-Film kann daher als einfache Form eines Molekularsiebs angesehen werden, dessen Selektivität auf der elektronischen Struktur der Ad-Atome beruht.

Der Einbau einzelner Pd Atome in die Nano-Poren des Silica-Films auf $\text{Mo}(1\ 1\ 2)$ verändert die Adoptionseigenschaften des Oxid-Materials. Das Pd erlaubt es, weitere Metallatome zu verankern, die ansonsten nicht an die innerte Silica Oberfläche binden würden. Mehrere Absorptionsverbindungen, Pd-Pd, Pd-Ag und Pd-Au wurden auf diese Weise präpariert und analysiert. Die Bindungsstärker der Ad-Atome an die Oberfläche wird dabei im Wesentlichen von den Frontier-Orbitalen bestimmt, die eine repulsive Komponente in die Wechselwirkung mit den elektronischen Zuständen des Oxids einbringen, was zu einer Schwächung der kova-

lenten Bindung zum Pd Anker führt.

Schlüsselwörter: Rastertunnel-Mikroskopie, Rastertunnel-Spektroskopie, Leitfähigkeits-Konturbilder, Vizinalflächen, Aluminiumoxid, Siliziumoxid, Molekularsieb.

Abstract

The functionalization of surfaces of thin oxide films, synthesized on conductive, crystalline supports either intrinsically as consequence of the film growth or extrinsically by controlled insertion of adsorption centers is the focus of this study. The surfaces are investigated by scanning tunneling microscopy, scanning tunneling spectroscopy and conductance mapping. Results from auxiliary model calculations based on density functional theory are presented as well.

A new experimental setup was designed and commissioned. A novelty of the design is the combination of low temperatures and exceptionally good accessibility of the sample. High thermal stability and low cryogen consumption enables investigations on the same sample for extended periods of time. Additionally, the setup allows for the successive implementation of additional analytic equipment at unchanged sample position within the microscope.

Significant changes of the surface morphology were observed during the oxidation of stepped NiAl(16 14 1) compared to the common NiAl(1 1 0)-substrate. The regular sequence of vicinal (1 1 0)-terraces is lifted in favor of large, triangular planes, in which mean size is determined by the lattice-mismatch induced strain that accumulates within the thin alumina film. The asymmetry of the mean step direction with respect to the reflection domains of the aluminum oxide leads to an efficient strain relief in one particular direction, resulting in the preferred formation of one domain.

Furthermore, a two-dimensional counterpart of a molecular sieve that is capable of controlling the access of distinct atomic species to a reactive surface region via nano-pores in the inert top layer is introduced. We demonstrate the size-specific adsorption characteristics of the ultra-thin, porous SiO₂ film on Mo(1 1 2) for Pd, Ag, and Au atoms. While Pd atoms are able to penetrate the holes in the silica top-layer with virtually no barrier, Ag atoms experience an intermediate barrier value and Au atoms are completely unable to pass the oxide surface. The penetration probability does not correlate with the effective size of the atom, but depends on their electronic structure. Whereas Pd with an unoccupied valence s-orbital has a low penetration barrier, Ag and Au atoms with occupied s-states experience a substantial repulsion from the filled oxide states, leading to a higher barrier for penetration. In the case of Ag, the barrier height can be temporarily lowered by promoting the Ag 5s electron into the substrate. The Mo-supported silica film can thus be considered a primitive form of an atomic sieve whose selectivity is governed by the electronic structure of the ad-atoms.

The embedding of single Pd atoms into the nano-pores of thin silica films on Mo(1 1 2) alters the adsorption properties of the oxide material. The Pd is able to anchor additional metal atoms that would not bind to the inert silica surface otherwise. Several adsorption complexes, Pd-Pd, Pd-Ag and Pd-Au have been prepared and analyzed this way. The binding strength of the ad-atoms to the surface is determined by the number of electrons in their frontier orbitals, which introduce a repulsive interaction with the oxide electronic states and weaken the covalent bond to the Pd anchor.

Key words: Scanning Tunneling Microscopy, Scanning Tunneling Spectroscopy, conductance mapping, vicinal surfaces, aluminum oxide, silicon oxide, molecular sieve.

Contents

1	Introduction	1
2	Description of the Experimental Methods	7
2.1	Scanning Tunneling Microscopy	7
2.2	Scanning Tunneling Spectroscopy	11
2.2.1	Spectroscopy Based on Elastic Tunneling	12
2.2.2	Inelastic Electron Tunneling Spectroscopy	15
3	Construction of a Low Temperature Scanning Tunneling Microscope	21
3.1	Design Criteria	21
3.2	The Setup	22
3.2.1	The Microscope	22
3.2.2	The Control Electronics	28
3.2.3	The UHV System	29
3.2.4	The Preparation Chamber	37
3.3	Performance	41
3.3.1	Mechanical and Thermal Stability	41
3.3.2	Imaging and Spectroscopies	44
4	The Influence of Substrate Steps on Oxide Formation	49
4.1	Introduction	49
4.2	The Growth of Aluminum Oxide on a Regular NiAl (110) Surface	51
4.2.1	The Oxide Structure	51
4.2.2	Typical Defects in the Oxide	53
4.3	The Formation of Aluminum Oxide on a NiAl(16 14 1) Vicinal Surface	56
4.3.1	Introducing the NiAl (16 14 1) Vicinal Surface	56
4.3.2	An Oxide Induced Surface Reconstruction	58
4.3.3	Oxide Nucleation and Growth	60
4.3.4	Controlled Alteration of the Alumina Domain Distribution	62
4.4	Conclusions	65
5	A Size-Selective Adsorption Mechanism: Metal Atoms on SiO₂ Thin Films	67
5.1	Introduction	67

5.2	Synthesis of Silicon Oxide on Mo(112)	68
5.2.1	Sample Preparation	68
5.2.2	Atomic and Electronic Structure of the Silica Film	71
5.3	Application of an Ultra-thin Silica Film as Atomic Sieve	81
5.4	Creating Anchoring Sites for Metal Atoms on the Silica Film	95
5.5	Conclusions	103

Bibliography	105
---------------------	------------

Appendix	119	
1	List of Abbreviations	121
2	Conductance Maps Color Scheme	123
3	Publications	125
4	Danksagung	127
5	Selbständigkeitserklärung	129

List of Figures

1.1	Portrayal of a model catalyst depicting potentially size-dependent effects.	3
2.1	Illustration of a tunneling junction, depicting a small atomic cluster as probe, a single crystal surface as sample, the tunneling gap width z , the bias voltage U_B and the tunneling current I_T .	8
2.2	Schematic of the density of states (DOS) of probe and sample for a biased tunneling junction. It is the convention that the polarity of the voltage refers to the sample side, hence, a negative bias leads to tunneling from the sample into the probe.	10
2.3	Field emission resonances within a tunneling junction: (a) Potential diagram of the gap indicating the states $n=1$ and $n=2$ above the vacuum level. (b) Measurements of field-emission resonances that form between a PtIr tip and a $\text{SiO}_2\text{-Mo}(1\ 1\ 2)$ surface (see Cha. 5).	15
2.4	Inelastic electron tunneling spectroscopy: (a) Schematic of inelastic electron energy transfer the within the tunneling gap due to the excitation of a vibration. (b) The resulting current increases due to the opening of another tunneling channel at the excitation energy $\hbar\omega/e$ and (c) how this onset translates into a peak of the second derivative of the current.	16
3.1	Model of the scan-head depicting the tripple-helix sampleholder with an inclination of $1\ \text{mm}/120^\circ$ (A), a sample (B), three steel balls to support and contact the sample holder (C), sapphire isolators (D), three piezo-legs for support and offsets (E), the tip (F), the tip-holder (G), the scan-piezo (H) and the base plate (I).	23
3.2	Eigenfrequencies of the scan-head. Left: resonances of the tube-scanner with and without tip holder. Right: resonances of an outer piezo-leg while supporting the weight of the sample holder. For the upper curve excitation as well as response are measured at the same piezo-element while for the lower curve two different elements are used.	24

3.3	Microscope assembly underneath the cryostat, including the vibration isolation: cold plate of the liquid-helium cryostat (A), spring connector (B), suspension-spring (C), microscope base-plate (D), eddy-current damping unit (E), clamping screw for fixing and cooling the microscope (F), electrical connections (G), the scan-head (H), wires (I), ceramics for heat-sinking and isolating the wire connections (J), shielded wire for the tunneling current (K).	27
3.4	Schematic of the control electronics: current set point (green), feedback-loop (blue), microscope (gray), bias and bias-modulation (red + orange), A/D conversion and data processing (yellow)	28
3.5	The UHV system: cryostat (A), experimental (STM) chamber (B), preparation chamber (C), main manipulator (D) ion-pump and Ti-sublimation pump (E), turbo-molecular pump (F), air-leg (G).	30
3.6	Cutaway view of the microscope inside the radiation shields and the pathways for different experimental applications.	31
3.7	Positions of the experimental applications and components on the STM chamber: port for connecting the electron energy-analyzer (A), optical lens-assembly for photon collection from the tunneling junction (B), metal evaporator (C), gas-doser (D), window for coupling to a laser (E), metal evaporator (F), wobble stick (G), main view-port (H).	33
3.8	Bottom view of the microscope inside the radiation-shields (shield end-plates removed): liquid-nitrogen cooled shield (A), liquid-helium cooled shield (B), cryostat cold-plate (C), magnet array for eddy-current damping (D), microscope base-plate (E), anchor for cooling and clamping.	34
3.9	The main manipulator: sample-holder with hook (A), locking mechanism to fix the sample during manipulator rotation (B), copper element (C), Kapton-isolated wires for low- and high-voltages (D), tank for cooling with liquid nitrogen (E), tungsten-filament for heating (F), capillary for cryogen supply (G), support tube (H).	38
3.10	Tip exchange with the manipulator: (a) View through the window inside the radiation-shields onto the tip carrier and the manipulator end-piece, (b) the manipulator in orientation to perform a tip exchange, holding a tip carrier.	39
3.11	(a) Sample preparation stage: high voltage supply (A), tungsten-filament (B) sample holder (C), molybdenum plate to support and protect the sample holder (D), manipulator end-piece (E), four-pocket evaporator (F) filled with Fe (G), Ag (H), Si (I) and Au (K), capillary for oxygen dosing (L). (b) Preparation-stage in heating mode.	40
3.12	Cool-down characteristic of the scan-head from of 130 K to 9 K.	41

3.13	Spectral analysis (FFT) of the tunneling current in the range of 0-6000 Hz with and without vibration isolation, showing the impact of mechanical and acoustical excitations on the stability of the tunneling junction: (a) The spring-suspension is locked and the air-legs are deflated. (b) The spring-suspension is locked and the air-legs are active. (c) Both isolation stages are active.	43
3.14	Thermal and mechanical stability of the tunneling junction at 9.5 K. After stabilizing the current at 32 pA the feedback-loop was disabled and the current monitored for 600 s. The change of the average current is less than 1 pA over the entire time interval. Both vibration-isolation stages were active.	44
3.15	Microscope performance regarding imaging and spectroscopy: (a) Atomic resolution of NiAl (110), image: $3.5 \times 3.5 \text{ nm}^2$, $U_b = +240 \text{ mV}$, $I_T = 560 \text{ pA}$ (b) Surface state on NiAl(110), image: $10 \times 10 \text{ nm}^2$ (c) The same surface state in k-space [Fourier-transform of (b)] (d) Ag atoms on NiAl(110), image: $28 \times 28 \text{ nm}^2$, $U_b = +760 \text{ mV}$, $I_T = 124 \text{ pA}$ (e) formation of Ag and Ag-CO after CO dosing (f) Scanning tunneling spectroscopy (dI/dV) of silver atoms and carbonyls (AgCO). (g) Vibrational spectroscopy (d^2I/dV^2) of silver carbonyls.	45
4.1	Nucleation of palladium atoms along the antiphase domain boundaries of Al_2O_3	49
4.2	Topography, LEED and model of alumina grown on NiAl(110): (a) STM image ($90 \times 90 \text{ nm}$) promoting the APDB and their orientation with respect to the crystallographic directions of the substrate. (b) Model of the Al_2O_3 unit cells and their appearance in LEED (insert).	52
4.3	Model of the NiAl(16 14 1) vicinal surface, consisting of narrow terraces with (1 1 0) orientation, separated by mono-atomic steps.	56
4.4	Schematic representation of the step orientation with respect to the oxide domains of the original film. The shorter side of the unit cell of type A is almost parallel to the step direction.	56
4.5	Comparison of topography and LEED between the NiAl(1 1 0) and the NiAl(16 14 1) surfaces. The LEED images are aligned to the crystallographic directions of the STM images: (a) NiAl(1 1 0), $40 \times 40 \text{ nm}^2$, $U_B = 0.32 \text{ V}$, $I_T = 0.5 \text{ nA}$. (b) NiAl(16 14 1), $40 \times 40 \text{ nm}^2$, $U_B = 0.85 \text{ V}$, $I_T = 0.6 \text{ nA}$. The LEED spots split due to the proximity of the steps	57
4.6	Morphological alteration of the NiAl vicinal surface by exposure to oxygen: the pristine surface (a, d), after exposure to 60 L O_2 (b, e) and after exposure to 1200L O_2 (c, f). Upper row: STM images, measured at 80 K (a) $100 \times 100 \text{ nm}^2$ and (b-c) $200 \times 200 \text{ nm}^2$. The tunneling parameters are $U_B = 4.5 \text{ V}$ and $I_T = 0.1 \text{ nA}$. Lower row: step with distribution, each referring to the STM image above.	58

4.7	Nucleation of alumina on a NiAl(16 14 1) vicinal surface after dosage of 60 L O ₂ (a) Overview, 200 x 200 nm ² . (b) and (c) close-up images, 45 x 45 nm ² . U _B = 4.0 V, I _T = 0.1 nA	61
4.8	STM topographic images after oxidation with 1200 L O ₂ and the corresponding LEED: (a) NiAl(1 1 0), 80 x 80 nm ² . (b) NiAl(16 14 1), 50 x 50 nm ² . (c) LEED of the sample (a) with indication of both oxide domains. (d) LEED of the sample (b) with one dominating reflection domain (A).	63
5.1	Model of a porous Zeolite surface.	67
5.2	Topography and geometry of the pristine Mo(1 1 2) surface. Left: STM (95 x 95 nm ² ; U _B = + 1310 mV; I _T = 42 pA); middle: model of the atomic configuration of the topmost layers; right: corresponding unit cell vectors.	69
5.3	The Evolution of LEED during the silica preparation (electron energy 45-60 eV) . Left to right: clean Mo(112); O ₂ chemisorbed at 700 K; SiO ₂ -Mo(1 1 2); SiO ₂ -Mo(1 1 2) + MoO _x	70
5.4	Structural and LDOS changes of the silica surface after annealing to 1280K for 300 s. Topography: 30 x 30 nm ² ; U _B = + 300 mV; I _T = 52 pA. The cross section along the dotted line illustrates the film buckling. Middle and lower row: conductance maps of the same surface area at bias voltages from + 1.2 V to + 4.3 V. For color code see appendix. . .	72
5.5	High resolution STM image and model of silica grown on Mo(112): (a) 5.2 x 5.2 nm ² ; U _B = + 990 mV; I _T = 40 pA (b) Model of the atomic arrangement within the silica layer.	73
5.6	Additional representations of the SiO ₂ -Mo(1 1 2) surface at varying imaging conditions. (a) 6.7 x 6.7 nm ² ; U _B = + 30 mV; I _T = 65 pA (b) 8.9 x 8.9 nm ² ; U _B = + 2074 mV; I _T = 40 pA (c) 6.2 x 6.2 nm ² ; U _B = - 510 mV; I _T = 11 pA.	74
5.7	Typical defects of the SiO ₂ -Mo(1 1 2) surface. (a) Domain boundaries along the $[\bar{1} 1 0]$ direction representing the Si atoms (2.9 x 2.9 nm ² ; U _B = + 990 mV; I _T = 40 pA) (b) APDB similar to (a) representing the O atoms instead (2.9 x 2.9 nm ² ; U _B = + 30 mV; I _T = 65 pA) (c) Model for (a+b), Si atoms show in yellow, O atoms in red (d) Domain boundaries along the $[\bar{1} \bar{1} 1]$ with unresolved atomic structure; diamonds indicate the preservation of the pore geometry (8.9 x 8.9 nm ² ; U _B = + 990 mV; I _T = 21 pA).	75
5.8	Photo-electron spectra of the SiO ₂ -Mo(112) film for the O 1s and the Mo 3d regions acquired with beam energies of 630 eV and 330 eV, respectively. The upper (red) curve shows the result for an incident beam normal to the surface. The lower (blue) curve was measured at a beam angle of 80° with regards to the surface normal.	76

5.9	Tunnel-spectroscopy of the band-gap region of the SiO ₂ -Mo(1 1 2) surface, probing (a) the valence band, made up from O 2 <i>p</i> states and (b) the conduction band, made up from Si 3 <i>s, p</i> states. The signal between - 2.8 V and + 2.3 V did not indicate the presence of additional states and has therefore been omitted in the graph.	78
5.10	(a) NEXAFS spectrum of the silica film at energies of the oxygen K-edge. The E-field vector of the synchrotron light was parallel to the $[\bar{1}10]$ direction. (b) Model calculations of unoccupied states. Within this work, only the 2D-network model has been considered. Both, the measured and the computed spectra display an onset at around 2.5 eV, followed by a larger peak ranging from approx. 4.5 eV to 10 eV.	79
5.11	Characteristic appearance of the silica surface after the deposition of Au (left), Pd (right) and Ag (middle). Displayed are Au : 20 x 20 nm ² , U _B = +1800 mV, I _T = 20 pA, Pd : 22 x 22 nm ² , U _B = +1124 mV, I _T = 40 pA, Ag : 20 x 20 nm ² , U _B = +2000 mV, I _T = 20 pA.	82
5.12	Pd : Bias dependent topography for Pd on the silica film. (a-c) STM images (6.5 x 6.5 nm ² , I _T = 40 pA) acquired at three different bias voltages. (d-f) Computed images (1.8 x 1.5 nm ²) based on the Tersoff-Haman method for the same voltages.	83
5.13	Ag : Bias dependent topography for Ag on the silica film. (a-b) STM images (6.5 x 6.5 nm ² , I _T = 30 pA) acquired at two different bias voltages. (c-d) Computed images (1.8 x 1.5 nm ²) for small negative and positive bias voltages.	85
5.14	Au : Bias dependent topography for Au on the silica film. (a-c) STM images (5.5 x 5.5 nm ² , I _T = 32 pA) acquired at three different bias voltages. The circle indicates a singly and the square a doubly filled oxide pore. (d-f) Computed images (2.2 x 1.3 nm ²) with V _B = 0.8 V for the Au ₁ and with V _B = 0.8 V/1.6 V for the Au ₂ species.	86
5.15	Potential-energy curves describing the energetic conditions at different stages of the adsorption process for Au (left), Pd (right) and Ag (middle). Each curve starts to the left with the binding energy on top of the oxide surface, followed by the potential barrier for film penetration and ending with the binding at the interface. All energies are given with respect to a gas-phase atom. For each element, models of two binding configurations are inserted at the upper part of the image: on top of the film (left) and at the interface (right). The Bader charges that occur during the penetration are added in parenthesis.	87

5.16	Conductance maps of Pd (top, 13 x 13 nm ² , I _T = 50 pA) and Ag (bottom, 12 x 12 nm ² , I _T = 32 pA) after incorporation into the silica surface, each at three different bias voltages. Pd reaches the maximum of the conductance at U _B = + 2.2 V. For Ag, the maximum is with U _B = + 2.0 V at a slightly lower energy. No features were observed for spectroscopy at negative bias voltages. For color code see appendix . . .	90
5.17	DFT calculations of the LDOS for the Pd-SiO ₂ -Mo(1 1 2) system (left) and the Au-SiO ₂ -Mo(1 1 2) system (right). Each series displays the LDOS layer by layer, starting with the results for the surface oxygen (top), followed by the interface oxygen (middle row) and the Mo-interface (bottom). The proximity of the surface O 2 <i>p</i> states and the Pd 5 <i>s</i> state result in a hybridization that leads to the characteristic contrast in STM images. The position of the Pd at the interface is shown in the insert. The scenario is very different for the Au species. The 6 <i>s</i> states overlap very little with any of the oxide states which leads to a small hybridization that does not contribute significantly to the LDOS. The situation is the same for either a singly or doubly occupied oxide pore (lower right). The binding positions and the respective color-code are given in the upper two inserts for Au ₁ and in the lower one for Au ₂ species.	91
5.18	Incorporation of Au into the defective oxide opening. The -Si-O- octagon is widened by a reduced hybridization of the Si and O states, which leads to the characteristic contrast in STM. The computed rearrangement of the individual atoms upon Au adsorption is indicated in the image.	92
5.19	(a) Calculated LDOS of the pristine silica film (gray) and of the hybrid states formed between the respective <i>s</i> -orbitals of incorporated Pd, Ag and Au atoms and the O 2 <i>p</i> states of the surface oxygen. (b) Tunneling spectroscopy performed in the energy range between 1.0 eV and 3.1 eV, showing the dI/dV spectra of the pristine oxide film and the states resulting from Pd and Ag insertion. The Pd-induced state appears less pronounced due to the increased LDOS of the silica-film itself.	93
5.20	Topographic images of SiO ₂ /Mo(1 1 2) after successive deposition of Pd and (a) Pd, 14 x 14 nm ² , U _B = + 550 mV, I _T = 26 pA, (b) Ag, 20 x 20 nm ² , U _B = + 3390 mV, I _T = 33 pA, (c) Au, 10 x 10 nm ² , U _B = - 325 mV, I _T = 34 pA. For each case new features become visible, marked by arrows, that differ significantly from the deposition of a single element only. The insert in (a) shows the model of the initial Pd incorporation.	96

5.21	Dissociation of a Pd-Pd dimer by a voltage pulse applied with the STM tip. (a) Initial topography, displaying four Pd dimers. $10 \times 10 \text{ nm}^2$, $U_B = + 1360 \text{ mV}$, $I_T = 31 \text{ pA}$. (b) The same surface section after application of $U_B = + 4.5 \text{ V}$ for 10 ms to the feature marked by the square. The dimer disappeared, and an area with several embedded Pd appears. (c) The same image taken at a lower bias voltage ($+ 1010 \text{ mV}$). The reduced contrast allows to pinpoint the adsorption site which is evidently on top of a Pd_{sub}	97
5.22	(a) Calculated LDOS of the pristine silica film (gray) and the respective dimers (colored lines). The spectra depict the contribution of the Au 6s (red), the Ag 5s (blue) and the Pd 5s (green) to the hybrid state that forms with the O 2p orbitals, when the respective ad-atom binds to the Pd_{sub} -anchor. (b) Spectroscopic results for the energy range between 1.0 - 2.8 eV, showing dI/dV spectra of a Pd-Pd _{sub} complex (red), an Au-Pd _{sub} complex (orange), the Pd _{sub} anchors (blue/green) and the plain oxide film (dashed line)	98
5.23	Topography and conductance map series of a Pd-Pd _{sub} complex. The topography is shown at the upper left corner ($10 \times 10 \text{ nm}^2$, $U_B = - 500 \text{ mV}$, $I_T = 32 \text{ pA}$). The conductance maps show an increase in the corona region of the feature between 1.4 V and 1.6 V and a pronounced maximum at $\approx 1.8 \text{ V}$	101
5.24	Topography and conductance map series of an Au-Pd _{sub} complex. The topography is shown at the upper left corner ($6 \times 6 \text{ nm}^2$, $U_B = + 1210 \text{ mV}$, $I_T = 35 \text{ pA}$). In addition to the Au-Pd _{sub} feature, the presence of a Pd _{sub} is indicated to serve as reference. The conductance maps present the most significant changes in the range from -0.4 V to + 2.2 V. The increase of the conductance at -0.3 V and + 1.6 V in the center region of the Au feature denotes the occurrence of two intrinsic states, while the ring-like conductance enhancement between $\approx 1.0 \text{ V}$ and 1.5 V originates from the widening of the oxide pore upon Au adsorption. .	102

List of Tables

3.1 Positions of the openings within the radiation shields to access the sample inside the cryostat. 32

1 Introduction

For many years complex catalytic systems have been successfully investigated in form of model systems. In this case a three dimensional oxide matrix of the actual catalysts is reduced to a planar and ideally single-crystalline oxide film. The distinct adsorption and reaction behavior of small metal particles dispersed over the oxide surface dominates the catalytic characteristics of the system.

Early studies that utilized the surface-science approach for catalysts have been carried out as of the 1960's, beginning with reactions on single-crystal metal surfaces like the oxidation of carbon monoxide on a palladium(110) surface [1], hydrogenolysis of cyclopropane on a platinum stepped single-crystal [2] and hydrogen adsorption on platinum(111) [3]. In spite of their relevance, these studies bypassed the role of the structure of the active surface, e.g. the presence of nanoparticles and their interactions with the oxide substrate.

A greater sensitivity for structure-related attributes was achieved by the deposition of metal clusters onto metal-oxide single-crystals. Since many of the methods used in surface science are based on electron or ion spectroscopy, reasonably conductive samples are required for the experiments to prevent charging, which would alter the results significantly. One intensely studied bulk material is TiO_2 which becomes an n-type semiconductor after annealing to ≈ 1000 K [4]. Another suitable material is ZnO with a band gap at the border between semiconductor and insulator, where a sufficient conductivity can be induced by reduction and annealing. A number of oxides have been studied in this context, including Cr_2O_3 , NiO , and SnO_2 . Insulators like Al_2O_3 , MgO , and SiO_2 can still be investigated with infrared-reflection-absorption spectroscopy (IRAS) or thermal desorption spectroscopy (TDS), but most of the common surface science methods can not be employed.

Consequently, it was imperative to model the oxide support in a way that the charging effects could be avoided. This problem was solved by introducing thin metal-oxide films, grown on metal single-crystals. Ideally, the thin film replicates the properties of the corresponding bulk oxide while exchanging charge carriers with the metal substrate. This was achieved in several cases. A 5 Ångström (Å) thin alumina film grown by oxidation of a $\text{NiAl}(110)$ crystal has a bandgap of ≈ 8 eV [5], close to the value measured for bulk alumina. Magnesia films on $\text{Mo}(100)$ can be grown with different thicknesses, reaching bulk characteristics and band gaps at 3 monolayers (ML) [6,7]. Often, a variety of metal single-crystals is taken into consideration as support to optimize the match of the lattice constants. To date, a substantial number of films have been synthesized this way: magnesia ($\text{MgO}(100)$) on $\text{Mo}(100)$ and $\text{Ag}(100)$,

nickel-oxide (NiO(100)) on Ni(100) and Mo(100), alumina (Al_2O_3) on NiAl(110) and Ni_3Al , silica (SiO_2) on Mo(110) and Mo(112), titania (Ti_XO_Y) on Mo(100), Mo(110) and Pt(111), chromia (Cr_2O_3) on Cr(110), vanadium sesquioxide ($\text{V}_2\text{O}_3(0001)$) on Au(111), W(110) and Rh(111), and iron oxide (FeO , Fe_2O_3 , Fe_3O_4) on Pt(111), and others [8–11].

Recently it was discovered that at the ultra-thin limit oxide films exhibit properties in their own right [12]. A monolayer FeO(111) film grown on Pt(111) features substrate-mediated adsorption. From the slight deviation of the lattice constants (3.08 Å to 2.76 Å) a Moiré pattern emerges with a periodicity of 25 Å. Hence, the position of iron atoms varies in respect to the substrate, resulting in an alternation of the surface dipole and in a site-specific adsorption behavior towards Au atoms [13]. The growth of alumina on NiAl(110) is self-limited and leads to a bi-layer (ML) oxide film [5, 14]. While this entity has served well as bulk substitute for the deposition of metal clusters like Rh, Pd, Co and others [15], it turns out that for small Au aggregates the presence of the alloy crystal becomes crucial. One dimensional cluster formations with lengths of up to 22.5 Å and a preferential orientation close to the [001] direction of NiAl(110) were observed. Scanning tunneling spectroscopy (STS) was able to reveal electron transfer from the substrate into the cluster. Chains with 7 Au atoms for instance, being the largest aggregates before crossover to a 2-dimensional growth mode, receive 3 electrons from the substrate [16, 17]. MgO can be fashioned on Ag(001) and Mo(001) with virtually arbitrary film thickness. In case of a 3 ML thin oxide, adsorbed Au atoms are negatively charged and arrange themselves in a hexagonal network to reduce coulomb repulsion. The reduction of the work function by the oxide over-layer in combination with a high electron affinity of the Au atoms issues tunneling of electrons from the substrate to the adsorbate [18]. The work presented in this thesis is following the approach of exploring properties unique to the ultra-thin oxide films in terms of structure as well as adsorption behavior.

However, the constitution of a thin oxide film also affects the geometry and properties of metal particles. In many cases size and shape of the metal deposits are of relevance for their catalytic activity. A number of possible reasons is sketched in Fig. 1.1. Small clusters might be positively or negatively charged. Their electronic structure evolves with size, reflecting the transition from atomic to non-metallic and metallic behavior. Crystal facets differ in adsorption and reactivity. The cluster-oxide interface can play a vital role, as in the case of oxygen storage at the interface of Pd clusters on Fe_3O_4 [20]. Unless a size-selective cluster-deposition method is applied, all techniques that measure across extended sample areas will comprise averaging over the various species. Consequently, a local method which allows the investigation of attributes related to single metal deposits is desired.

To characterize these kind of catalytic model-systems regarding their electronic, vibrionic and optical properties at the atomic scale, a new instrument has been designed and constructed. The new design can be regarded as an extension of scanning

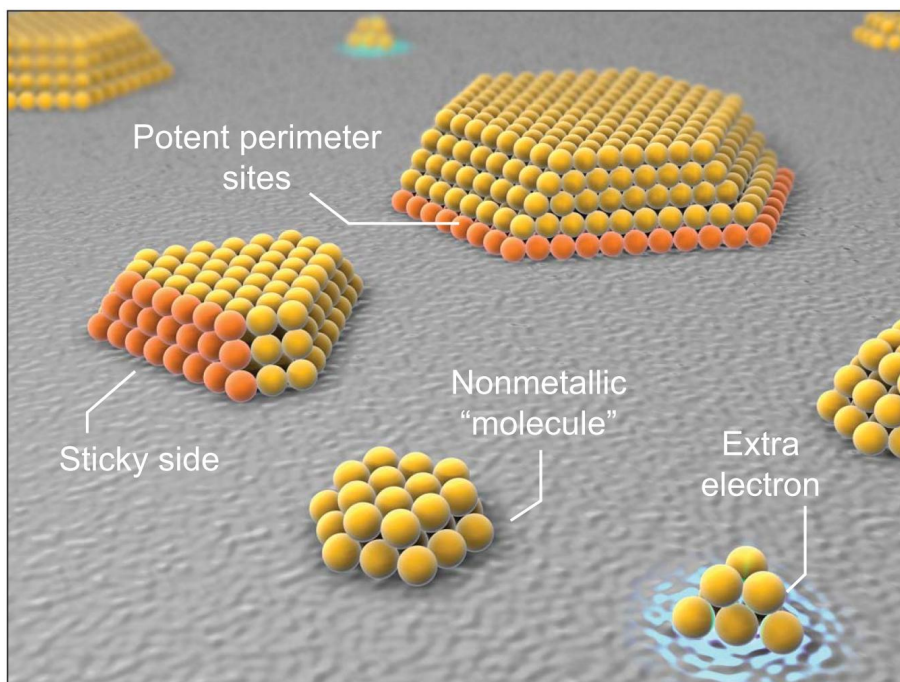


Figure 1.1 Portrayal of a model catalyst depicting potentially size-dependent effects [19].

tunneling microscopy by merging its key characteristic of a superior spatial resolution with several spectroscopic applications. Conductance-spectroscopy and -mapping performed with a scanning tunneling microscope (STM) can reveal the local density of states (LDOS). Inelastic electron tunneling spectroscopy (IETS) provides the vibronic properties of single molecules as a function of their adsorption place. The combination of STM and classical absorption- and emission-spectroscopy enables the local study of optical sample properties as well as photon-induced processes locally. The concept presented in this thesis allows for a comprehensive investigation of fundamental steps of heterogeneous catalysis, such as the adsorption, reaction and desorption of atoms and molecules in well-defined model systems. By merging morphological and electronic measurements, the relation between topography and reactivity of cluster-adsorbate systems can be elucidated, while the influence of inhomogeneity is suppressed by the high spatial resolution. This is a great advantage over other surface science methods like ultraviolet photo-electron spectroscopy (UPS), infrared reflexion absorption spectroscopy (IRAS), electron energy-loss spectroscopy (EELS) or electron-spin resonance (ESR).

The electronic information that is generated by the analysis of a given sample system is directly related to the energy range that is probed. Scanning tunneling spectroscopy focuses on the energy range of a few meV up to a few eV. Both, occupied and unoccupied electronic states are measured by decomposing the current into its

components regarding the energy. The technique can be applied to any conductive or semi-conductive surface, single atoms, molecules, surface states, band edges and field-emission resonances. In the context of this work, the ability to examine the development of the electronic structure of metal adsorbate from single atoms to small clusters alone and in combination with adsorbed molecules as building blocks for model catalysts is of relevance.

The energy range below a few hundred meV contains information about molecular vibrations and surface phonon. Knowledge of the active vibrational mode and its energy can lead to an understanding of the adsorption site, orientation or internal bond reorganization of a molecule. Vibrational modes serve as chemical fingerprints and can be useful for chemical identification or distinction of adsorbed molecular species. Binnig et al. proposed in 1985 to transfer the technique of inelastic electron tunneling spectroscopy (IETS) [21, 22] to the STM [23]. In conventional IETS the effects of vibrational modes of molecules placed at the oxide surfaces inside a metal-insulator-metal tunnel junction and their impact on the tunnel-current are studied. One of the strengths of inelastic electron tunneling spectroscopy is its sensitivity, resulting in the capability to detect vibrations from molecules with a density in the order of $10^{12}/\text{cm}^2$. It has been successfully used in studies of catalysis, biology, trace impurity detection, and electronic excitations.

The first unambiguous observation of an inelastic electron tunneling spectrum by STM was reported by Ho's group in 1998 investigating acetylene (C_2H_2) and deuterated acetylene (C_2D_2) on a copper(100) surface [24]. Since then IETS with the STM has proven its ability to provide vibrational information for a variety of systems: CO on Cu(001) and Cu(110) [25], O_2 on Ag(110) [26], benzene (C_6H_6) and pyridine ($\text{C}_5\text{H}_5\text{N}$) on Cu(001), Cu(II) etioporphyrin-I on Cu(001) [27], FeCO and FeCO₂ [28], and CuCO and Cu(CO₂) on Ag(110) [29] and PdCO [30], AuCO, and AgCO [31] on NiAl(110). Recently, the acquisition of the surface phonon spectrum of Au(111) and Cu(111) plain metal surfaces was achieved [32].

While STS and IETS generate information at the lower energy scale, an unambiguous chemical identification can only be achieved by measuring core level excitations. Auger electron spectroscopy (AES) inspects the occurrence of a certain species but the position remains hidden. Scanning AES requires high energies to obtain the spatial resolution. The pairing of such technique with a low temperature STM seems difficult. Other attempts to introduce chemical sensitivity to the STM include the illumination of the tunnel junction with x-rays [33, 34] and synchrotron radiation [35] while simultaneously recording the resulting changes in the tunneling current. Another promising method was put forward by Reihl et al. [36] and later continued by Palmer et al. [37]. Their concept employs the STM tip in field-emission mode as a local electron source. The electrons are detected in the far field after interaction with the surface. Energy-loss spectra of silicon oxide, graphite and Si(111)7x7 as well as Auger spectra of silicon oxide were presented. This approach was chosen to be included in the design of the new STM.

For certain materials and experimental conditions the tunneling phenomenon is accompanied by the emission of light from the junction [38]. The collection and spectral analysis of this light gives detailed insight into the underlying emission mechanism and provides information about optical parameters that can be compared to the values obtained by non-local optical techniques, such as photo-luminescence, reflectance and absorption spectroscopy [39–41]. Unlike the conventional techniques, these properties can be measured with high spatial resolution, though typically not at the same scale as STM imaging. This way ensemble and background effects can be circumvented, originating from size and shape distributions of optical active entities, their linkage and potentially non-homogeneous dielectric environments. Equipping the new setup with an option for photon collection was therefore an integral part of the design.

The core component of the new experimental setup is an ultra-high-vacuum (UHV) scanning tunneling microscope operating at liquid helium temperatures. A scan-head construction that gives external access to the sample while inside the microscope was implemented as well as the instrumentation needed for the methods described above.

2 Description of the Experimental Methods

2.1 Scanning Tunneling Microscopy

The resolution of conventional optical methods is constrained by Abbe's diffraction-limit to about half of the photon wavelength. The much shorter wavelength of accelerated electrons in scanning electron microscopes (SEM) delivers a higher resolution but not without the setback of the obligatory use of ultra high vacuum, sophisticated lenses and the potential interaction of high energy electrons with the sample.

The idea of imaging surfaces by scanning a local probe was brought forward by Young in 1972 who introduced an instrument he named the *Topographiner* [42, 43]. His device used a metallic needle as field-emitter which was positioned close to a sample surface and moved by piezo-ceramics. about ten years later, scientists at IBM made experiments with a similar design but at conditions where quantum mechanics determines the physics. With potential energies well below the work functions and both electrodes being separated by only nanometers, Binnig, Rohrer, Gerber and Weibel made a historic breakthrough by imaging the Si(111)7x7 reconstruction with atomic resolution which constitutes the birth of scanning tunneling microscopy [44]. It didn't take long to recognize the enormous potential of this new tool for the field of surface science and solid-state physics and in 1986 the Nobel prize was awarded to Gerd Binnig and Heinrich Rohrer.

A scanning tunneling microscope consists mainly of a pointed sensor, usually a metallic tip, and a conductive sample (Fig. 2.1). If the distance between probe and sample becomes appreciably small, the application of a potential difference (U_B) results in a current based on electron tunneling through the vacuum gap. One or both of the electrodes can be moved laterally and vertically relative to each other. The motion is controlled by piezo-electric ceramics at the atomic scale. For instance, by scanning the probe over a sample surface changes in the local topography or electronic structure induce changes in the tunneling current. Thereby a signal is generated which corresponds to the convolution of both effects. The most common way of measurements today is the constant-current mode (CCT), where a feedback-loop controls the probe-sample gap in a way that the tunneling current stays constant during the scanning process. The control signal that regulates the gap-width is then translated into an image.

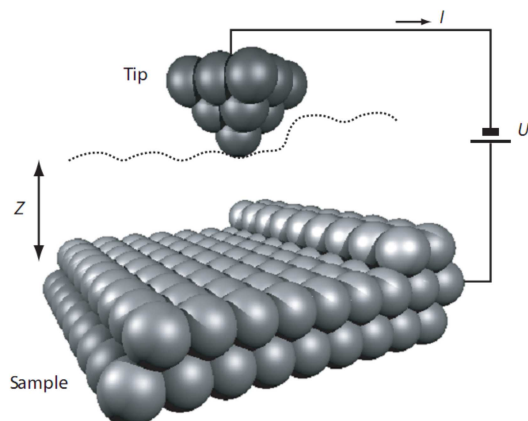


Figure 2.1 Illustration of a tunneling junction, depicting a small atomic cluster as probe, a single crystal surface as sample, the tunneling gap width z , the bias voltage U_B and the current I_T [45].

This amazingly simple device has been successfully applied to many systems. The topography [46] and electronic properties [47] of metal surfaces, semiconductors, single atoms [48] and molecules [49] were investigated. Furthermore, atomic manipulation [50, 51] and spin polarized tunneling [52] were performed. The first low-temperature experiments were done on the superconductor Nb_3Sn [53] and on graphite [54]. The ability of the STM to operate under a wide range of experimental conditions, especially regarding temperatures and pressures, while at the same time being able to provide local information of the surface has made it a capable tool for the investigation of model catalysts [15, 55, 56].

Calculation of the Tunneling Current

The tunneling current consists of the contributions of elastic and inelastic electron transport, though the inelastic tunneling channels make up for only a few percent of the total signal. Due to their difference in nature they will be described separately. In this section only elastic tunneling is taken into consideration while inelastic tunneling is discussed in Sec. 2.2.2.

The theoretical treatment of tunneling currents started long before the discovery of STM. Bardeen calculated the transition probability for electrons tunneling through Metal-Insulator-Metal structures as early as 1961 [57]. Instead of solving the Schrödinger equation for the combined system of two electrodes and a gap, he considered two sub-systems with independent electronic states which are obtained by solving the stationary Schrödinger equation for each side individually. The transmission rate across the tunneling junction is then calculated by using time-dependent perturbation theory. One of the main contributions of Bardeen's approach is the de-

scription of the tunneling matrix element M as being determined by a surface integral of the unperturbed wave-functions at the separating surface:

$$M_{\mu\nu} = -\frac{\hbar^2}{2m} \int_S (\chi_\nu^* \nabla \Psi_\mu - \Psi_\mu \nabla \chi_\nu^*) \vec{n} df, \quad (2.1)$$

where m refers to the mass of the electron, df to the surface area located between probe and sample and \vec{n} to a vector normal to this surface. Ψ_μ and χ_ν represent the wavefunctions of the states μ of the probe and ν of the sample, respectively. The matrix element has the dimension of energy and represents the interaction energy resulting from the overlap of the undisturbed states of each side. It needs to be mentioned that neither Ψ_μ nor χ_ν are eigenfunctions of the Hamiltonian for the combined system and that the two sets of wave-function are only approximately orthogonal:

$$\int \Psi_\mu^* \chi_\nu d^3\vec{r} \cong 0. \quad (2.2)$$

Bardeen's approach is based on several assumptions. He considered the tunneling barrier to be of finite width and both electrodes to be metallic with independent density of states. Furthermore, the quasi-particles would not correspond to plane waves but to states that either reflect at the barrier or decay exponentially with distance into the vacuum barrier. In analogy to Fermi's golden rule the transition probability for a wave-function Ψ_μ on one side of the barrier to wave-function χ_ν on the opposite side as induced by a perturbation of the potential can be written as:

$$w_{\mu\nu} = \frac{2\pi}{\hbar} |M_{\mu\nu}|^2 \delta(E_\mu - E_\nu), \quad (2.3)$$

with the condition for elastic tunneling $E_\mu = E_\nu$. E_μ and E_ν represent the eigenenergies of the states μ and ν , respectively.

Shortly after the invention of STM, Tersoff and Haman (TH) provided an alternative formulation of the tunneling current that is well established and in use until today [58, 59]. The simulated images shown in this work, calculated by Pacchioni's group (Chapter 5.3 and 5.4), are based on their mathematical model. The different nature of the STM junction compared to Bardeen's theory for planar tunneling required the deconvolution of the sample- and usually unknown probe-states to be able to treat the latter separately. Within the TH model the probe is described as a geometrical point, ergo, an STM image is related to the properties of the unperturbed surface alone, rather than the combined probe-sample system¹ [60]. For the electronic structure of the probe, a single s -orbital is assumed.

The total current flow at the bias voltage U_B can be calculated from the transmission coefficient $|M_{\mu\nu}|^2$ as

¹These assumptions lead to meaningful interpretation of STM images for feature sizes ≥ 1 nm.

$$I_T = \frac{4\pi e}{\hbar} \int_{-\infty}^{\infty} [f(E_F - eU_B + \epsilon) - f(E_F + \epsilon)] \times \rho_P(E_F - eU_B + \epsilon) \rho_S(E_F + \epsilon) |M|^2 d\epsilon, \quad (2.4)$$

where $f(E)$ is the Fermi distribution function. This equation can be understood as convolution of the local density of states of the probe $\rho_P(E)$ and the sample $\rho_S(E)$. The integration accounts for the forward-flow of the electrons as well as the back-flow, since for finite temperatures the occupation probability at an energy $E_F + eU_B$ is non-zero .

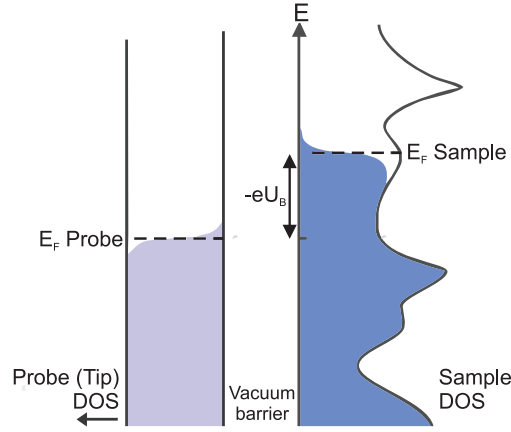


Figure 2.2 Schematic of the density of states (DOS) of probe and sample for a biased tunneling junction. It is the convention that the polarity of the voltage refers to the sample side, hence, a negative bias leads to tunneling from the sample into the probe.

Fig. 2.2 sketches the sample–probe junction and the LDOS of both electrodes. If the sample is biased by a negative voltage U_B with respect to the tip, the Fermi level of the sample is offset with respect to the probe. Electrons will mainly travel out of the filled states of the sample, into the empty states of the probe.

The TH model can be extended to finite bias voltages. With the following preconditions: (i) the relevant probe state is of spherical symmetry (s-like); (ii) the tunneling matrix element is independent of the energy level; (iii) the probe DOS is flat across the included energy range and (iv) the sample DOS varies only little in units of kT , then equation 2.4 for the tunneling current becomes [60]:

$$I_T = \frac{4\pi e}{\hbar} \int_0^{eU_B} \rho_P(E_F - eU_B + \epsilon) \rho_S(E_F + \epsilon) |M|^2 d\epsilon$$

$$\approx \frac{4\pi e}{\hbar} \rho_P |M|^2 \int_0^{eU_B} \rho_S(E_F + \epsilon) d\epsilon. \quad (2.5)$$

It is appropriate to choose a material for the tip with a flat distribution of the density of states. This assumption is valid for the widespread probes made of tungsten and platinum-iridium as long as only *s*- and *p*-like states are taken into account². In this case the density of states can be treated as a constant and written outside the integral. If the overlap of the wavefunctions is small the matrix element for tunneling will be virtually independent of the potential difference between the electrodes. One of the consequences of the approximations within the TH model is the representation of the tunneling matrix element by a simple exponential term (WKB approximation) $|M|^2 \propto |\Psi(r_0)|^2 \simeq e^{-2\gamma}$, with γ given by:

$$\gamma = \int_0^d \sqrt{\frac{2m\phi}{\hbar^2}} dz = \frac{d}{\hbar} \sqrt{2m\phi}. \quad (2.6)$$

The term d refers to the distance between the electrodes, ϕ is the median barrier height which is given by the average of both work functions. In conclusion, the current is well approximated by:

$$I_T \approx \frac{4\pi e}{\hbar} \exp\left\{-\frac{2d}{\hbar} \sqrt{2m\phi}\right\} \rho_P \int_0^{eU_B} \rho_S(\epsilon - eU_B) d\epsilon. \quad (2.7)$$

The TH model is not able to account for the richness of observations with the STM. In those cases the Bardeen formulation of M needs to be evaluated. Nevertheless, despite its simplicity, it can deliver excellent results as shown later in this work.

2.2 Scanning Tunneling Spectroscopy

An image in STM can be regarded as a convolution of atomic positions and the underlying electronic structure. In various experiments it is of particular interest to get access to the electronic or chemical properties of the surface, including the local density of states, the work function, collective electron excitations and vibrations. All this information is hidden within the current. Hence, a decomposition of the current into its components permits the extraction of the relevant information. The total current consists of contributions from elastic and inelastic tunneling channels. The interdependence of various tunnel parameters leads to a number of derivations which bring out the relevant properties. Most common are dI/dV , dI/dz and dz/dV measurements for elastic tunneling and d^2I/dV^2 for inelastic tunneling.

²A more realistic LDOS description that includes d-states was introduced by Chen and is partially seen as the reason for the high resolution achievable with the STM.

2.2.1 Spectroscopy Based on Elastic Tunneling

dI/dV Spectroscopy

It is intuitively clear that the magnitude of the conductance correlates to the presence of electronic states on the sample surface. In accordance to Eq. 2.5 the tunneling current is derived by integrating over all sample states up to the energy eU_B . Selloni was the first to propose the derivative of the current with respect to the voltage as a measure for the samples density of states [61]:

$$\frac{dI}{dV} \propto \rho_S(eU_B)T(d, \epsilon, eU_B). \quad (2.8)$$

This is a simplified expression for the derivative of Eq. 2.7. The assumption made earlier for several terms to be changing slowly with energy and hence to take them outside of the integral is not indicated for a proper description of dI/dV spectroscopy, especially since experiments often cover an energy range of several eV. Therefore, the transmission probability

$$T(d, \epsilon, eU_B) \propto \exp\left(-d\sqrt{\frac{\phi + eU_B}{2} - E_F}\right) \quad (2.9)$$

is energy dependent. The term ϕ denotes the average work function of probe and sample. Taking the derivative, one derives the proportionality in a more complete form where the dependence of the tunneling probability with respect to the bias voltage is accounted for:

$$\frac{dI}{dV} \propto e\rho_S(eU_B)T(eU_B, eU_B) + e \int_0^{eU_B} \rho_S(\epsilon) \frac{dT(\epsilon, eU_B)}{d(eU_B)} d\epsilon + e \int_0^{eU_B} T(\epsilon, eU_B) \frac{d\rho_S(eU_B)}{d(eU_B)} d\epsilon. \quad (2.10)$$

Based on Eq. 2.8 the DOS is evaluated at the energy $\epsilon = E_F + eU_B$. Although this expression is rather general in nature, it pinpoints the extraordinary potential of this method to investigate the local density of states with the resolution of STM. Due to the evolution of $T(d, \epsilon, eU_B)$ the dI/dV signal diverges exponentially with increasing bias voltage, which adds difficulties to a proper discrimination of DOS features from the background. To account for this phenomenon within the data analysis Fennstra et al. suggested the evaluation of the normalized signal $(dI/dV)/(I/V)$ instead [62]. Lang calculated the peak position for a Lorentzian-like feature in the sample DOS with respect to its full-width half-maximum (FWHM) [63]. The results differed between the standard and the normalized expression. Using the dI/dV term tends to overestimate the peak position with increasing FWHM. On the other hand the $(dI/dV)/(I/V)$ term underestimates the true value for small FWHM. Altogether, the results merge around a FWHM of ≈ 1.5 eV. For features that are less extended dI/dV is the better

choice, for broader features $(dI/dV)/(I/V)$ is more exact. Throughout this work, the expression dI/dV was used as indicated by the acquired data.

It is noteworthy that dI/dV spectroscopy has the unique capability to probe both occupied and unoccupied states within the same experiment, by simply changing the bias polarity. Other commonly employed, non-local methods (PES, MIES, IPES, NEXAFS) have to be applied complementary and require a greatly increased experimental effort. In addition, STS literally measures the LDOS while non-local methods by nature average over comparably huge areas. On the other hand STS is limited to an energy range below the work functions of both electrodes, which often requires a combination of local and non-local experiments. We note that only states with high spatial extension into the vacuum, hence with a good overlap with the tip wave functions are actually detected in STS. Spatially highly confined levels, e.g. d - and f -states are therefore hardly observed.

dI/dz Spectroscopy

In section 2.2.1 it was shown that the current can be dissected to obtain the density of electronic states at a certain fixed the bias voltage. Another quantity of interest is the dependence of the current on the width z of the vacuum barrier. From equation 2.7 we obtain:

$$\phi = \left(\frac{1}{1.025} \frac{d \ln(G_t)}{dz} \right), \quad (2.11)$$

where $G_t = (I/V)$ represents the tunneling conductance and ϕ the average barrier height [64]. This quantity stays constant over a large range of z which stresses the fact of the purely exponential dependence of the current on the tip sample separation. Even though the average barrier height and the work function of the sample are not the same, there is a distinct connection. Yhoshikawa et al. have studied the influence of Cs adsorbed on Si(111)7x7 and found a reduction in the local barrier height at Cs sites of $\Delta\phi = 0.87$ eV in correspondence with the low work-function of Cs [65]. Rienks et al. have investigated a polar iron oxide film and extracted the dipole strength by correlating it with measurements of the average barrier height [66]. They found variation of the surface potential within the unit cell of the Moire pattern that the oxide forms with its Pt(1 1 1) support. Areas with a stronger surface dipole effectively increased ϕ and hence the work function.

In practice, this type of spectroscopy is performed in analogy to dI/dV measurements by modulating the z -position of the scanner by values of up to several Å. Typically, a lock-in technique is applied, modulating the z or V input parameter while performing a phase sensitive measurement of the current. The frequencies used range from 0.5 to 100 kHz [67], ideally lower than the cutoff of the preamplifier but far way from any resonance of the scan-head.

dz/dV Spectroscopy

When the feedback-loop is enabled and is actively regulating the tunneling-gap width, a given bias voltage in combination with the set-point value of the current directly translate into a defined electrode distance which is related to the local conductance and the transmission barrier. This fundamental relation of STM can be used for yet another spectroscopic mode which is referred to as dz/dV spectroscopy. For the constant-current mode one can write:

$$\frac{dI}{dV} = \left(\frac{\partial I}{\partial z} \right)_V \frac{dz}{dV} + \left(\frac{\partial I}{\partial V} \right)_z = 0, \quad (2.12)$$

and since $(\partial I/\partial z)_V$ is a slowly varying function, $(\partial I/\partial V)_z \simeq -dz/dV$. Hence, $(\partial I/\partial V)_z$ will be mirrored by (dz/dV) . A step of $z(V)$, for instance due to the opening of a new conductance channel, will be transformed into a peak of the $|(dz/dV)|$ and $(\partial I/\partial V)_z$ -signal alike [68].

Because the feedback-loop stays active, large energy ranges can be covered within a single measurement. Once the applied bias exceeds the average work function of the electrodes, electronic states above the vacuum level become accessible. Gundlach was the first to calculate the transmission coefficient and the tunneling current for this scenario [69]. For metal/insulator/metal systems, he found that the conductance is superimposed by oscillations. In the case of STM tunnel-junctions, these oscillations can be understood as field-emission resonances that form as result of the large electron mean free path at energies above the vacuum level and their reflexion at the sample surface and the tunnel barrier. The condition for standing wave formation depends on the shape of the electronic potential inside the classically permitted part of the tip-sample gap, which is mainly governed by the presence of the tip, the tip-induced electric field that determines the slope, the energy of the electrons, and the reflectance of the sample surface.

Coombs and Gimzewski have presented an approximation for the resonance condition inside the gap [70]. According to their description, the resonance condition is fulfilled if the length of the electron path between the sample surface and the reflexion point at the vacuum level (or between the tip surface and the vacuum level crossing point of opposite polarity, respectively) is equal to half the electron wavelength times an integer number. Then the wave vector $k(z)$ of the propagating electron is given by:

$$k(z) = \frac{2\pi\sqrt{2me}}{\hbar} \sqrt{\frac{eU_B}{z_0}z - \Phi}, \quad (2.13)$$

with z_0 being the separation of the electrodes and Φ the average work function. For the n^{th} order of the resonance the integration between the turning point $z = z_T$ and the sample surface has to result in a total phase change of πn :

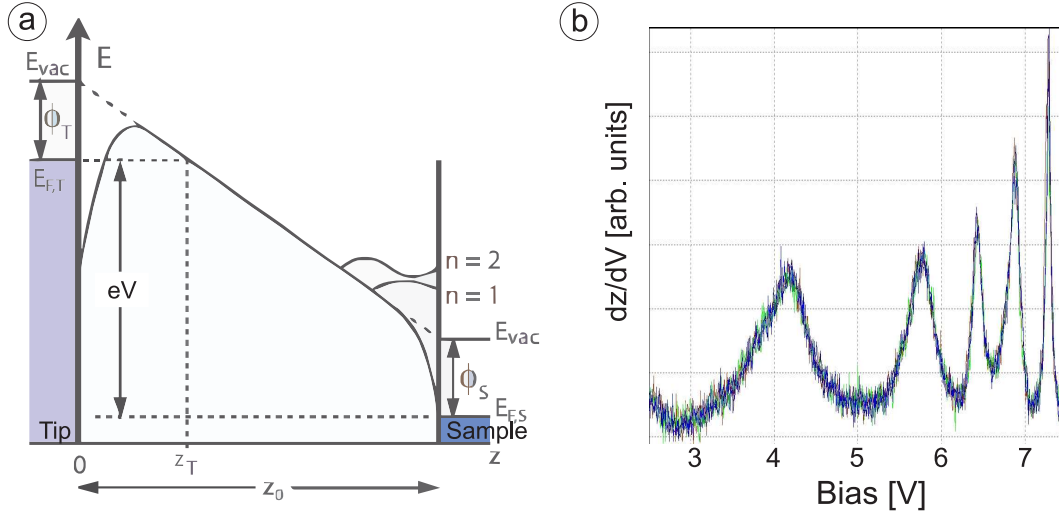


Figure 2.3 Field emission resonances within a tunneling junction: (a) Potential diagram of the gap indicating the states $n=1$ and $n=2$ above the vacuum level. (b) Measurements of field-emission resonances that form between a PtIr tip and a $\text{SiO}_2\text{-Mo}(1\ 1\ 2)$ surface (see Cha. 5).

$$\pi n = 2\pi \frac{\sqrt{2me}}{\hbar} \frac{2z_0}{3eU_B} (eU_B - \Phi)^{\frac{3}{2}}, \quad (2.14)$$

or, expressed in terms of the bias voltage U_n , corresponding to the n^{th} state:

$$U_n = \Phi + \alpha n^{\frac{2}{3}} E^{\frac{2}{3}}. \quad (2.15)$$

The field strength E is entered in units of $\text{V}/\text{\AA}$ and α is simply a constant ($\alpha = 4.39V^{\frac{1}{3}}A^{\frac{2}{3}}$). Image forces are neglected in this approximation, though they distort the potential right in front of the electrodes and affect the oscillations for small n (see Fig. 2.3). It should be noticed that the dependence of the resonances on the work-function can be used to extract the latter quantity from dz/dV spectra.

2.2.2 Inelastic Electron Tunneling Spectroscopy

Electron tunneling from an initial occupied state in one electrode to a final unoccupied state in the other electrode without energy loss during the transmission is considered elastically and represents the largest contribution to the current. Energy loss during the transition changes the total current only slightly but is, due to the very nature of its origin, of highest interest. An adsorbate, e.g. a molecule, present between the electrodes perturbs the local density of states in a unique way, producing a different I-V

dependency than the sample itself³. If the energy of the tunneling electrons is sufficient to excite a molecular vibration, the electron is scattered and leaves the molecule in an excited state. The inelastic scattering provides an additional channel for electron tunneling and increases the differential conductance $\sigma = dI/dV$. At the threshold for the excitation $\hbar\omega = eU_B$ the current shows a small onset, being seen as a step in the derivative or as a peak in the second derivative (Fig. 2.4).

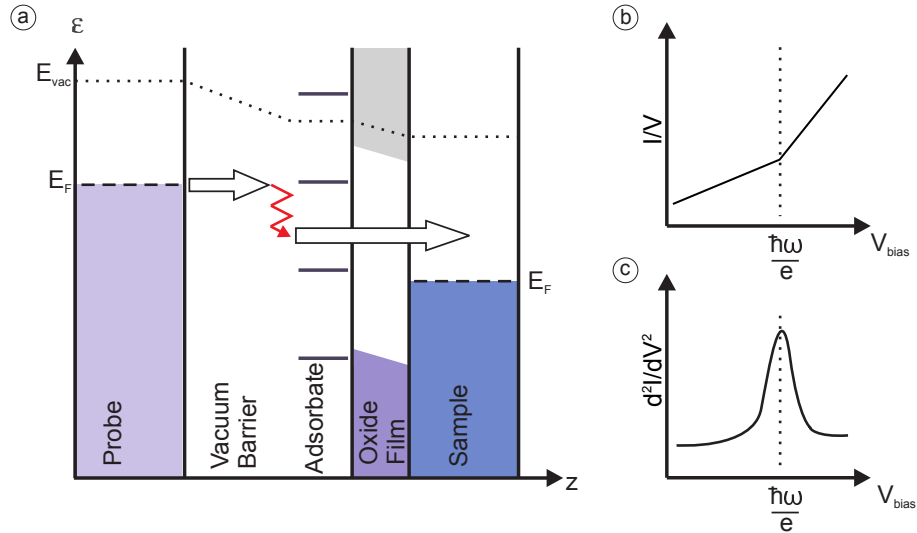


Figure 2.4 Inelastic electron tunneling spectroscopy: (a) Schematic of inelastic electron energy transfer within the tunneling gap due to the excitation of a vibration. (b) The resulting current increases due to the opening of another tunneling channel at the excitation energy $\hbar\omega/e$ and (c) how this onset translates into a peak of the second derivative of the current.

Early calculations by Garcia et al. [23] and Persson et al. [71] based on the dipole scattering approximation of Scalapino and Marcus [72] predicted changes of the conductance of a few percent at most. In this case the interaction between an electron and a molecule is described by a dipole potential:

$$U_{int}(z) = \frac{2ep_z z}{\epsilon(z^2 + R^2)^{\frac{3}{2}}}.$$

The equation contains the electron charge e , the dipole strength and the distance perpendicular to the surface p_z and z , respectively, and the radial distance from the dipole R . Since the molecule is in a polarizable medium the dielectric constant ϵ appears. It has been suggested, however, that the dipole scattering approximation may not be precise at the Ångström-scale of STM tunneling gaps, and that resonance

³This is the elastic contribution.

as well as impact scattering may lead to an enhancement of $\Delta\sigma/\sigma$ to values around 10% [73, 74]. These small changes of the conductance can be directly translated into requirements for the stability of the tunnel junction: to keep the current stable within 2% fluctuations of the gap-width have to be reduced to below 0.01 Å. This requirement is usually fulfilled only in LT-STMs.

The energy resolution expressed in terms of the full-width at half-maximum (FWHM) of the d^2I/dV^2 vibrational peak is given by

$$V = ((1.7U_{mod})^2 + (5.4kT/e)^2 + W^2)^{\frac{1}{2}},$$

where U_{mod} is the bias modulation voltage for the lock in detection, k is the Boltzmann constant, T the temperature, and W the intrinsic width as given by the lifetime of the vibrational excitation.

Photon Emission Scanning Tunneling Microscopy and Spectroscopy

Light emission spectroscopy can be conducted with an STM to measure optical properties of a conductive sample surface locally with resolutions in the sub-nanometer range [75]. An optical response is evoked by the spatially confined electrons that travel within the junction. The energy of these electrons can be tuned by simply adjusting the bias voltage.

The identification of the underlying mechanisms is related to the nature of the cavity where the relevant processes are triggered [76]. Excitations within the junction refer to inelastic electron tunneling between probe and sample accompanied by an energy transfer to optically active modes. Excitations within the sample itself refer to the injection of a spatially confined electron (hole) beam from the STM probe, followed by electro-luminescence. In either case it is the radiative decay of the respective excitations that lead to photon emission.

In principle, the detection of light from an STM junction should be rather difficult due to the low emission cross section of the local excitation. Even for conventional, non-local methods the photon yield tends to be close to the detection limit [77]. The distinguishing phenomenon is the tip-related enhancement of the electro-optical modes within the cavity [78, 79]. The enhancement results from the stimulation of collective oscillations in the electron gas of probe and sample. These oscillations are coherent in phase and delocalized over both electrodes. The name *tip-induced plasmons* was given with reference to the term *plasmons* for collective electronic excitations in bulk materials, surfaces and clusters.

The theoretical description considers the frequency-dependent enhancement factor G to be the ratio between the induced electromagnetic field within the junction at position r_j and a tip-independent, incorporated virtual far-field source at the position r_f :

$$G(\Theta, r_j, \omega) = \frac{E_{ind}(r_j, \omega)}{E_{inc}(\Theta, r_f, \omega)}. \quad (2.16)$$

To quantify this equation, G is split in two terms. The first one is G_0 , which describes the enhancement in absence of the tip due to the interference of the incoming and reflected waves with Frenel's formula. The other one, G_{ind} , is accounting for the presence of a tip. The respective scalar potentials $G(\Theta, r_j, \omega) = -\frac{\delta}{\delta z}\Phi_0 - \frac{\delta}{\delta z}\Phi_{ind}$ can be calculated by solving the Laplace equation numerically and inserting the correct boundary conditions for the simplified junction geometry.

The radiative decay of TIP modes within the tunneling junction occurs from a sequence of mechanisms. The presence of a tip in close proximity to a surface induces a general field enhancement within the STM cavity. The strength of the enhancement is a function of the dielectric properties and the geometry of the surrounding electrodes. Tunneling electrons transfer energy inelastically to TIP-modes with the excitation cross section depending on the gap width and the presence of suited initial and final electronic states in probe and sample. This excitation is followed by the decay of TIP-modes through radiative and non-radiative channels. High emission yields are expected for electrode materials whose dielectric function have small absorption indices, which results in longer TIP lifetimes and accordingly higher probabilities for radiative decay.

The inelastic tunneling current can be related to the electromagnetic gap modes and the associated radiation field $E(r, \omega)$ according to the reciprocity-theorem of electrodynamics [Johansson-1992]:

$$E(r, \omega) = \int d^3r_j \frac{\omega}{c^2} \frac{e^{ikr}}{r} G(\Theta, r_j, \omega) \cdot j(r_j, \omega). \quad (2.17)$$

The term $j(r_j, \omega)$ constitutes the current density of electrons tunneling inelastically along the probe-sample axis, which is evoked by electron transition from an initial tip-state $|i\rangle$ to a final probe-state $|f\rangle$. Finally, the differential power of the light emission can be calculated by summing over all possible transitions that obey the requirement of energy conversation:

$$\frac{d^2P}{d\Omega d(\hbar\omega)} = \frac{c}{2\pi} \sum_{i,f} r^2 |E(r_j, \omega)|^2 \delta(\epsilon_i - \epsilon_f - \hbar\omega). \quad (2.18)$$

Several systems have been successfully investigated with this method, including light emission from metal surfaces [78, 80, 81], metal nano-particles [82, 83], semiconductors [84–86] and molecules adsorbed on thin, metal-supported oxide films [87, 88].

Remarks

The most comprehensive set of data regarding the electronic, vibrational and optical properties of a surface can be achieved by measuring a full spectrum at each point of a

2-dimensional matrix⁴. The result is a multi-dimensional data array, with its dimension depending on the number of simultaneously recorded channels. However, this kind of data acquisition is time consuming, requires an extraordinarily high stability of the probe-sample geometry and potentially produces repetitive results. Even though this is justified in some cases, often a smaller amount of data-sets will already describe the surface properties satisfactorily.

The decomposition of the current can be done mathematically but this method is in most cases compromised by noise and can not deliver useful results. The best signal-to-noise ratio (SNR) is achieved by phase-sensitive measurements using a lock-in amplifier (LIA). Commonly, a small AC component is added to the bias voltage and the responding tunneling current is fed back into the LIA where it is dissected. The first harmonic of the signal is directly related to LDOS at the DC value of the bias, while the second harmonic provides a measure of the inelastic current.

For point spectroscopy the width of the tunneling gap is fixed and the bias voltage is slowly ramped across the energy interval of interest. Alternatively, conductance maps are acquired by reading the lock-in signal while taking images in constant-current mode. This allows for easy generation of a spacial profile of specific electronic states. Similar measurements can be performed with the optical channel, producing photon-maps of the surface.

⁴Hyperspectral imaging.

3 Construction of a Low Temperature Scanning Tunneling Microscope

3.1 Design Criteria

The new design was made to be most suitable for investigations of model systems for heterogeneous catalysis at a fundamental level. Following the bottom-up approach, characterization usually starts with the morphology of the substrate that serves as template. This is followed by an examination of the thin oxide films grown on that substrate. Finally, metal deposits and molecular adsorbates are studied.

Two main requirements have driven the development of the here presented setup. One is the need to study complex systems, the other is the goal to apply several spectroscopic techniques to the same surface region of a stationary sample. All applications must be made possible for a sample residing inside the microscope and should include:

- metal evaporators to deposit single atoms or small metal aggregates in situ;
- gas inlets for exposure to CO, NO, or noble gases like xenon;
- a hemispherical mirror analyzer (HMA) including an electronic lens for electron collection in the far field;
- an array of lenses for photon collection from the tunnel junction;
- a laser to carry out photo-excitation experiments;
- optional a X-ray source or an electron gun.

As a result, two contrary demands had to be met. Only at low temperatures the required thermal stability and appropriate suppression of adsorbate diffusion is achievable. Consequently, the cooling of the sample or even the entire microscope to temperatures below 20 K was indicated. At the same time spectroscopic methods require access to the cooled sample, while the instruments themselves remain at room temperatures. Since tunneling and vibrational spectra are acquired subsequently at specific

surface sites, only very small thermal drifts in the range of a few picometer per minute would be acceptable.

The microscope itself had to be designed in a way that access to the sample would be feasible from positions distributed over an angle of at least 200 degrees. Only then all applications would cover the required surface area. In addition, a probe exchange mechanism had to be implemented to allow tip replacement without breaking vacuum, resulting in much shorter turnover times. This is of particular importance in photon-emission experiments since photon emission from the tunneling junction is known to be sensitive to shape and material used as tip which makes frequent replacements even more likely.

Mechanical and acoustical noise transmitted into the experiment from the surrounding environment had to be suppressed significantly to assure accurate performance of the microscope. The laboratory location for this setup exhibits severe noise from different sources: a large number of rotary-pumps and turbo-pumps belonging to several other experimental setups nearby, a subway in close proximity and common activities like doors closing or mechanical work being done within the building. Therefore a vibration isolation had to be included.

The preparation of thin oxide films on single crystal surfaces requires the admission of gases into the UHV system, reducing the quality of the vacuum. The sputtering with argon is commonly done with Ar^+ pressures in the range of 10^{-6} to 10^{-5} mbar. Sample heating can increase the background pressure up to several 10^{-8} mbar. For the oxidation of the sample surface, O_2 pressures of typically 1×10^{-6} are used. To protect the microscope and the cryostat from these contaminations, two separate chambers, one for the experiment and one for the preparations, have been favored.

In the following section the design choices based on these requirements are described.

3.2 The Setup

3.2.1 The Microscope

Scan Head

Principle The different requirements for the scan-head could be met by choosing the Besocke type, a design commonly known as *Beetle* [89] which is shown in Fig. 3.1. This design has demonstrated its potential in various room-, low- and high- temperature applications, including measurements on metal deposits, oxide surfaces [90], high-temperature superconductors [91], and the employment of atomic manipulation [92] and vibrational spectroscopy [93]. An intrinsic compensation of temperature-induced thermal drift makes it most suitable for variable temperature measurements. Combinations with additional methods like molecular beam epitaxy (MBE) [94] and scanning electron microscopy (SEM) [95] have been successfully realized.

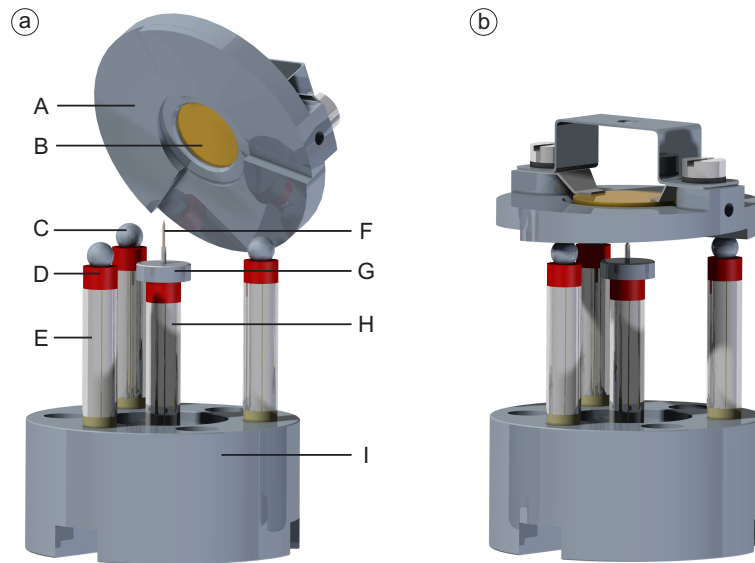


Figure 3.1 Model of the scan-head depicting the tripple-helix sampleholder with an inclination of $1\text{ mm}/120^\circ$ (A), a sample (B), three steel balls to support and contact the sample holder (C), sapphire isolators (D), three piezo-legs for support and offsets (E), the tip (F), the tip-holder (G), the scan-piezo (H) and the base plate (I).

The *Beetle*-type concept uses four piezo-ceramic tubes which are placed on a rigid base. Three ceramics are positioned with equal spacing at the corners of a triangle, while the fourth tube is placed in the center. Outside and inside each piezo-element is coated with nickel to apply the controlling voltage¹. The outside electrode is divided in 4 radial segments covering close to 90 degrees each. To prevent electrical shortening or discharge, 1 mm of the conductive coating is removed at the mounting side where the tube connects to the base. The piezo-element in the center serves as scanner. By applying voltages to the individual sectors the probe can be moved laterally across the sample. If the same voltage is applied to all four electrodes synchronous, the scanner contracts or expands, respectively. The sample rests on the three outer piezo-elements, which serve as offset elements. For a coarse approach between the sample and the probe, the sample-holder integrates a triple-helix at the bottom as shown in Fig. 3.1a². A saw-tooth like control voltage induces a radial slip-stick motion of the piezo-legs. The subsequent change of the resting position on the triple-helix decreases the tip-sample spacing. Once the distance reaches a value suitable for tunneling, the motion stops and the distance is fine-controlled by the scanner. In a similar way the lateral offset of the sample is accomplished by moving the legs in parallel. The application of a DC voltage instead of a saw-tooth allows for a fine control of the

¹Charge amplifier are superior to voltage amplifier but are rarely used.

²The sample holder is lifted for better visualization.

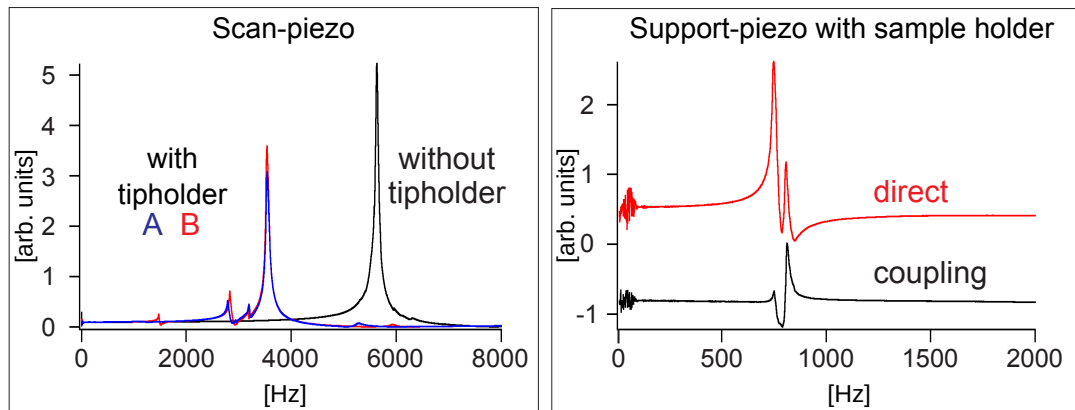


Figure 3.2 Eigenfrequencies of the scan-head. Left: resonances of the tube-scanner with and without tip holder. Right: resonances of an outer piezo-leg while supporting the weight of the sample holder. For the upper curve excitation as well as response are measured at the same piezo-element while for the lower curve two different elements are used.

lateral position.

The benefits of the Besocke-design are obvious. The sample is accessible along an azimuthal angle of about 300° and polar angles between -8° and -45° . The rigid construction of the scan-head leads to eigenfrequencies well above the ground vibrations and the dominating acoustic frequencies. Temperature changes affect all ceramics in a similar way which results in excellent compensation of thermal drifts. The consequent reduction of constructive elements and material leads to very simple device that guarantees reliability.

Assembly The ceramics (EBL No. 2, dim.: 3.2 mm OD, 12.7 mm length, 0.5 mm wall thickness, EBL Products Inc.) are glued to the base plate (Epotek H77, Polytec PT) and capton coated electrical wires (KAP012, Caburn MDC) are soldered (Soldamoll 220, BrazeTec) to the nickel plates. The upper tube ends are electrically isolated by sapphires (Giese KG). The outer piezos are terminated by steel balls (2.5mm \varnothing) which serve as electrical contacts to the sample-holder. The sapphire at the end of the scan piezo carries a small magnet (DE 153, SmCo, IBS Magnet) inside and the entire top side is chromium and gold plated to connect the tip carrier. Steel balls and magnet are connected by coaxial wire (KAP3, Caburn MDC) which is fed through the ceramics. The shielding of the coax-wire also connects the inner electrodes of the piezos.

Operation The operation of a scan-head is to a large extent determined by the properties of the piezo-elements [96]. The tube dimensions in combination with a particular piezoelectric material lead to resonances which impose a limit for the scan

speed as well as for level and spectral density of the acoustic noise that the tunneling junction can transmit. In addition, the mass of parts stiffly connected to the ceramics lead to a down shift of the eigenfrequencies. Fig. 3.2 depicts the resonances of scan- and support-piezos. For each of these measurements, one of the four radial electrodes was excited by an AC voltage of 5.6 mV peak-to-peak and the response was detected on the electrode vis-a-vis.

The scan piezo without tip holder carries the smallest load with only the sapphire extension and the magnet attached to it. As result it exhibits a characteristic frequency of 5500 Hz. The additional weight of the tip holder (0.25 g) shifts the main resonance to 3450 Hz but also adds smaller resonance peaks at 3100 and 2900 Hz. These side features indicate slight rattling which may be resulting from the limited stiffness of the connection between the magnetically held tip-holder and the scan-piezo. A different tip holder exhibited a small feature around 1400 Hz that is not present at the former one. This feature has been taken as indicator for a less planar and therefore unstable contact between both parts and could be removed by remounting the tip-holder. Hence, the quality of the assembly can be monitored externally after each tip exchange. The support-piezos carry a substantially larger load, sharing the mass of sample-holder and sample (11.4 gr). Consequently the resonance peak is located at ≈ 720 Hz. The same test performed by excitation of one support piezo and detecting the signal at another one demonstrates the strong coupling between the outer ceramics (Fig. 3.2, left). Since the lateral scan is done with the center-piezo, the resonance at 720 Hz does not play a significant role during image acquisition. However, since it is the lowest eigenfrequency, it determines the coupling of mechanical noise into the tunneling junction. The higher such resonance is located in the frequency domain, the smaller the impact of vibrations during tunneling.

A crucial parameter for the operation of the scan head is the dynamic range of the scan-piezo, which is determined by the response of the material (EBL #2), the highest field applicable without depolarization, and the dynamic range of the amplifier. The change in length as response to the applied voltage is given by:

$$\Delta L = \frac{2d_{31}VL}{(OD - ID)} \quad (3.1)$$

where d_{31} refers to the piezoelectric charge constant, V to the applied voltage, L to the length of the scanner and $(OD - ID)$ to the wall thickness. For the ceramic type EBL #2, Eq. 3.1 results in a sensitivity of 8.79 nm/V at room-temperature, which is close to the value obtained by calibration using the height of a single step in the NiAl(110) surface. At 10 K the sensitivity is severely reduced to 1 nm/V. To avoid depolarization the voltage needs to stay well below 0.7 kV/mm or, taking the wall thickness of 0.5 mm into account, below 350 V. The high-voltage amplifier deliver +/-215 V with a peak to peak noise of 2 mV. Hence, the dynamic range of the scanner at 10 K is $\simeq 2 \times 10^5$ and covers 0.002 to 430 nm.

Microscope Base and Suspension

The performance of a microscope can be improved by reducing the coupling to external vibrations. Two types of isolating systems are prevalent for STM applications [97]. One type consists of a microscope suspension by either a single stage or by multiple stages of coil springs paired with an eddy-current damping unit. The transfer function equals a low pass with resonance peak. The decay beyond the resonance increases with the number of spring stages but so does the amplification at the resonance. The necessary damping counteracts the peaking but also reduces the order of the low pass. The second type utilizes multiple stacks of Viton[®] elastomers separated by metal plates. This approach is particular efficient for frequencies above 30 Hz. At low temperatures the elastic properties of elastomers decrease severely and the functionality is lost. Springs, on the other hand, contract and thus change the position of the microscope. Nevertheless, due to the good performance, this is a tolerable drawback and thus a spring suspension was chosen for this design.

The scan-head is mounted to the base plate of the microscope, consisting of a stainless-steel disk with a diameter of 68 mm and a height of 14 mm. This unit is sustained by three springs (stainless steel, k : 0.03 N/mm, Federntechnik Knörzer). Copper pieces connect them at their upper end to the cryostat and this connection also includes the level adjustment. The eigenfrequency of the system is given by:

$$f_r = \frac{1}{2\pi} \sqrt{\frac{k}{m}} \equiv \frac{1}{2\pi} \sqrt{\frac{g}{\Delta l}}, \quad (3.2)$$

where k refers to the spring constant, m to the mass of the entire microscope, g to the gravitation-constant and Δl to the change in length of the springs between the unloaded spring and the equilibrium position [98]. Eq. 3.2 results in $f_r = 1.9$ Hz and external vibrations above 5-8 Hz are already significantly suppressed (Fig. 3.13). To reduce the amplification at the resonance of the spring suspension, an eddy-current damping (ECD) unit was employed. It is positioned below the microscope base as shown in Fig. 3.3. A circular array of 9 SmCo magnets (\varnothing : 15 mm, l: 5 mm, DE155, IBS Magnet) is paired with aluminum fins. Several external noise sources need to be suppressed. The floor vibrations of the building where the experimental setup is located are significant in the low frequency regime with a diffuse noise between 14 and 30 Hz. In addition, a subway nearby excites floor modes at 21 and 54 Hz [99].

The STM base-plate is equipped with a Si-diode for temperature measurements (DT 470 BO, Lake Shore) which is suitable for temperatures as low as 6 K. A small heater that is made up from Kapton[®]-coated stainless steel wire ($\varnothing = 0.12$ mm) wound around a copper winding form can be used to change the microscope's temperature in situ. With a DC resistance of $\approx 300 \Omega$ and a current carrying capability of 200 mA it can dissipate up to 12 W. Electrical connectors for all wires including those necessary to operate the scan-head are mounted in small Macor[®] blocks and can be disconnected for maintenance work.

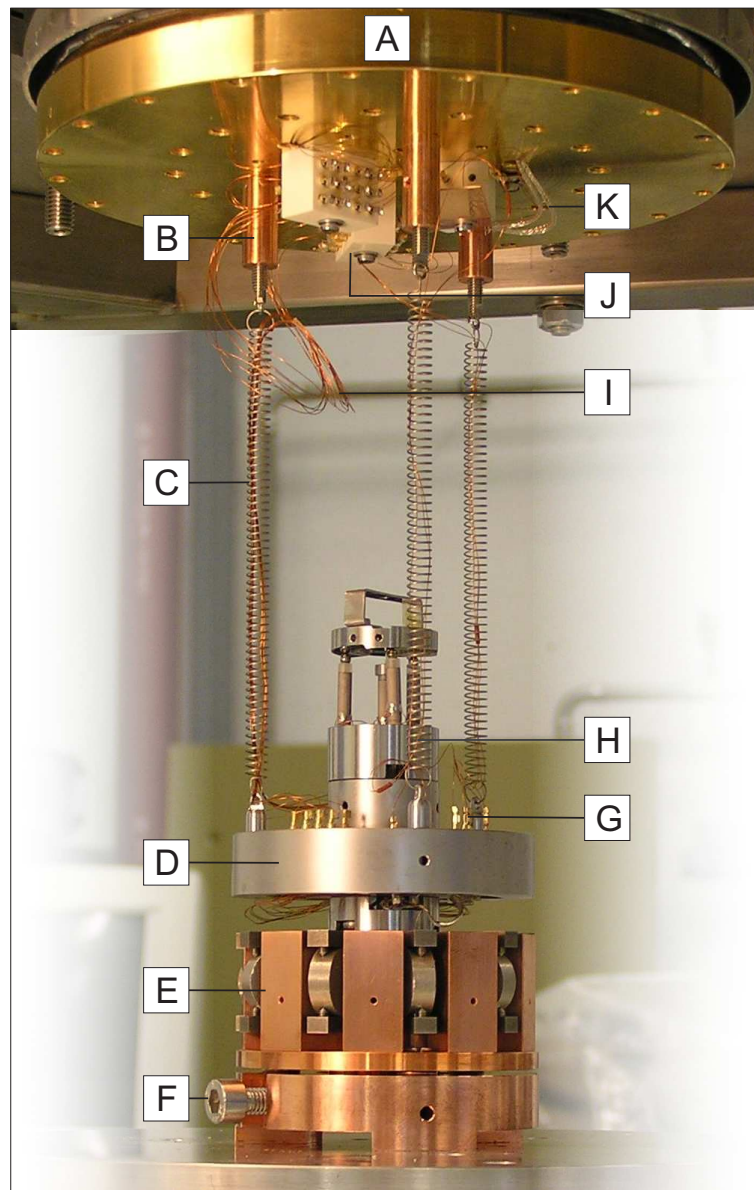


Figure 3.3 Microscope assembly underneath the cryostat, including the vibration isolation: cold plate of the liquid-helium cryostat (A), spring connector (B), suspension-spring (C), microscope base-plate (D), eddy-current damping unit (E), clamping screw for fixing and cooling the microscope (F), electrical connections (G), the scan-head (H), wires (I), ceramics for heat-sinking and isolating the wire connections (J), shielded wire for the tunneling current (K).

At the very bottom of the stage (Fig. 3.8) a copper element can be pushed against the EDC-frame with an allen-key screw (Fig. 3.3 F). This way the microscope can be clamped to establish a thermal contact or simply for fixation. A wobble stick is used to turn the screw.

3.2.2 The Control Electronics

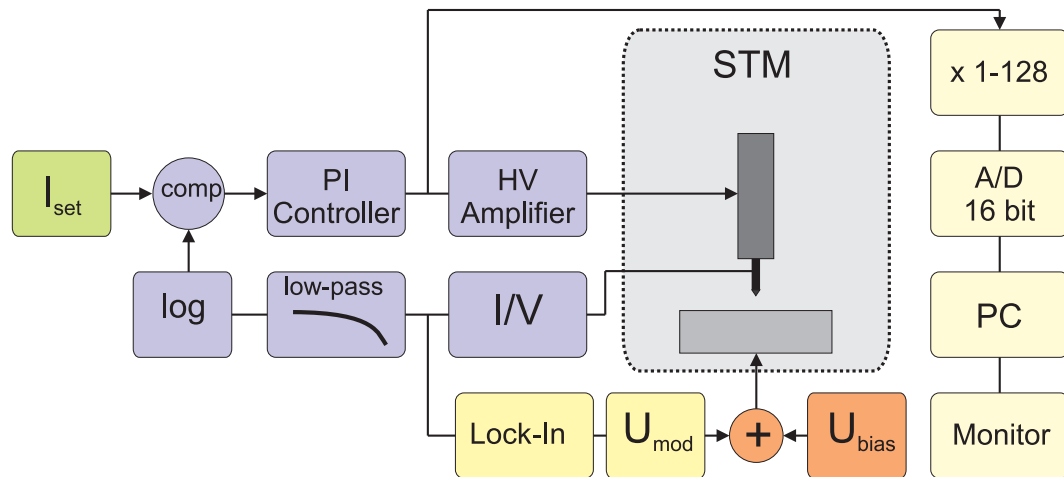


Figure 3.4 Schematic of the control electronics: current set point (green), feedback-loop (blue), microscope (gray), bias and bias-modulation (red + orange), A/D conversion and data processing (yellow)

At the core of each STM experiment is the controlling of the probe-sample distance via the z-motion of the scanner which is commonly done by a well established feedback sequence. For any given set of sample and probe, the width of the tunneling junction is a function of the bias-voltage and the current. The usage of a specific DC bias-voltage leaves the current as the determining component³. The scheme of the circuit is shown in Fig. 3.4. The current flowing through the junction is converted into a voltage by the preamplifier, filtered, potentially amplified and send into the comperator. Optionally, a logarithmic stage can be put between the I/V converter and the comperator to counteract the exponential dependence of the current from the gap width and to reduce the loop-response for large gap variations. The real current (or, to be exact, a voltage representing the current) is compared to the set-point, generating an error signal that is fed into a PI controller to adjust the response of the loop. The output is forwarded to the high-voltage amplifier that controls the position of the tube-scanner

³The bias modulation during conductance mapping is done with frequencies that exceed the feedback response.

and thus the gap width. It is obvious that the signal for controlling the scanner is changing as long as the tunneling current deviates from the set-point.

A constant-current image, being the imaging mode used exclusively throughout this work, is constructed from the regulation signal after the PI controller. A 16 bit A/D converter processes the signal. By default, the 16 bit are covering the entire output range of the PI controller (-10 V to +10 V). To improve the resolution, the signal can be amplified prior to the A/D conversion. At maximum amplification, the 16 bit are covering a range of +/- 78 mV, resulting in a nominal resolution of 22 bit. Most of the measurements in this work have been done on surfaces with corrugations of less than 1 nm. To achieve the highest possible resolution, the (large) DC component of the regulating voltage was subtracted from the signal entering the A/D converter, allowing for the (small) AC component to determine the usable 16 bit range.

All electrical signals of relevance are generated, modulated and detected by a commercial SPM controller (SPM 100, RHK) and a lock-in amplifier (7265 DSP, Signal Recovery). In addition, a sampling oscilloscope (TPS 2014, Tektronix) serves as monitor for tunneling current and z-position. In this design, the application of the bias voltage to the sample was favored. The bias is made up of two voltages: a DC voltage which is generated in the SPM 100 controller and a AC voltage which is output by the lock-in amplifier and is of relevance for dI/dV and dz/dV spectroscopy. The tunneling junction itself can be regarded as a variable resistor and a more or less constant capacity⁴. The current through the junction is fed into a preamplifier where it is converted into a voltage. Two different amplifiers were available (IVP 200/300, RHK) with a conversion of 0.1 V/nA and 1 V/nA, respectively. A second stage provides options for several signal adjustments. The differential input section allows for offset elimination and amplification by 1, 10 or 100, followed by a -6 dB low pass with selectable cut off frequency between 0.5 and 50 kHz. A DSP inside the main control unit generates almost all signals of relevance for imaging and spectroscopy. This includes the x/y voltages for scanning and lateral tip positioning, the adequate waveforms for sample positioning via support-piezos and a variable bias voltage. (In addition, those signals that were converted by the A/D card are processed here before they are transferred to the computer.)

3.2.3 The UHV System

The UHV system is formed by two separate chambers which are connected via a gate valve (CF 100, Hayward). An overview of the setup is given in Fig. 3.5. The experimental unit consists of the cryostat (CryoVac), the STM chamber (Pink) and an ion pump (Low Profile 200, Gamma Vacuum) with built-in titanium sublimation pump (TSP-IGP, Vacom). The pressure of typically $5 \cdot 10^{-11}$ mbar is measured with an

⁴In some cases it was helpful to compensate for the parasitic capacitance by adding the AC signal from the LIA with a 180° phase shift via a small capacitor to the input of the I/V converter [100].

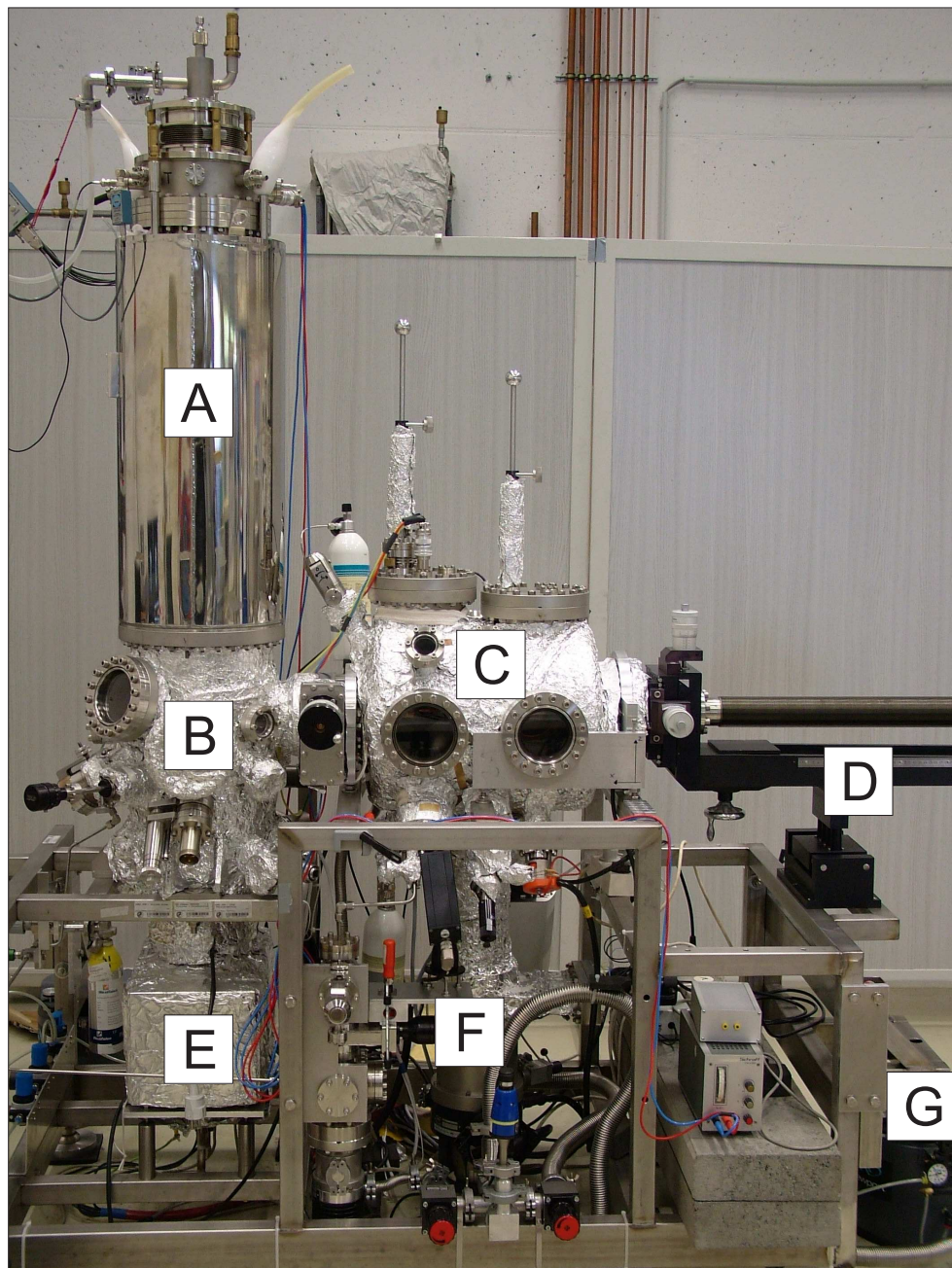


Figure 3.5 The UHV system: cryostat (A), experimental (STM) chamber (B), preparation chamber (C), main manipulator (D) ion-pump and Ti-sublimation pump (E), turbomolecular pump (F), air-leg (G).

ion gauge (Ionivac IM520, Leybold). The preparation chamber (Pink) incorporates a turbo molecular pump (Turbovac 340M, Leybold) and the main manipulator (PM 12-750, VAb). The pressure ranges around $6 \cdot 10^{-10}$ mbar and is monitored by another ion gauge (Ionivac IM221, Leybold). A stainless steel frame (FHI workshop) carries the entire UHV assembly. For vibrational isolation, an air-leg system (XL-A, Newport) was employed. The details will be described further below.

The STM Chamber

The starting point for designing the chamber that houses the STM was the arrangement of additional experimental techniques and application around the microscope so that each device would have visible access to the tip-sample junction. Fig. 3.6 shows a sectional drawing of the chamber and the helium-cooled shield to illustrate the allocation. The perspective of this view is in accordance to the connection axis of both vacuum chambers. For better visibility one suspension spring has been removed from the sketch.

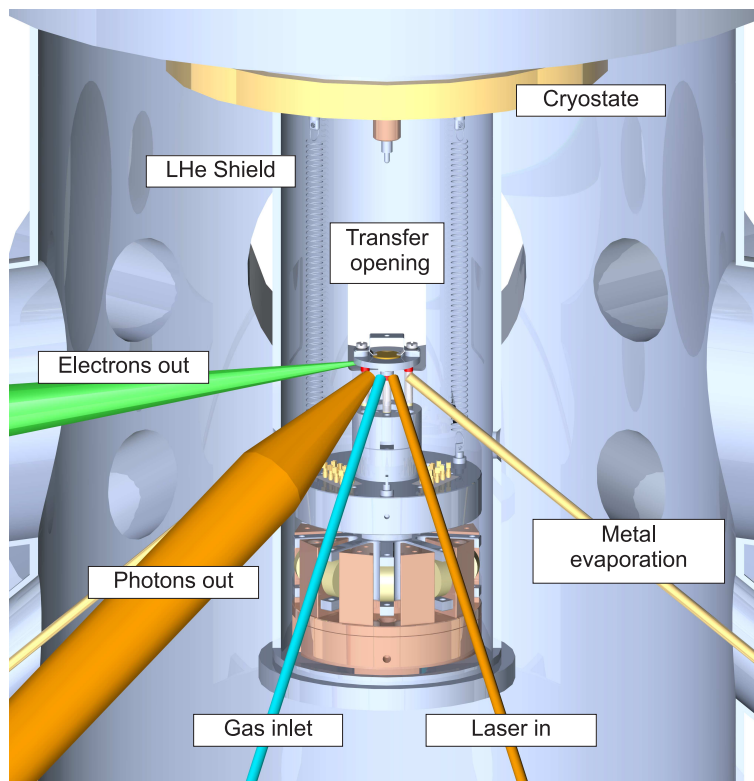


Figure 3.6 Cutaway view of the microscope inside the radiation shields and the pathways for different experimental applications.

The square opening in the back of the cryo-shield serves as door. It is aligned with

the x-axis of the manipulator and utilized for tip and sample exchange. The positions of all other applications are listed in Tab. 3.1 using the door as origin of the coordinate system. Their arrangement is demonstrated in Fig. 3.7. The individual components are described in more detail below.

Table 3.1 Positions of the openings within the radiation shields to access the sample inside the cryostat.

Position	Purpose
0°	– Door
90°	– Metal evaporator
135°	– Wobble stick (figure 3.7)
135°	– View port (figure 3.7)
165°	– Laser window
195°	– Gas inlet
225°	– Photon collection
270°	– Metal evaporator
270°	– Electron analyzer

The Cryostat

The demand for an easily accessible tunnel junction has led to the decision to use a top-mount bath cryostat (CryoVac). This system is composed of a 8.5 L dewar for liquid helium surrounded by a second dewar holding 19 L of liquid nitrogen. Both can be filled from above. To lower the helium consumption, the helium exhaust line is equipped with a recuperator which uses the cold gas to cool two baffles in the form of aluminum disks. The upper baffle reaches a temperature of ≈ 70 K, while the lower one levels off at 30 K. The helium vessel is surrounded by an additional shield of high-purity aluminum which is connected to the 30 K baffle. According to Stefan-Boltzmann's law $P = \sigma \cdot A \cdot T^4$ the additional shield reduces the radiation load on the cryostat from 49 mW/cm² to 0.01 mW/cm².

The microscope is suspended from the bottom of the helium dewar, which is made of a gold-plated copper disc with 160 mm diameter (Fig. 3.3). Also mounted to the dewar-bottom is an aluminum-can which is housing the STM to protect it from infrared-radiation. To lower the helium consumption even further, a second aluminum can which is heat sunk by the nitrogen dewar encloses the helium-cooled shields. The view from below (Fig. 3.8) elucidates the concentric array of He-cooled and N-cooled escutcheon. Access to the sample inside the microscope is provided by a number

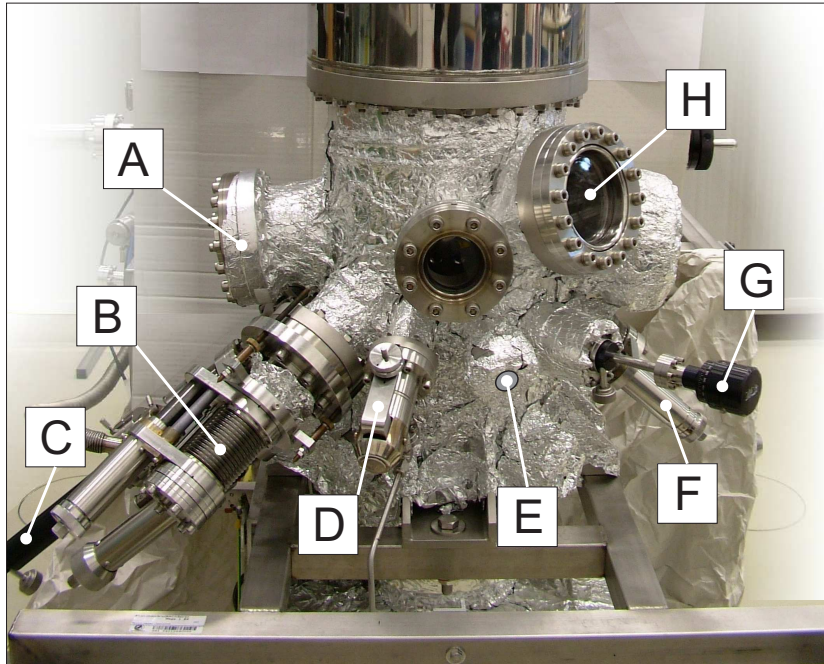


Figure 3.7 Positions of the experimental applications and components on the STM chamber: port for connecting the electron energy-analyzer (A), optical lens-assembly for photon collection from the tunneling junction (B), metal evaporator (C), gas-doser (D), window for coupling to a laser (E), metal evaporator (F), wobble stick (G), main view-port (H).

of openings in the radiation-shields. These openings are lining up with four main directions. A rotating aluminum shutter can be activated via wobble-stick to close the ports and seal the enclosure. A detent that snaps in every 15° keeps it aligned with the required positions.

Special care had to be taken for the wiring since their thermal conductance plays a major role in helium consumption. In addition, maintenance was simplified by arranging the wires in sections. The wire material and diameter was optimized for lowest thermal conductance. Besides the coaxial cables for bias and current, which are split into two segments each, all wires are sectioned in three parts. The first segment starts from a CF 16 feed-through at room-temperature and terminates at a ceramic heat sink (Shapal[®]) which is mounted to the lower side of the upper baffle at 70 K. From there the wires are guided through 3 thin tubes in the dewar to be heat sunk at 4.2 K by another Shapal[®] element at the bottom of the helium vessel. For the main signals to and from the tunneling junction coaxial wires have been chosen, consisting of semi-rigid stainless steel capillaries (\varnothing : 0.5 mm) with a PTFE dielectricum and a 0.08 mm stainless steel core (UT-020-SS, Micro-Coax). The wires for operating the STM are Kapton[®]-isolated stainless steel wires (KAP4K-04, \varnothing : 0.14 mm, Caburn). Only the wire for the heating coil is made from copper (KAP012, Caburn) for lower

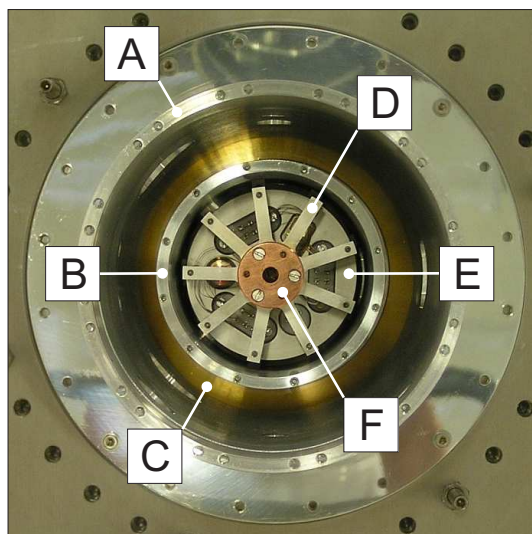


Figure 3.8 Bottom view of the microscope inside the radiation-shields (shield end-plates removed): liquid-nitrogen cooled shield (A), liquid-helium cooled shield (B), cryostat cold-plate (C), magnet array for eddy-current damping (D), microscope base-plate (E), anchor for cooling and clamping.

electrical resistance.

As result of these measures, the He-consumption has been reduced dramatically. The amount of helium required for the initial cool-down from the LN₂ value of 80 K to 10 K amounts to 10 L. Once the final temperature is reached the cryostat displays ultra-low helium consumption of 1.1 to 1.2 L LHe per day. This allows to measure for about one week without refilling the dewar. The nitrogen vessel has to be refilled every 36 hours, which is executed by an automated system.

The Metal Evaporators

The investigation of nucleation and electronic properties of small metal particles as the active species in model catalysts requires the dosage of small amounts of metals onto a sample at temperatures below 20 K to reduce the diffusion and avoid sintering. Ideally the oxide film which serves as support can be investigated by STM before metal deposition by keeping the same sample position inside the microscope. For this purpose two evaporators were developed. Both are based on tungsten filaments which are formed to coils. Short wires of the relevant metals are wound around the filaments and annealed close to the point of melting. This results in formation of small metal beads which produce homogeneous evaporation conditions when the filament is heated. The installation angle is 45° relative to the sample surface normal. Linear z-motion stages facilitate positioning of the filaments close to the nitrogen shields. One of the evaporators allows exchange of the metal without breaking vacuum. To do so it can be retracted as far as 170mm, separated from the STM chamber by a CF 35 gate valve and pumped by a separate turbo-molecular pump.

The Gas Inlet

Via a leak valve (Varian) gases can be dosed into the STM chamber. A coarse valve reduces the pressure of the gas bottle from 50 bar to 0.1 bar. The leak valve allows dosages in the range of 10^{-9} mbar. The lines between both valves can be evacuated either by a rotary pump alone or in combination with a turbo-pump. Any air that enters the system during exchange of the gas supply can be eliminated this way. One of the frequently used gases, CO, reacts with the stainless steel tubes and forms nickel carbonyls. Therefore, the gas lines are emptied out while not in use.

The adsorption of most gas-molecules at temperatures as low as 10 K requires a direct transmission path from the valve to the sample surface. Hence, the shutter of the nitrogen-cooled radiation-shield can be opened and the molecules can reach the sample under an angle of 30° relative to the sample surface.

The Laser Port

The laser light is produced by a Nd:YAG laser (HY 200, Lumonics). Besides the fundamental emission at 1064 nm the second and third harmonics at 532 nm and 355 nm are available for experiments. The light is guided via a mirror system (Thorlabs) to the STM chamber where it enters the vacuum via a sapphire window and reaches the sample surface at an angle of 30° in reference to the sample plane.

The Optical System

Investigation of photon emission from the tip-sample junction provides complementary information of local surface properties. A correlation with feature at the atomic scale was already achieved [101]. As described in Sec. 2.2.2, the fundamental difference between conventional STM and photon emission measurements is the conversion from tunnel-electrons into photons via inelastic processes. The quantum efficiency i.e. the number of photons generated by one tunnel-electron depends on the emission process [77] and ranges typically between 10^{-8} and 10^{-4} which exceeds the efficiency of inverse photo-electron spectroscopy (IPES) by several orders of magnitude [102].

The light emitted from the tip-sample region can be regarded as a point-like source with a spatial extension comparable to the wavelength. One main requirement common to all optical systems is to maximize the number of photons at the entrance of the detector. Several ways to accumulate the radiation have been employed by different groups, including collection into a fiber with [103] and without [104] linear polarizer, placing the tunnel junction in the focus of an ellipsoidal or parabolic mirror [102, 105] and guiding the light via lenses [106–108].

The low-temperature setup induces some extra challenges for the photon collection. In particular the positioning of the junction with respect to the focus of the collecting system is demanding. Vertical displacements due to thermal contractions of the dewar and the suspension and horizontal displacements resulting from the allowance of the

tip exchange mechanism require compensation. Hence, a lens system with several alignment stages seemed to be suitable.

The present design is simply based on two lenses. The first lens (UV grade fused silica, \varnothing : 25.4 mm, f: 63 mm, Lot Oriel) is placed inside the vacuum, right outside the helium-cooled shield. The angle of the orifice axis was selected to be $\theta = 30^\circ$ with respect to the sample surface, the direction where maximum photon emission from the tunneling junction has previously been observed [76].

In order to minimize the 300 K radiation onto the microscope the optical path is shielded by a quartz window (\varnothing : 22 mm, Lot Oriel) which is mounted to the radiation-shield. The first lens acts as a condenser with the tip apex in its focus. The parallel beam is relayed via a viewport (UV grade fused silica, CF 35, Vacom) outside of the UHV. A second lens focuses the beam into the center of a small x/y-stage for lateral adjustment of the following instruments which is either a photomultiplier tube (H9306, Hamamatsu) for integral photon measurements or a spectrometer/CCD combination (Triax 180, gratings: 1200/mm, 300/mm or 150/mm, Jobin Yvon) for wave-length selective analysis. The alignment of the lens unit can be done by two components, one with angular motion one that varies the lens-junction distance.

The Electron Analyzer

The identification of chemical properties with the STM is not as straight forward as the interpretation of the topographic features [109]. Even though the tunneling current always includes the combined information of the spatial extension and the local density of electronic states, images are commonly referred to as topographic representations of the surface. Most of the element specific information are generated by tunneling into distinct electronic orbitals, discrete atomic levels or surface states. Another chemical fingerprint are molecular vibrations which have been successfully investigated by IETS. An impeccable chemical analysis requires access to core level excitations, as exploited in X-ray photo-electron spectroscopy and Auger-electron spectroscopy. However these methods do not commonly exhibit spatial resolution. Alternatively, scanning Auger microscopy provides local information but at the expense of significantly higher electron energies in the range of 10 to 30 keV.

It is therefore appealing to make use of the STM as local electron emitter and to collect the backscattered electrons in the far field into an energy analyzer similar to EELS or AES experiments. This idea was brought forward first by Reihl and Gimzewski [36]. By positioning the tip in close proximity to the surface and applying a positive bias voltage that significantly exceeds the work function electrons are accelerated along classically allowed trajectories and interact with the sample. Scanning the probe across the surface can be employed to produce chemical maps e.g. by collecting specific Auger electrons during the scan. The setback of this method is related to the interdependence of tip-sample distance, electron current and bias voltage. The higher the bias, the further the tip has to retract to stabilize a given current. This

leads to a loss of spatial resolution. A narrow tunneling gap on the other hand can only be achieved by keeping the bias low or allowing currents above a critical value. Nevertheless people have been successful with this approach both in the low energy regime [37] as well as at high energies [110].

One flange of the STM chamber has been dedicated to a hemispherical mirror analyzer (Vacuum Generators). Electrons emitted from the sample pass through a slit in the cryo-shield. They continue to the entrance of an electronic lens which focuses them into the analyzer. The acceptance angle of the lens is $\theta = \pm 12^\circ$. The strong and inhomogeneous electrical field between tip and sample results in electron trajectories which are severely back-bend toward the surface. The final energy as well as the exact emission spot and angle play a decisive role whether or not an electron can escape at all. Nowadays, it is believed that only electrons from the fringe area of the irradiation cone contribute to the signal [37]. Consequently, significant currents can be detected only by positioning the lens almost parallel to the sample plane. Due to the geometry of the sample-holder and the acceptance angle of the electron lens the analyzer is positioned with $\theta = 8^\circ$ relative to the surface plane. Another way to further increase the current in the far-field is the suppression of the local field to prevent electron deflection. To implement this, the tip gets an additional electrode in coaxial configuration, which is either connected to grounded or to its own bias-voltage. A special tip holder that incorporates the extra contact can be placed on the scanner where it connects to a coaxial cable leading to a feed-through on the UHV chamber.

3.2.4 The Preparation Chamber

Besides the chamber that houses the STM, a separate chamber was designed which serves multiple purposes. A load lock in combination with a transfer-rod (MDS40-400, VAb) allows the transfer of tips and samples into the chamber. The branch is separately pumped by a small TMC (Turbovac 50, Leybold). Presently, up to three samples and two tips can be stored inside the vacuum. A quadrupole mass spectrometer (QME 200, Pfeiffer) enables the determination of the composition of residual gases.

The Manipulator

Inside and between the vacuum chambers, samples are transported with the main manipulator which is shown in Fig. 3.9. An extension length of 750 mm was required to bridge the largest distance located between sample storage and STM. The carrier piece at the end of the manipulator (Fig. 3.9 C) is manufactured from oxygen-free high-conductivity copper (OFHC) for the best electrical and thermal conductance. Ceramic washers disconnect it electrically from the ground potential. For cooling, liquid nitrogen can be pumped through capillaries. The tubes lead to a small tank which is mounted at the lower side of the copper-carrier. This little dewar serves as

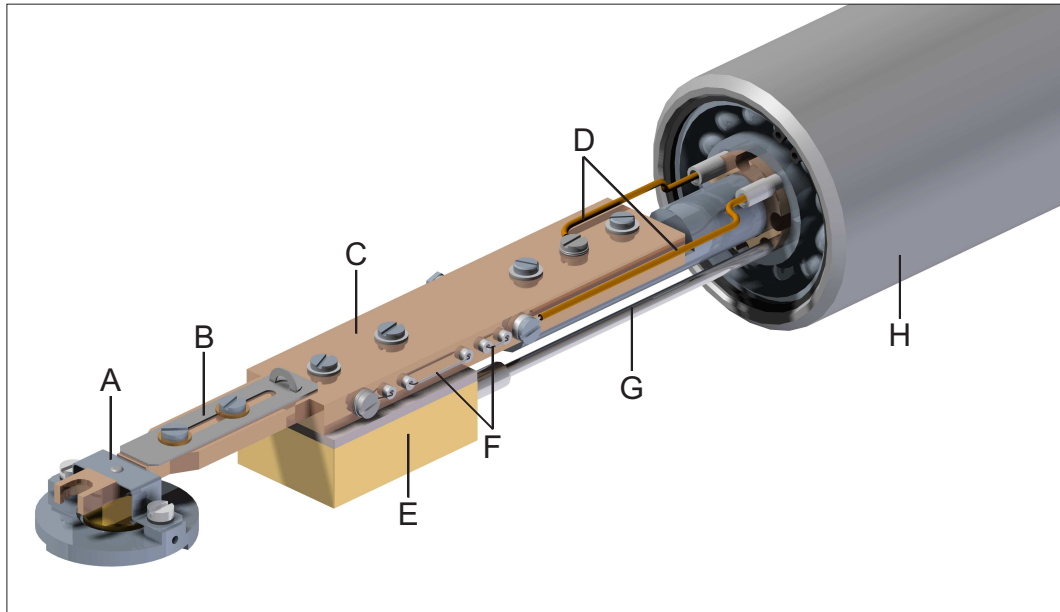


Figure 3.9 The main manipulator: sample-holder with hook (A), locking mechanism to fix the sample during manipulator rotation (B), copper element (C), Kapton-isolated wires for low- and high-voltages (D), tank for cooling with liquid nitrogen (E), tungsten-filament for heating (F), capillary for cryogen supply (G), support tube (H).

heat exchange and maximizes the contact area. Temperatures around 90 K are reached after approximately 30 minutes. A filament made of 0.1 mm tungsten wire is held in place by ceramic tubes enables heating of the copper piece. Both ends of the filament are contacted separately by Kapton-coated wire. High voltage can be applied via the same conductors. The temperature is measured via a chromel-alumel thermocouple which is connected to the copper piece near the sample retainer.

The sample is picked up into a receptacle which centers and aligns the hook (see Fig. 3.1). This way the sample arrives at the microscope in a well defined position. A locking mechanism fixes the sample holder to the manipulator and allows turning the sample to face the LEED/AES system and the evaporators.

Tip Exchange

There are some obvious reasons to abstain from the option of in-situ tip exchange. The additional weight added to the scanner lowers the eigenfrequency and limits the maximum scan speed as shown in figure 3.2. Concomitantly with larger dimensions of the tip holder comes a parasitic capacity. Hence, bias modulation during dI/dV spectroscopy generates an increased signal which is not related to the tunneling process and has to be compensated externally. In spite of this, the reasons to include such

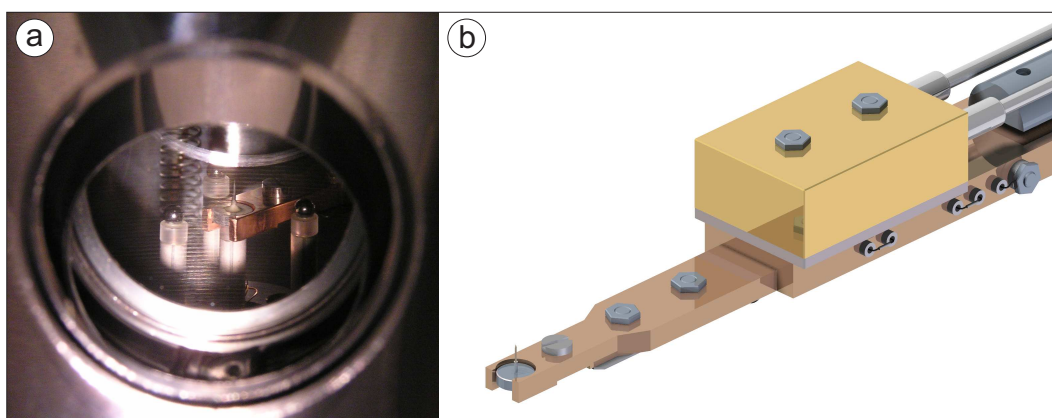


Figure 3.10 Tip exchange with the manipulator: (a) View through the window inside the radiation-shields onto the tip carrier and the manipulator end-piece, (b) the manipulator in orientation to perform a tip exchange, holding a tip carrier.

a mechanism prevail. For a low temperature system the procedure of changing tips *ex situ* is laborious and the warm-up time consuming. Experiments related to photon emission from the tunnel junction are sensitive to the tip material. While most probes for common investigations are made from either tungsten or platinum-iridium, silver and gold are the materials of choice in conjunction with photon emission experiments. As described in section 3.2.3 experiments associated with electron emission require a shielded tip and an additional contact at the tip-holder. In summary only a probe exchange mechanism would enable the variety of experiments aimed for in this thesis.

For the exchange procedure the copper extension at the end of the manipulator has to be rotated by 180° to accommodate the tip-holder, which then rests 2 mm deep inside a pocket (Fig. 3.10). For installation, the manipulator is extended until the tip-holder is located right above the scanner. The microscope is not locked during the exchange procedure so that forces to the tube-scanner can be avoided. The distance between the holder and the magnet inside the piezo is decreased until the microscope spurts upwards and connects to the holder bottom via magnetic force. The guide in the manipulator centers the tip-holder within a margin of 0.2 mm. For removal, the guide is placed below the tip where the opening surrounds the scanner. The electrodes around the piezo serve as contacts to indicate the position. The manipulator is moved upwards until the weight of the microscope disconnects the contact. After the exchange the tip can either be prepared *in situ* inside the preparation-chamber or removed from the system through the load-lock.

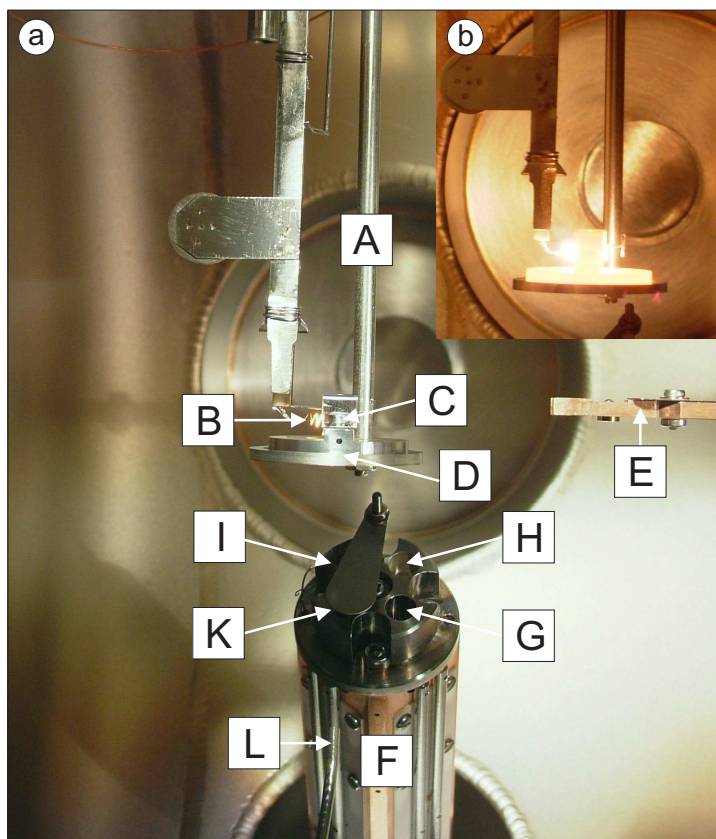


Figure 3.11 (a) Sample preparation stage: high voltage supply (A), tungsten-filament (B) sample holder (C), molybdenum plate to support and protect the sample holder (D), manipulator end-piece (E), four-pocket evaporator (F) filled with Fe (G), Ag (H), Si (I) and Au (K), capillary for oxygen dosing (L). (b) Preparation-stage in heating mode.

Sample Preparation

Most of the preparations take place at a separate stage apart from the manipulator. Here, the sample is placed on a molybdenum support which is located in the focus of a sputter gun (IQE 11-A, Specs), a capillary doser for oxygen, a 4-pocket evaporator (Oxford Scientific) and a pyrometer (MI 16, Sensortherm). Annealing is done by an electron beam that is emitted from a tungsten filament and accelerated with up to 2 kV towards the back-side of the sample. Temperatures as high as 2300 ° K can be achieved this way. Samples are cleaned by repeated cycles of sputtering with argon ions and annealing to heal and flatten the surface. The deposition of metals can be done either while the sample rests in the heating stage or, if cooling is indicated, with assistance of the manipulator. A four-pocket evaporator provides silicon, silver, iron and gold as ad-materials. In addition, lithium can be evaporated from a resistively heated dispenser (SAES) with a separate device. The initial check of surface cleanness and long-range crystallographic order is done with a LEED/AES system (ErLEED 3000, Specs).

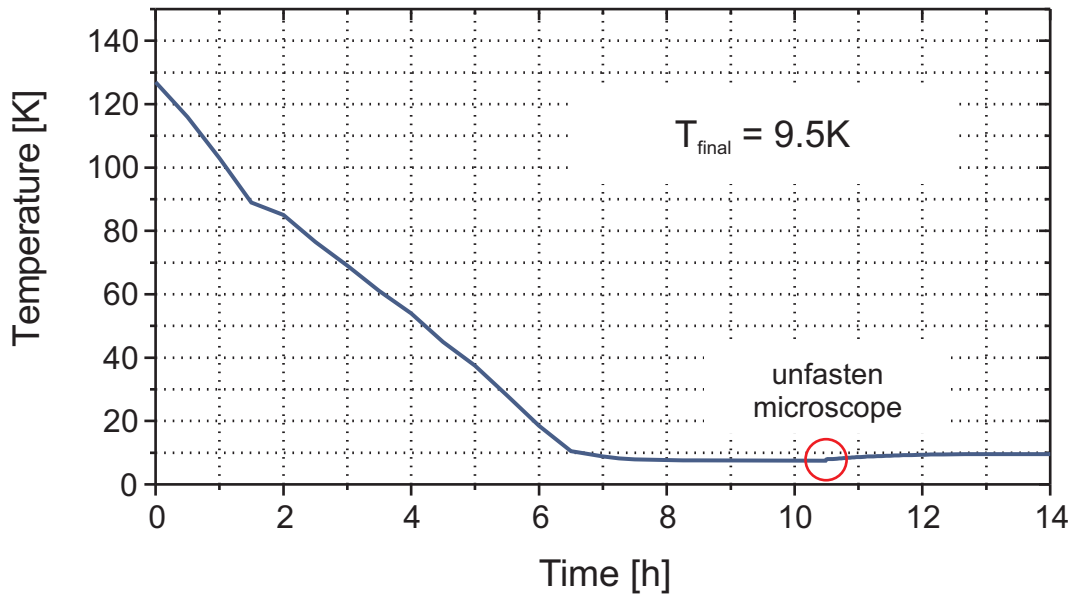


Figure 3.12 Cool-down characteristic of the scan-head from of 130 K to 9 K.

3.3 Performance

This section summarizes the performance of the fully assembled experimental setup and some key characteristics. This includes the cooling process after filling the dewars with cryogenic liquids, the response to external vibrations, the stability of the tunneling junction and the qualities of the scan-head.

3.3.1 Mechanical and Thermal Stability

Cool-Down

The cool down of the cryostat is initialized by filling of the outer dewar with liquid nitrogen. If time permits, 5-8 hours are given for the system to reach equilibrium. The large surface of the nitrogen cooled sections serves as efficient cryo-pump and a pressure reduction of up to 80% is usually achieved. The inner dewar gets pre-cooled with liquid nitrogen as well, which is later removed and replaced by liquid helium. In particular, the large copper plate at the bottom of the vessel has a substantial heat capacitance and the amount of helium that would be needed to cool it down is unreasonable. Therefore, the dewar temperature is reduced to ≈ 80 K prior to the LHe filling. Fig. 3.12 illustrates the temperature progression during cool-down. The starting point of the graph refers to the moment when nitrogen was replaced by helium. The microscope was clamped to the cold frame at 128 K. In the following hours the temperature decreases with almost constant gradient of 16 K/h until arrival at 10 K.

The final temperature of the microscope of 9.5 K is reached after 7.5 h. Unfasten the microscope is of minor impact, leading to an equilibrium temperature of just 0.5 K above the value for the scan-head being in direct thermal contact with the dewar. This alludes to a good thermal connection of the STM base plate via the wires, and to a marginal radiative heat load from the surroundings (Sec. 3.2.3).

Once the system has reached the final temperature, a single filling with helium can last up to 180 h. Due to the extremely low consumption, it is more efficient to keep the system at low temperatures permanently. Hence, both dewars are refilled frequently whether or not experiments take place. Since the surfaces of the dewars and radiation-shields acts as cryo-pump, warming up the cryostat once every three month has been found suitable to release the adsorbate which are then pumped out by the turbo-molecular- and ion-pump.

Vibration Isolation

The vibration isolation is made up by two stages acting in series. The first stage consists of a spring suspension in combination with an eddy-current damping, as described above, which is mounted as close to the scan-head as possible. The second stage is made up by air legs mounted to the sides of the frame (Fig. 3.5). While the air legs are especially dedicated to reduce environmental motions, the spring suspension also reduces the noise that is created within the setup, for instance by turbo-pumps that are kept kept running or by boiling nitrogen. Pumping on the cryogenic nitrogen to solidify the liquid has not been found to be necessary in any of the experiments up to this point.

To measure the influence of each stage on the performance of the scan-head, the tunneling junction itself was serving as the sensor. Once the feedback-loop is disabled, all mechanical excitations that are present will directly translate into changes of the tunneling current. Fourier-analysis transforms $I(t)$ into $I(f)$. Fig. 3.13a-c illustrate the impact of the vibration-isolation stages on the stability of the tunneling junction. The frequency-range of the graph was chosen with respect to Fig. 3.2 in accordance with the lowest eigenfrequencies of the scan head.

Figure 3.13a Both vibration-isolation stages are inactive. The spring-suspension is bypassed by clamping the microscope to the frame with the same mechanism that is used during the cool-down. The air-legs are deflated and their impact is nearly negligible. Only a thin elastomer at the bottom of each air leg stays active for reducing the noise from the building at high frequencies. Plotting the spectral density of the current versus frequency demonstrates that the largest excitations by the ambient noise are found in the low-frequency regime between 1 Hz and 200 Hz. The amplitude can be as high as $22 \text{ pA}/\sqrt{\text{Hz}}$, though the highest peaks of the plot are capped for reasons of easier comparison to the following measurements.

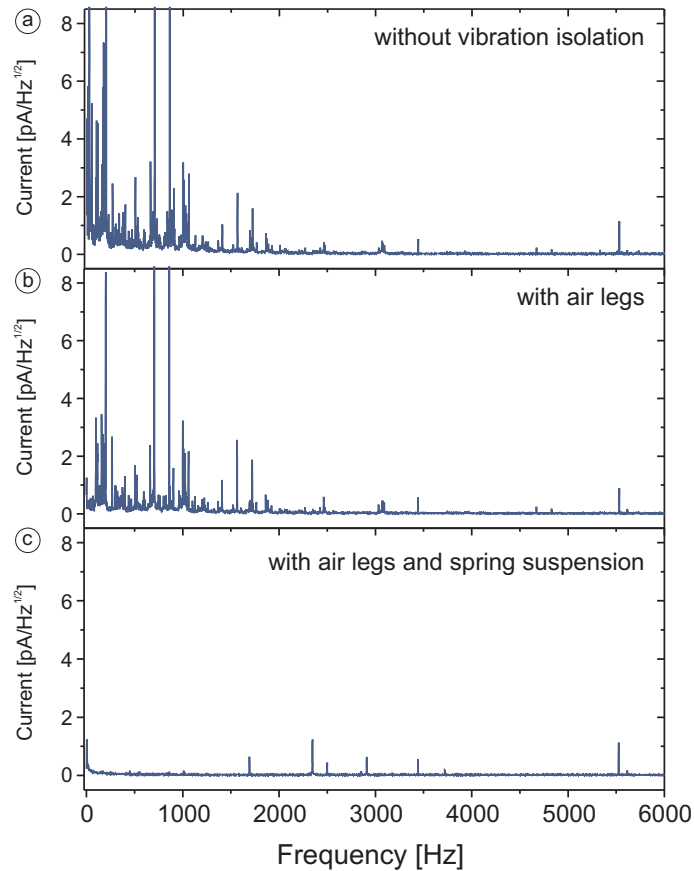


Figure 3.13 Spectral analysis (FFT) of the tunneling current in the range of 0-6000 Hz with and without vibration isolation, showing the impact of mechanical and acoustical excitations on the stability of the tunneling junction: (a) The spring-suspension is locked and the air-legs are deflated. (b) The spring-suspension is locked and the air-legs are active. (c) Both isolation stages are active.

Figure 3.13b The second measurement was done with active air-legs and inactive spring-suspension, resulting in a significant decrease of the noise contributions below 150 Hz. Above this value the noise density remains basically unchanged, supporting the validity of the assumption that environmental noise at higher frequencies is barely transmitted through the ground. The benefits for STM measurements are rather small, improving neither the imaging nor spectroscopy capabilities sufficiently.

Figure 3.13c Both isolation stages are active during the test. The superior performance of the spring-suspension becomes obvious immediately. The majority of noise is efficiently suppressed. Nevertheless, there are some contributions at the low end of the frequency range, a consequence of the resonances of the isolation-stages at 4 Hz

for the air-legs and at 1.9 Hz for the springs, respectively. The origin of several spikes occurring between 1.7 kHz and 5.5 kHz could not be clarified with certainty. The small peak at 3450 Hz actually occurs in all three graphs and is the lowest horizontal resonance of the tube-scanner (Fig. 3.2). The lateral resonance of the three outer piezo-legs is not visible at all. Switching of the TMP had no measurable impact on the graph. A possible explanation for the presence of features at frequencies several order of magnitude above the resonance of the spring suspension lies in the over-simplified approximation of the transfer function. Commonly, only the first resonance is calculated, leading to a transfer function that decreases with ω^{-2} for lightly and ω^{-1} for strongly damped systems. Higher-order modes are not taken into consideration and neither is the non-zero mass of the springs, both resulting in a declining performance at higher frequencies.

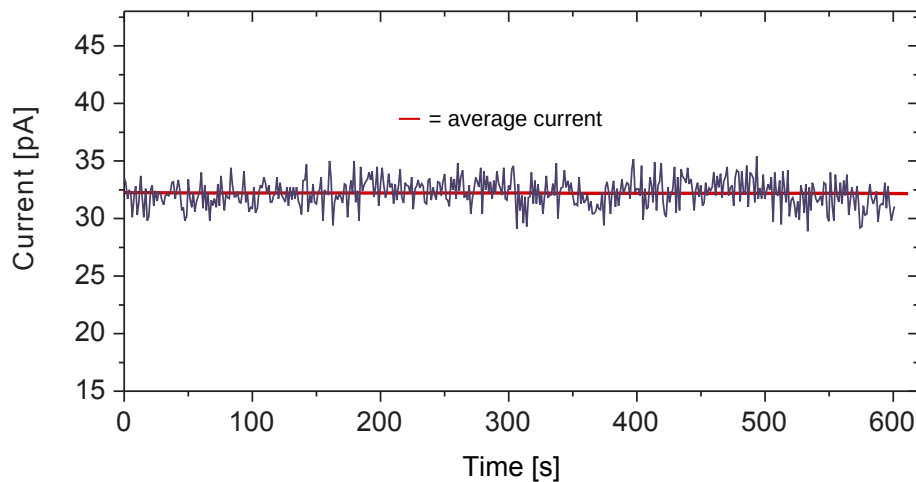


Figure 3.14 Thermal and mechanical stability of the tunneling junction at 9.5 K. After stabilizing the current at 32 pA the feedback-loop was disabled and the current monitored for 600 s. The change of the average current is less than 1 pA over the entire time interval. Both vibration-isolation stages were active.

Ultimately, the efforts taken by cooling the microscope and isolating it from the external noise are supposed to result in a very stable tunneling junction. That this was indeed achieved is demonstrated by measuring the tunneling current at 10 K for 600 s while the feedback-loop was inactive. Fig. 3.14 displays the graph of the current vs. time. The variation of $\Delta I/I$ is less than 10^{-4} .

3.3.2 Imaging and Spectroscopies

The core capabilities of the new microscope were tested using an adsorbate-sample system that was previously investigated by Wallis et al. [31]. Hence, the results can be directly compared to existing data to ensure an appropriate performance.

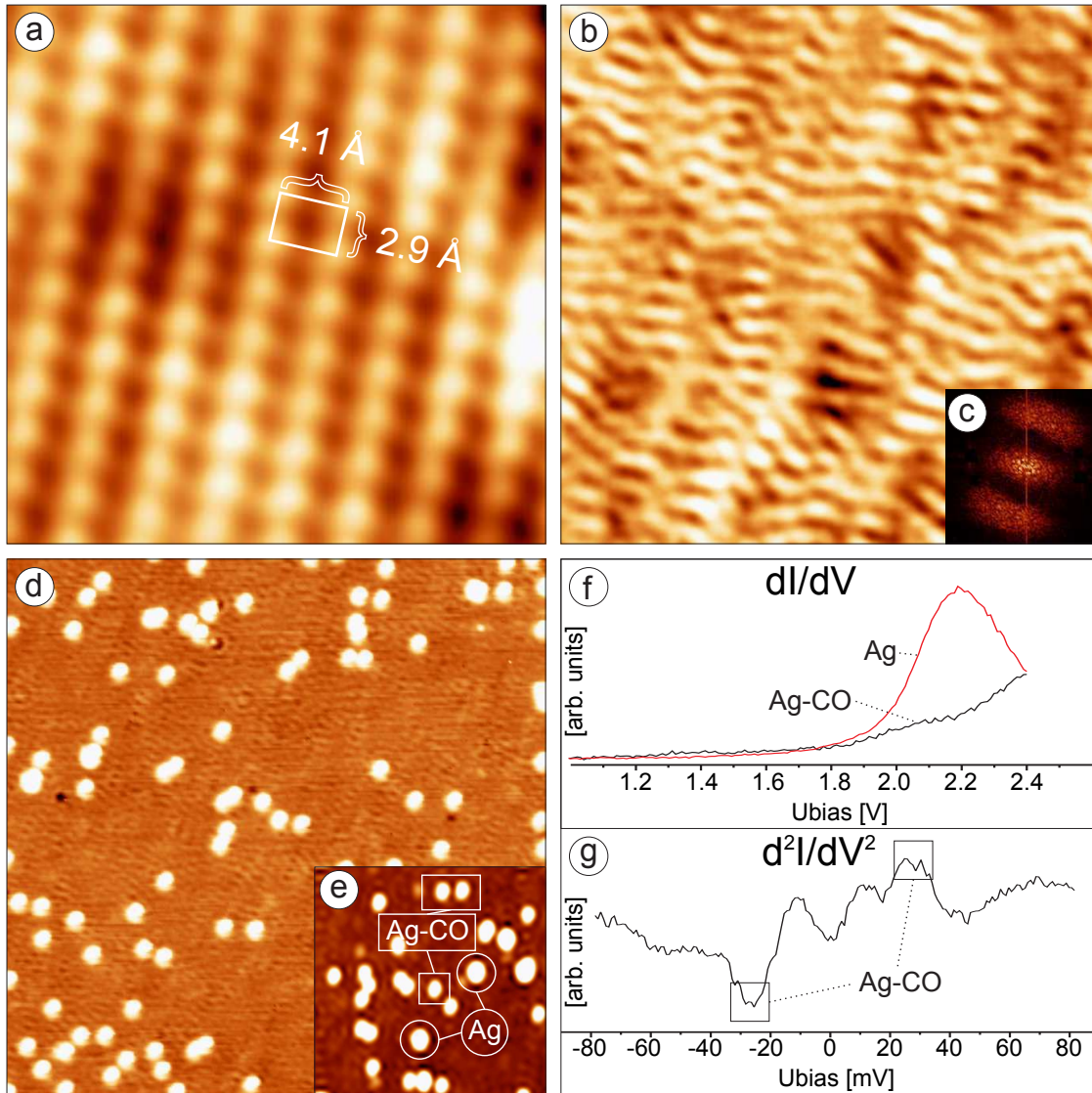


Figure 3.15 Microscope performance regarding imaging and spectroscopy: (a) Atomic resolution of NiAl (110), image: $3.5 \times 3.5 \text{ nm}^2$, $U_b = +240 \text{ mV}$, $I_T = 560 \text{ pA}$ (b) Surface state on NiAl(110), image: $10 \times 10 \text{ nm}^2$ (c) The same surface state in k-space [Fourier-transform of (b)] (d) Ag atoms on NiAl(110), image: $28 \times 28 \text{ nm}^2$, $U_b = +760 \text{ mV}$, $I_T = 124 \text{ pA}$ (e) formation of Ag and Ag-CO after CO dosing (f) Scanning tunneling spectroscopy (dI/dV) of silver atoms and carbonyls (AgCO). (g) Vibrational spectroscopy (d^2I/dV^2) of silver carbonyls.

STM A NiAl(110) single crystal serves as support. Fig. 3.15a shows an image of the atomically resolved surface. Given the rectangular arrangement of the features, only one atomic species is visible in the image. It is generally believed that STM preferentially detects the Al atoms which protrude a few picometer from the surface. The unit cell measures 0.41 nm in $(1\bar{1}0)$ direction and 0.29 nm in (001) direction and is identical for both atomic species. These numbers were used for the calibration of the lateral response of the tube-scanner, while mono-atomic steps on the NiAl(110) crystal with a height of 2\AA were used to calibrate the sensitivity in direction of the surface normal, respectively. It is well known that piezoelectric coefficients change with temperature and the response of the tube-scanner made of EBL No. 2⁵ changes its response between 300 K and 10 K by a factor of ≈ 0.2 , leading to a sensitivity of 0.6 nm/V normal to the surface and 3.8 nm/V in plane. The small corrugation of metal surfaces is representative for the smallest features that can be resolved with the microscope. The NiAl(110) surface features a number of surface states (SS) which mix into the topography. Such a state can be seen in Fig. 3.15b. The original STM data is a superposition of Fig. 3.15a and b. To separate them, a Fourier filter was applied, removing the contributions from the surface state in Fig. 3.15a and from the surface atoms in Fig. 3.15b. The inset (c) was received by Fourier transformation of image (b) and displays the k-dependence of the SS at this particular bias voltage. A detailed analysis of the SS was done by Hansen and can be found in [111].

The following step was the deposition of silver atoms onto the cold sample surface with the sample remaining inside the microscope. One of the previously described evaporators was heated for 90 seconds until a steady flux was achieved. The deposition on the sample was controlled simply by using the shutter of the radiation shields to open and close a small penning. The Ag atoms and the scattering of the SS due to the presence of the deposits can be seen in Fig. 3.15d.

STS Finally, CO was released into the chamber. The high sticking coefficient of CO at low temperature requires visible access to the sample for the molecules to reach the surface. This was done by opening another small penning inside the radiation shields. The STM chamber was back-filled with $5 \cdot 10^{-9}$ mbar CO and the port was opened for 60 seconds. Adsorption takes place almost exclusively on top of the Ag atoms with a coverage of approximately $0.1/\text{nm}^2$. The apparent height of the Ag-CO complex is dependent on the bias voltage which makes a clear distinction from the Ag atoms possible. Tunneling spectroscopy performed on a Ag adsorbate shows a resonance at an energy of 2.2 eV which is quenched on a single AgCO (Fig. 3.15f). The resonance reflects the Ag 5s orbital that changes position and spatial extension with the CO molecule [31].

⁵Industry-type PZT 5A.

IETS One of the ultimate tests for the quality of the STM is the performance of vibrational spectroscopy. The excitation of a vibrational mode opens an additional channel for electron tunneling yet the contribution to the total current is usually so small that its measurement literally defines the detection limit. Fig. 3.15g shows a spectrum taken on an AgCO complex that was acquired by averaging the second derivative of 4 scans in the energy range of -80 meV to +80 meV. Two features appear with the characteristic point-symmetry around zero at + 26 meV and -26 meV and are assigned to the hindered rotational mode of the CO molecule on the Ag. In general, bonding between CO and transition metals is explained by the Blyholder model, stating that electron density is donated from the filled 5σ orbital of CO to an empty s -like metal orbital and back-donated from the d -orbitals of the metal to the $2\pi^*$ orbital of the CO molecule [112]. The quality of the acquired IETS data is satisfactory considering the averaging of only a few scans.

Other Spectroscopies

At the time of writing this thesis, both, the photon detection and the far-field electron detection has not yet been established. The UHV related part of the optical system together with the external lens was completed and briefly tested. In addition, the response of the microscope to the additional thermal load from the openings in the radiation-shields for the photon detection was tested. The inner, helium-cooled shield-opening is covered by a sapphire window which limits the exposure to 300 K radiation. However, the outer opening is unprotected and close to the first lens being at 300 K. Still, the microscope reaches a new equilibrium temperature that is only slightly higher than before (20 K). Unfortunately, this is accompanied by a considerably higher LHe consumption.

4 The Influence of Substrate Steps on Oxide Formation: A Thin Alumina Film Grown on a NiAl Vicinal Surface

4.1 Introduction

This study was motivated by the desire to not only use oxide films in their native form, but to go a step further and modify and tune their surfaces concurrently with their chemical properties. Oxides have been successfully grown on metal surfaces as templates for model catalysts [9, 10, 56]. The controlled structuring of surfaces at the nanometer scale provides a way to design new functionalized materials as they find their applications in electronic devices and heterogeneous catalysis.

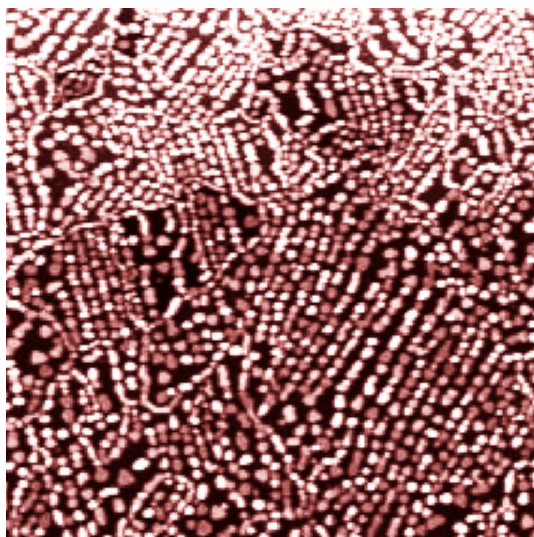


Figure 4.1 Nucleation of palladium atoms along the antiphase domain boundaries of Al_2O_3 [15].

One approach to manipulate and pattern a surface is by the use of external processes which have been scaled down to the nanometer range. Representations are laser-beam assisted deposition [113], electron beam lithography [114] or local manipulation with the probe of a STM [115]. Common to these methods is the little dependency on internal material properties but instead the challenge of control fabrication at small dimensions. Another way to fashion surfaces with well defined characteristics is by exploiting internal material properties. At the nanometer scale this aims specifically at self-organization.

Gambardalla et al. initiated self organization by depositing Cobalt onto a Pt(997) surface, fabricated by cutting a crystal along a high index plane to produce a regular step pattern, to investigate magne-

tocrystalline anisotropy. The cobalt forms atomic rows along the step edges enabling a deposition-dependent transition from a 1-dimensional (wire) to a 2-dimensional (layer) system [116]. In another experiment Neel et al. used an Au (433) vicinal surface to deposit C_{60} fullerenes onto it. While deposition at room temperatures with sub-monolayer coverage led to a mainly disordered adsorption preferentially along step bunches, annealing the substrate changed the arrangement of both the C_{60} molecules and the surface step pattern. Triggered by the higher temperatures, self-organization resulted in hexagonally arranged fullerenes on step bundles with decreased step width that was now self-adjusted to optimally support the adsorbate pattern [117].

Heteroepitaxial systems can develop misfit-induced relaxation networks [118, 119]. The deposition of material onto a substrate with a slightly different lattice constant introduces strain that unloads into dislocations. Due to mutual long-range repulsion and high mobility at the surface, the dislocations often arrange into highly ordered periodic patterns. This enables fabrication of periodical, two-dimensional nano-structured arrays through nucleation of deposited metal atoms. Brune et al. demonstrated the feasibility of this self-organized growth method for Fe islands on a Cu bilayer on a Pt(111) substrate, and for Ag nucleation on a bilayer of Ag on Pt(111)¹ [118]. Becker et al. investigated the growth of copper-group elements and additionally Mn and V on an Al_2O_3/Ni_3Al template. It is believed that a well ordered dot pattern that can be seen with STM arises from a slight mismatch between the metal crystal and the oxide film [119].

Yet another mechanism is employed by the exploitation of charge modulations originating from electronic super-structures or charge-density waves [13, 120]. Nilius et al. observed self-organization of gold atoms on a polar FeO(111) surface. The oxide is forged by a bilayer of the two components where a surface dipole forms between the Fe cations and O anions. The lattice mismatch between FeO and Pt(111) leads to a Moiré pattern with a periodicity of 25 Å. The Moiré cell is divided into three domains, where Fe atoms alternately occupy on-top, fcc and hcp positions on the Pt(111) surface and have different vertical distances from the O ions, imaging a spatial variation of the surface potential. As a result the vast majority of Au atoms occupy hcp sites. Silly et al. produced a hexagonal super-lattice of Cerium atoms with a spacing of 32 Å on a Ag(111) surface when the substrate was cooled down to 3.9K. The order hereby originates from Ag(111) surface waves.

The examples listed above show that the agent for the self-organization can either be a property of the plain substrate, a property that is created within the substrate prior to deposition or it could be an adsorbate-induced reconfiguration. It needs to be distinguished for each case whether it is a kinetically or thermodynamically driven process. Some of the systems above indicate a strong interaction between the under-

¹For the latter case they found that the second monolayer of Ag forms a trigonal network of dislocations in which the compressive strain is partially relieved. The dislocations mark the transitions from a fcc to a hcp stacking.

laying metal and the deposit. This is not always desirable. Template surfaces that are chemically inert are of special interest, in particular because the intrinsic properties of the functional units on top of it can be preserved. Oxide films conform to these demands and due to their band gap, minimize the adsorbate-support interactions. Hence, considerable efforts have been made to fabricate patterned oxide surfaces [121, 122].

The approach taken within the research presented here was to focus on an inert support and modulate the surface properties prior to any metal deposition. This was achieved by growing the ultra-thin aluminum oxide film that is commonly prepared on NiAl(110) onto a stepped NiAl{16141} surface [123]. The alumina film on regular NiAl(110) is a well investigated and understood metal-oxide system. A detailed picture of its stoichiometry, atomic configuration and electronic properties has evolved from extended experimental and theoretical investigations [5, 15, 124]. A characteristic of special interest is the well-defined defect structure of the film which is expressed in a network of dislocation lines. These surface defects are responsible for various chemical and physical properties of the oxide. In particular a variation regarding the adsorption and nucleation of several metals² (Fig. 4.1) [15] and the dissociation of molecules [125] have been observed. By growing the alumina film on a vicinal NiAl surface, the initial conditions are changed. Ideally, the intrinsic dislocation lines might be adjusting to a regular step pattern, leading to a controlled modification of the defect structure.

Manipulating the defect structure of an oxide surface is of scientific and technological relevance, because it opens a way to fabricate arrays of suited nucleation sites for the growth of metal particle or nano-wires, which can be used as model systems for catalytic and magnetic investigations. Also intrinsic oxide properties might be controlled by changing the abundance of one specific defect type, e.g. of optically-active color or paramagnetic spin centers [121, 126].

4.2 The Growth of Aluminum Oxide on a Regular NiAl (110) Surface

4.2.1 The Oxide Structure

The understanding of the structure of the alumina film on NiAl(110) has undergone quite an evolution and is an excellent example for the complementarity of the multitude of surface science methods and theoretical model-calculations.

The crystals are cut from a rod and mechanically polished. Laue diffraction is used to verify the surface orientation. Once introduced to the ultrahigh vacuum environment, the surface is repeatedly sputtered with Ar⁺ ions and subsequently annealed to about 1300 K to heal the crystal. These cycles are continued until an atomically flat corrugation is achieved, resulting in terrace widths of up to several 100 nm. STM and

²Rhodium, Palladium, Cobalt, Platinum and Vanadium

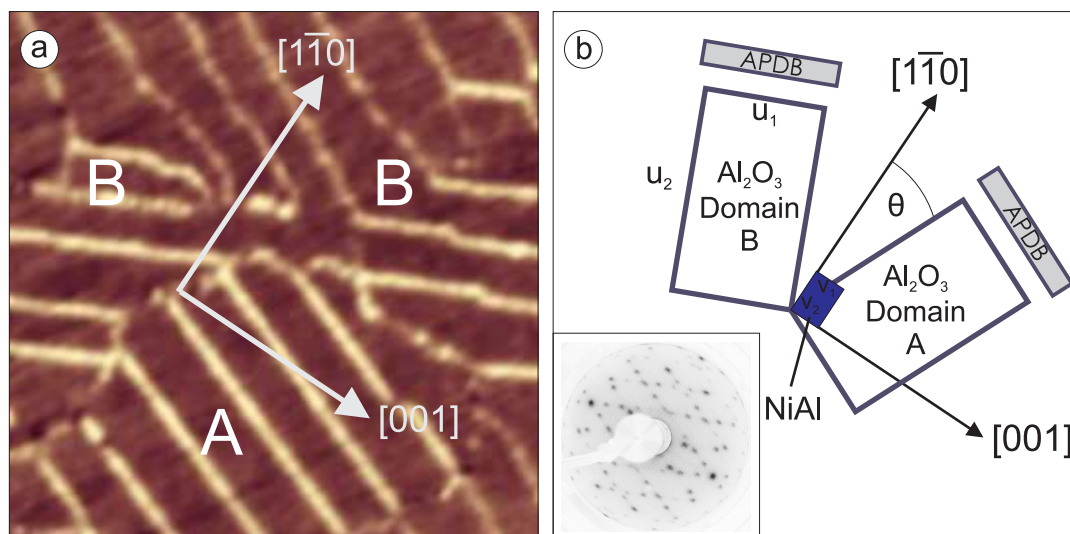


Figure 4.2 Topography, LEED and model of alumina grown on NiAl(1 1 0): (a) STM image (90 x 90 nm) promoting the APDB and their orientation with respect to the crystallographic directions of the substrate. (b) Model of the Al_2O_3 unit cells and their appearance in LEED (insert).

LEED are used to inspect the surface quality (Fig. 4.5a).

A method for preparing the aluminum oxide was presented by Jaeger et al. [5]. The clean NiAl(1 1 0) surface is slightly annealed to 550K and exposed to 1200 L oxygen. In the following UHV conditions are reestablished and the sample temperature is raised to 1100 K for 600 s. During the oxide formation the film becomes more compact and covers only $\approx 90\%$ of the substrate. Therefore, a second cycle of oxygen exposure and annealing is performed to achieve full coverage. Once completed the LEED pattern displays a unique signature that is characteristic for the oxide film (Fig. 4.2b, insert).

From the LEED pattern the Freund group was able to derive several significant features [5]. Immediately obvious is the fairly large unit cell which was found to be $u_1 = 10.55 \text{ \AA}$ and $u_2 = 17.89 \text{ \AA}$ compared with the NiAl unit cell of $v_1 = 2.89$ and $v_2 = 4.08 \text{ \AA}$ (Fig. 3.15a). The oxide is growing in two reflection domains (referred to as A and B) that are tilted by $\pm 24^\circ$ with respect to the $[1 \bar{1} 0]$ direction of the support. The film growth is commensurable along the $[1 \bar{1} 0]$ direction but incommensurable along the $[001]$ direction.

A combination of ion-scattering spectroscopy (ISS) and X-ray photo-electron spectroscopy (XPS) was able to prove the absence of Nickel within the oxide film. The incorporation of the Aluminum ions was investigated with electron energy-loss spectroscopy (EELS) and indicated that the cations are residing in tetrahedral as well as octahedral sites. The thickness of the oxide layer was concluded to be approxi-

mately 5Å, based on the damping of the Ni Auger³ intensity and the dimming of the substrate's LEED spots. The result indicated the presence of two oxide layers.

STM data displays large terraces fully covered with oxide that exhibits a distinctive feature in form of line patterns (Fig. 4.2). These lines are assigned to a dislocation network that is incorporated into the oxide to reduce the strain building up along the commensurate growth direction⁴. Two types of defect orientations can be discriminated for each domain: the straight lines adjusts to the shorter vector of the respective unit cells, the other zig-zag kind crosses the oxide unit-cells in a diagonal fashion.

While the aluminum oxide was well understood down to the nanometer scale, a clear understanding of its atomic configuration was missing until recently. The breakthrough came through STM, STS and conductance mapping (CM) experiments by Kulawik et al. [127] and through DFT model calculations by Kresse et al. [124]. A set of STM images was acquired that was able to produce three out of four layers of the oxide film and of the APDB, giving direct insight into the atomic arrangements in each of them. Shortly after, a model based on density functional calculations, using the plane wave code VASP and the PW91 gradient corrected functional was presented. Both, images and theoretical model were in full agreement with each other. Hence, the oxide is build up by an succession of two aluminum - oxygen layers and accordingly oxygen terminated. The amount of anions and cations varies for each layer, resulting in a stoichiometry of Al₁₆O₂₄Al₂₄O₂₈ alias Al₁₀O₁₃. The first layer of aluminum atoms is arranged in pentagon pairs and heptagons with a preference for binding to the Ni interface atoms, which leads to the commensurate growth along the [1 $\bar{1}$ 0] direction where Ni and Al rows alternate. Given the outer shell configuration of Al 3s²p¹, the aluminum might bind to the Ni via the p_z orbitals, leaving the 2s electrons to anchor the oxide film. The following oxygen layer shows a quasi hexagonal structure, that is in fact identical of the atomic arrangement of the first aluminum layer. The second Al layer has one half of the ions arranged in a pyramidal, the other half in a tetrahedral coordination. This configuration leads to a rather unexpected arrangement of the surface oxygen ions. While the typical constitution of bulk alumina would indicate a hexagonal arrangement, in the thin film the ions are positioned in triangles and squares. The band gap of the film amounts to 6.4 eV for areas away from defects.

4.2.2 Typical Defects in the Oxide

The main structural defects in the film are reflection boundaries between the A and B domains of the oxide and antiphase domain boundaries (APDB) which appear within identical regions. While the borders between reflection domains seem to occur randomly, the APDB form a distinct pattern which can easily be seen in STM (Fig. 4.2b).

³Auger electron spectroscopy (AES)

⁴Sideways the extension of these defect states is delimited by the respective reflection domain borders.

A total of four orientations is distinguishable, each with a specific alignment with respect to the alumina unit cells. Two of them line up parallel to the shorter unit cell vector (Fig. 4.2a) and are referred to as straight APDB, while the other two⁵ cross diagonally [127]. These dislocation lines form as a result of the commensurate growth of the oxide film along the $[1\bar{1}0]$ direction and the consequent strain $\Delta L/L$ that builds up. The growth along the $[001]$ direction on the other hand is incommensurate which by nature prevents the formation of strain.

The straight type of APDB are of particular relevance for the following experiments since their orientations are the determining factor for selecting the plane index of the vicinal surface. This type of dislocation lines is incorporated fairly regularly every 8-10 nm into the oxide film. The formation of this structural element occurs by a split in the middle of the oxide unit cell leading to an elongation of 3 Å and providing room for an additional row of atoms. This has a profound impact on the stress in the film, the stoichiometry and with it the electronic structure. The larger oxide unit cell leads to a different alignment with the underlying NiAl substrate. The domain boundary cell bridges one more Ni row of the substrate than the unperturbed cell. Regarding the $[1\bar{1}0]$ direction, the difference amounts to 2.7 Å. Compared to the 4.1 Å long unit cell of the substrate, the difference of $4.1\text{ Å} - 2.7\text{ Å} = 1.4\text{ Å}$ provides room for the oxide film to relax the compressive strain.

The stoichiometry of the straight APDB was determined through investigations similar to the ones carried out for the undisturbed oxide by Kulawik [127] and Schmid [128]. The row insertion was described in a layer by layer fashion, revealing a composition of $\text{Al}_{19}\text{O}_{28}\text{Al}_{28}\text{O}_{32}$ with an aluminum oxygen ratio equivalent to 4:5, substantiating an oxygen deficiency compared to the unperturbed alumina. Due to the oxidation state of the $\text{Al}_{\text{interface}}$ (+2) and $\text{Al}_{\text{surface}}$ ions (+3), the film is not auto-compensated and lacks one O atom per boundary unit-cell. This absence would be expected to result in two electrons occupying electronic defect states with Al 3p character near the conduction band edge. Instead, the electrons are transferred to the NiAl support and the defect states remain unoccupied.

These findings are well reproduced by the scanning probe data, where the ADPB displays a strong dependence on the bias voltage. At energies between +2.5 eV and +3.5 eV and above +4.5 eV, the defect rows appear as bright protrusions. In comparison with STM where the current results from the integration over an energy interval (0 eV to 'bias' eV), scanning spectroscopy imaging is probing the local differences in conductance at a given energy and therefore extracts the local variation in the density of states at that energy. The conduction maps clearly show an increase in LDOS at 2.5 eV and 4.5 eV, based on tunneling into unoccupied states⁶. Additional information gained by scanning tunneling spectroscopy indicated two states at +2.6 eV and +3.0 eV. The state at 4.5 eV seen in topographic imaging could not be discriminated due

⁵Zigzagged.

⁶A detailed description of the bias dependence can be found in [129].

to the increasing conductance of the conduction band. Model calculations performed by Schmid [128] indicate a total of three unoccupied states, located at energies of 2.3 eV, 2.9 eV and 3.9 eV, seemingly slightly shifted compared to the experimental data. As a consequence of the electron donation from the Al ions into the NiAl substrate, a local band bending occurs that shifts the CB edge to lower energies and with it the oxide states into the conduction band. The highest state, though, is in any case well above E_C .

4.3 The Formation of Aluminum Oxide on a NiAl (16 14 1) Vicinal Surface

4.3.1 Introducing the NiAl (16 14 1) Vicinal Surface

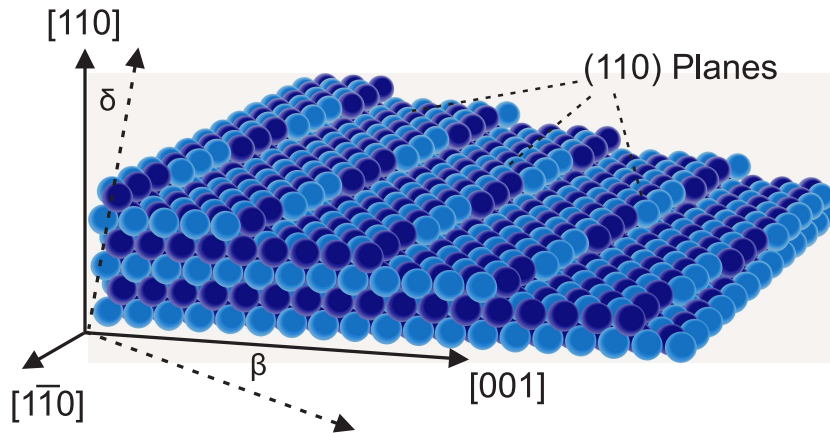


Figure 4.3 Model of the NiAl(16 14 1) vicinal surface, consisting of narrow terraces with (110) orientation, separated by mono-atomic steps.

Vicinal surfaces can be created by cutting of a single crystal along a plane in proximity to a main crystallographic direction. Considering the cutting angle does not deviate too much from the low index plane the procedure results in a periodic succession of steps⁷ while the orientation of the small sections in between is preserved. In this respect the nomenclature is phenomenologic since only the long range orientation follows the cutting plane.

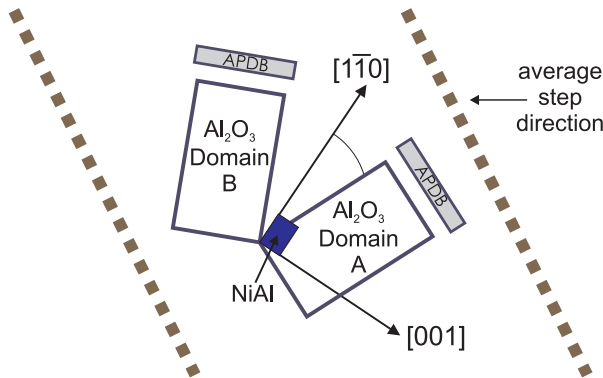


Figure 4.4 Schematic representation of the step orientation with respect to the oxide domains of the original film. The shorter side of the unit cell of type A is almost parallel to the step direction.

The NiAl(16 14 1) surface is featured as the new template for alumina growth. Its orientation was created by cutting a NiAl crystal by 4.7° degrees along the $[1\bar{1}1]$ direction. The resulting plane is a vicinal to (110). Figure 4.3 depicts a model of the (16 14 1) surface in relation to the relevant crystallographic directions. The trimming is supposed to result in an array of mono-atomic steps running at an angle of 34° with

⁷Usually mono-atomic

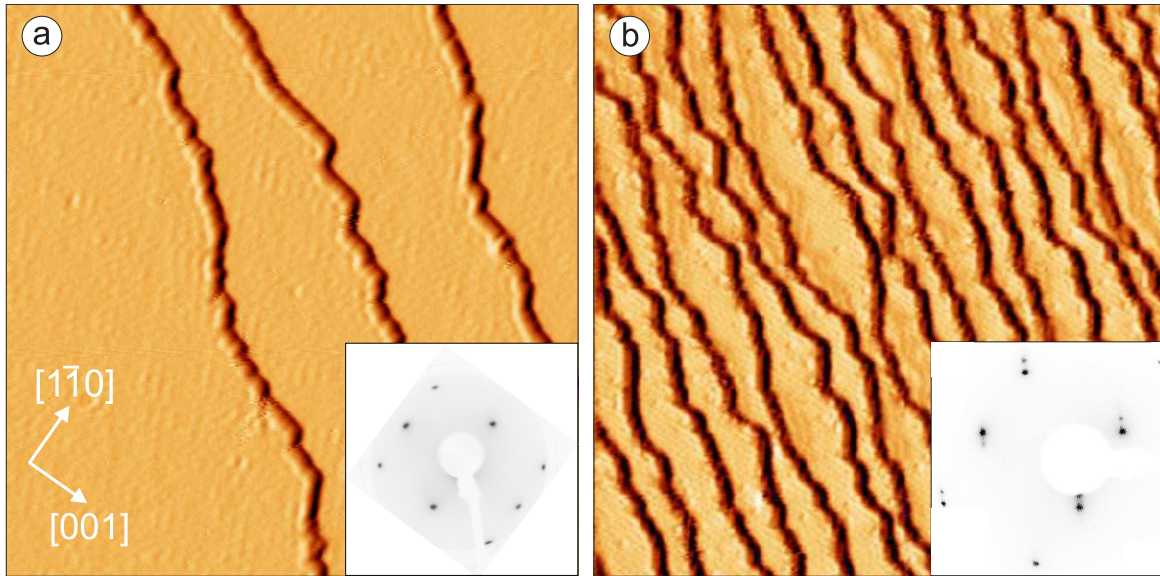


Figure 4.5 Comparison of topography and LEED between the NiAl(110) and the NiAl(16 14 1) surfaces. The LEED images are aligned to the crystallographic directions of the STM images: (a) NiAl(1 1 0), $40 \times 40 \text{ nm}^2$, $U_B = 0.32 \text{ V}$, $I_T = 0.5 \text{ nA}$. (b) NiAl(16 14 1), $40 \times 40 \text{ nm}^2$, $U_B = 0.85 \text{ V}$, $I_T = 0.6 \text{ nA}$. The LEED spots split due to the proximity of the steps

respect to the $[001]$ direction. As illustrated in Fig. 4.4, the (16 14 1) plane was chosen because of the step alignment with respect to the oxide domain orientation, considering the oxide growth on the (1 1 0) surface. Theoretically, the steps line up with the APDB of domain A, which leads to different growth condition for both domains.

Like before, the crystal was cut from a rod and mechanically polished. Next, the sample was transferred into the ultrahigh vacuum environment, repeatedly sputtered with Ar^+ ions and subsequently annealed for flattening the crystal. A lower surface roughening temperature in accordance with the higher mobility limits the annealing temperature to about 1100 K.

The changeover from the original to the vicinal surface is illustrate by the STM images in Fig. 4.5 a and b. The modified surface exhibits the expected succession of (1 1 0) terraces with an average width of $2.5 \pm 0.5 \text{ nm}$. This is confirmed by LEED measurements, which exhibit the NiAl unit cell and a distinct splitting of the fundamental spots compatible with the presence of a regular step pattern with about 2.5 nm periodicity (Fig. 4.5b, insert). In the STM image the step edges appear with ragged shape. Only the mean step orientation follows the angle of 34° with respect to NiAl $[001]$ as expected from the miscut angle. The ruggedness is resulting from an alteration of short step sections running along $[001]$ and $[111]$ direction. Apparently, these directions mark the low-energy step orientations on the (1 1 0) surface and

therefore develop at thermodynamic equilibrium conditions.

4.3.2 An Oxide Induced Surface Reconstruction

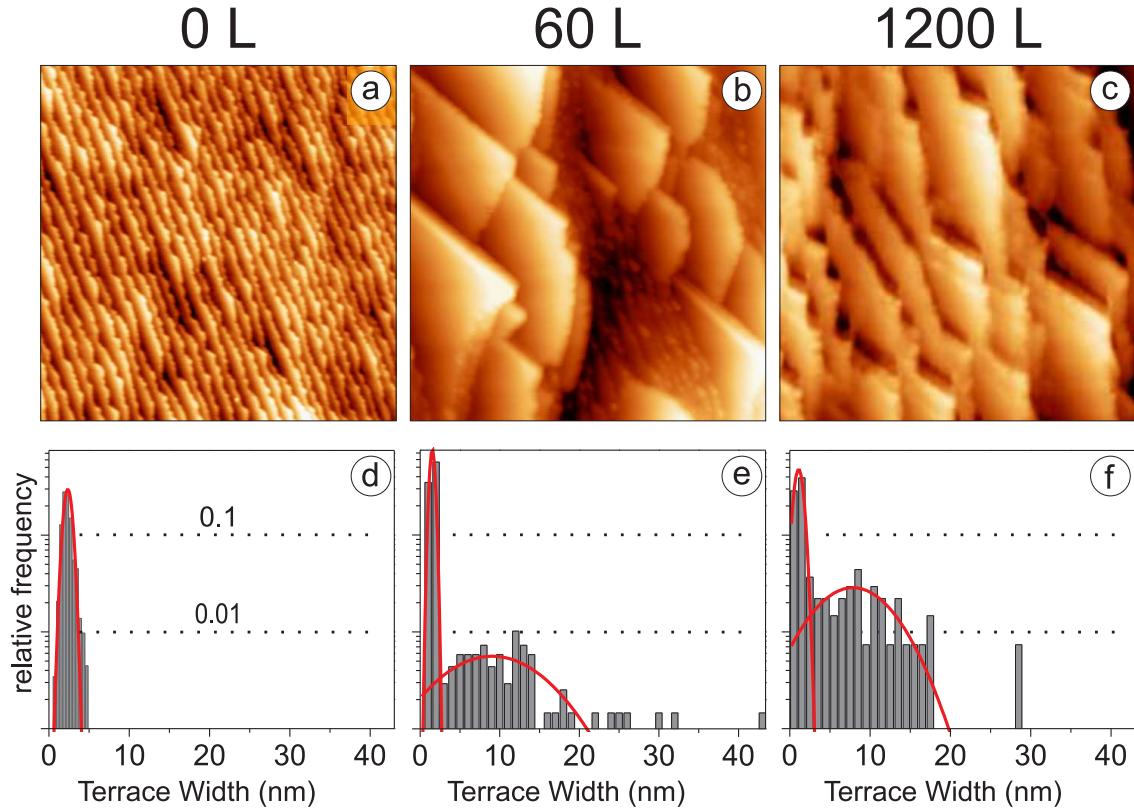


Figure 4.6 Morphological alteration of the NiAl vicinal surface by exposure to oxygen: the pristine surface (a, d), after exposure to 60 L O₂ (b, e) and after exposure to 1200L O₂ (c, f). Upper row: STM images, measured at 80 K (a) 100 x 100 nm² and (b-c) 200 x 200 nm². The tunneling parameters are $U_B = 4.5$ V and $I_T = 0.1$ nA. Lower row: step width distribution, each referring to the STM image above.

The amount of oxygen needed for the film formation on the vicinal NiAl surface was initially unknown and accordingly, the O₂ exposure was varied during the experiments⁸. The results for two dosages, one leading to a partial film formation, the other one resulting in a fully oxidized surface, shall be discussed here.

The initial preparation was done by dosing 60 L O₂ onto the NiAl(16 14 1) at a sample temperature 550 K followed by annealing to 1000 K. Already this small amount

⁸The O₂ background pressure was held constant at 1×10^{-6} mbar during all experiments and the exposure time varied instead.

leads to a profound change in the surface morphology (Fig. 4.6b). The succession of almost equidistant (1 1 0) terraces vanishes at the expense of a new pattern that consists of very large (1 1 0) planes in alternation with small-sized areas. Characteristic for the large terraces is a triangular shape that is formed by long, straight sides along the [0 0 1] directions and rather rugged boundaries with alternating [0 0 1] and [1 1 1] sections. This is indicating an energetically favorable oxide formation along the [0 0 1] direction up to the point when the surface tension by maintaining the misdirection exceeds the gain. Large (1 1 0) planes are often delimited by step bunches containing ten and more single steps, a feature that was not observed on any of the clean NiAl surfaces. The resulting terrace width distribution is depicted in Fig. 4.6e. It exhibits two maxima, which can be fitted by Gaussians, one with a peak at 1.5 nm ($\sigma = 0.2$ nm), representing the narrow terraces, and a second one with a peak at 9.8 nm ($\sigma = 8.1$ nm) representing the broader terraces. The large standard deviation of the latter reflects the significant difference in size, as displayed in the STM data⁹.

In well-resolved STM images, metallic surface regions are clearly distinguished from areas covered by alumina patches due to the characteristic line pattern of the alumina lattice (Fig. 4.7a and c). At 60 L O₂ exposure, the oxidized fraction of the surface is approximately 20%. Even in the case of small oxide patches, the alumina shows the known crystalline structure with no indication for the presence of alternative, potentially disordered phases. The oxide islands exclusively nucleate at the upper sides of step edges. They are found in various constitution, either as patches which cover entire terraces or as small fractions near the edges, next to vast NiAl regions (Fig. 4.7b and c). Along the edges though, an additional feature can be found. Sporadically, extended oxide stripes of 2 nm width and 0.2 nm height appear that strictly follow the NiAl[0 0 1] direction and border the triangular (1 1 0) planes (see arrows in Fig. 4.7a).

Augmenting the O₂ exposure increases the oxide coverage until a complete surface oxidation is achieved at around 500 L (Fig. 4.6c). At this point the structure is dominated by large (1 1 0) terraces that are more uniform in size and shape than for the case of partial oxidation. While some of the triangular shaped boundaries are still present the overall alignment has changed, being in average closer to the original orientation of the pristine metal steps (Fig. 4.6a and c). Correspondingly, terraces with less than 2 nm width cover a much smaller fraction of the surface. The terrace width-distribution therefore retains the bimodal character, although the peak positions have shifted to 1.1 nm ($\sigma = 0.3$ nm) and 7.9 nm ($\sigma = 5.0$ nm) for narrow and wide terraces, respectively (Fig. 4.6f). Height profiles across a fully-oxidized (16 14 1) surface indicate the presence of step bunches, containing approximately 10 single steps, while mono-atomic steps have obviously disappeared.

Remarkably, even for a complete oxidation, the dislocation lines between neighboring oxide domains are rarely observed, although they dominate the STM images of the alumina film on flat NiAl(1 1 0) (Fig. 4.6f and Fig. 4.8b). Instead, the domains are

⁹The contribution of Patrick Helmecke in analyzing the STM data is greatly appreciated.

almost entirely delimited by steps. The electronic structure has changed in a similar way. The defect states described in 4.2.2 were the outstanding attribute of flat films within the STM/STS data. Now, the flat oxide regions remain plain and featureless for energies that are within the bandgap.

4.3.3 Oxide Nucleation and Growth

The remarkable changes of the morphology during the oxidation for both the partially and the fully oxidized NiAl(16 14 1) surface prompted an exploration of the oxide nucleation process. The STM images in Fig. 4.7 were acquired at small oxygen exposures and illustrate the different regions that form during oxidation. From a detailed analysis of the STM data, the upper sides of the step edges were identified as the thermodynamically favored nucleation site of the oxide. This type of nucleation was previously observed by Eierdal et al. for the Ni(1 1 0) surface at room temperatures and oxygen exposures of $\geq 0.1L$ [130] and by Hildebrandt et al. for the Ni(1 1 1) surface at slightly elevated temperatures and oxygen amounts between 10L and 150L [131].

There are several arguments that need to be considered for the initialization of the oxidation process on-top of a step edge:

(i) Atoms at step positions have a lower coordination than those incorporated into terraces and are usually more reactive.

(ii) The aluminum oxide is Ni free (see Cha. 4.2.1). Thus, during the oxidation of NiAl, Ni atoms have to be removed from the reaction site. On flat crystals this occurs via diffusion into the bulk. On step edges, the energy-expensive sub-surface diffusion of Ni might be replaced by the less-activated surface diffusion, favoring the initial oxidation of steps.

(iii) The electron distribution across steps derives from the bulk, as it does not follow the abrupt change of the atom positions. Instead, the transition is rather smooth which leads to a reduced electron-density at the upper side of the step edge, while charge accumulates at the bottom, resulting in a small dipole¹⁰. The oxide formation involves charge donation from the interfacial Al atoms toward the NiAl support [124] which anchors the film. Therefore, the oxide nuclei behave like nucleophilic molecules that preferentially bind to the topside of a step edge as well [132].

Once an oxide nucleus has formed at the top of an edge the step is pinned, since the oxide particle inhibits the participation of this region in the diffusive material transport across the terraces that takes place at elevated temperatures. During the annealing the mobile atoms on the surface are inclined to reduce the energetically expensive deviation of the vicinal surface from the low index plane. The mass transport follows the mis-cut direction of the crystal, causing a backward motion of steps along the $[1 \bar{1} 1]$ direction and an overall decrease of the surface inclination. As pinned steps are unable to take part in this movement, the adjacent terraces develop into large,

¹⁰Known as the Smucholowski effect

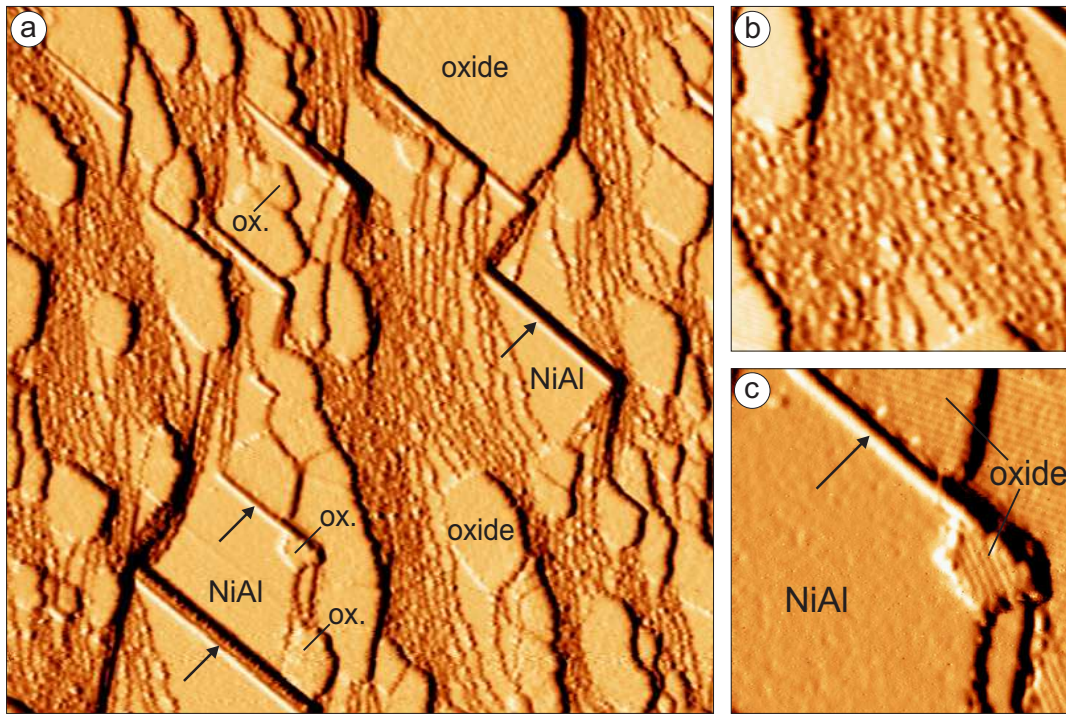


Figure 4.7 Nucleation of alumina on a NiAl(16 14 1) vicinal surface after dosage of 60 L O₂ (a) Overview, 200 x 200 nm². (b) and (c) close-up images, 45 x 45 nm². U_B = 4.0 V, I_T = 0.1 nA .

triangular (1 1 0) planes, as observed on partly oxidized surfaces.

In addition to the oxide agglomerates described above, another surface feature seems to be important for the nucleation. Extended stripes that form exclusively along the [0 0 1] direction (see arrows in Fig. 4.7a) cause the development of triangular-shaped surface planes. The composition of these one-dimensional features could not be deduced from the STM data, however, their exclusive emergence after oxygen treatment suggests a distinct oxide phase that preferentially grows along this direction¹¹. An oxide nature of these stripes would be compatible with their role as pinning lines for the triangular (1 1 0) planes. Oxide nano-rods of similar shape have previously been observed by Pierce et al. in LEEM studies performed during the initial oxidation of flat NiAl(1 1 0) surfaces [133]. In that case, the one-dimensional growth has been traced back to an asymmetry in the lattice strain of this oxide phase (NiAl₂O₄ as proposed by the authors), which favors elongation of the rod along the direction of smallest mismatch with the NiAl lattice, that is the [0 0 1] direction.

¹¹It should be considered though, that the crystal lattice along the [0 0 1] is equivalent for the horizontal (terrace) plane and the vertical (step) plane. Hence, the initial growth conditions are similar until the further extension of the step height becomes energetically unfavorable.

With increasing oxygen exposure, the number of oxide nuclei at the surface increases and pinning centers homogeneously arrange along the step edges (Fig. 4.7b). At this point the mean step direction according to the mis-cut angle is almost not discernible anymore and the interplay between the step pinning and the realignment with the original orientation lets the edges appear curved. The higher density of nucleation centers suppresses the development of extremely large (110) planes and leads to a smaller terrace width distribution on the fully oxidized surface. The average terrace size has enlarged by a factor of 4-5 with respect to clean NiAl(16141), which is accompanied with the agglomeration of mono-atomic steps into step bunches.

Apparently, the expense to overcome step-step repulsion during bunching is compensated by the energy gain when growing large, step-free oxide patches. The mean terrace width of 8 nm on completely oxidized surfaces agrees surprisingly well with the typical distance between APDB on flat NiAl(110) [127]. As APDB are usually introduced into the oxide lattice to release the mismatch-induced strain, one might argue that this relaxation mechanism is replaced by the insertion of step edges on the vicinal surface. This mechanism would render the energy-expensive formation of domain boundaries unnecessary, thus explaining their absence in STM images taken for fully-oxidized NiAl(16141). The mean terrace width on the vicinal surface now arises as the result of the energy balance between enlarging an oxide patch without step edge and stabilizing a single domain against the mismatch-induced lattice strain. From the fact that the observed terrace width nearly matches the APDB-distance on flat NiAl(110) follows that mainly the strain contributes to the final step arrangement and step-step repulsion plays only a minor role.

4.3.4 Controlled Alteration of the Alumina Domain Distribution

The NiAl(110) crystal exhibits a C_{2v} symmetry which leads to the formation of two oxide reflection domains A and B that are occurring with equal probability. On the vicinal surface, the mean step direction forms an angle of 34° with the [001] direction. While the original symmetry is still present on the terraces of the vicinal surface, the insertion of steps creates unequal conditions for the oxide formation regarding the two domains. The step edges roughly align with the short unit cell vector of type A domains which is similar to the path of the corresponding straight APDB (Fig. 4.2). For the B domains on the other hand, short unit cell vector and APDB are tilted by almost 60° against the step orientation. Considering that the step configuration on the vicinal surface replaces the strain release via APDB, this mechanism works significantly different for the two domains.

Figure 4.8d shows the LEED image of the fully oxidized NiAl (16141). The difference to the LEED of the oxide film on NiAl(110) (Fig. 4.8c) is quite obvious. In case of the plain substrate, the reflection spots form a peculiar diamond-shaped pat-

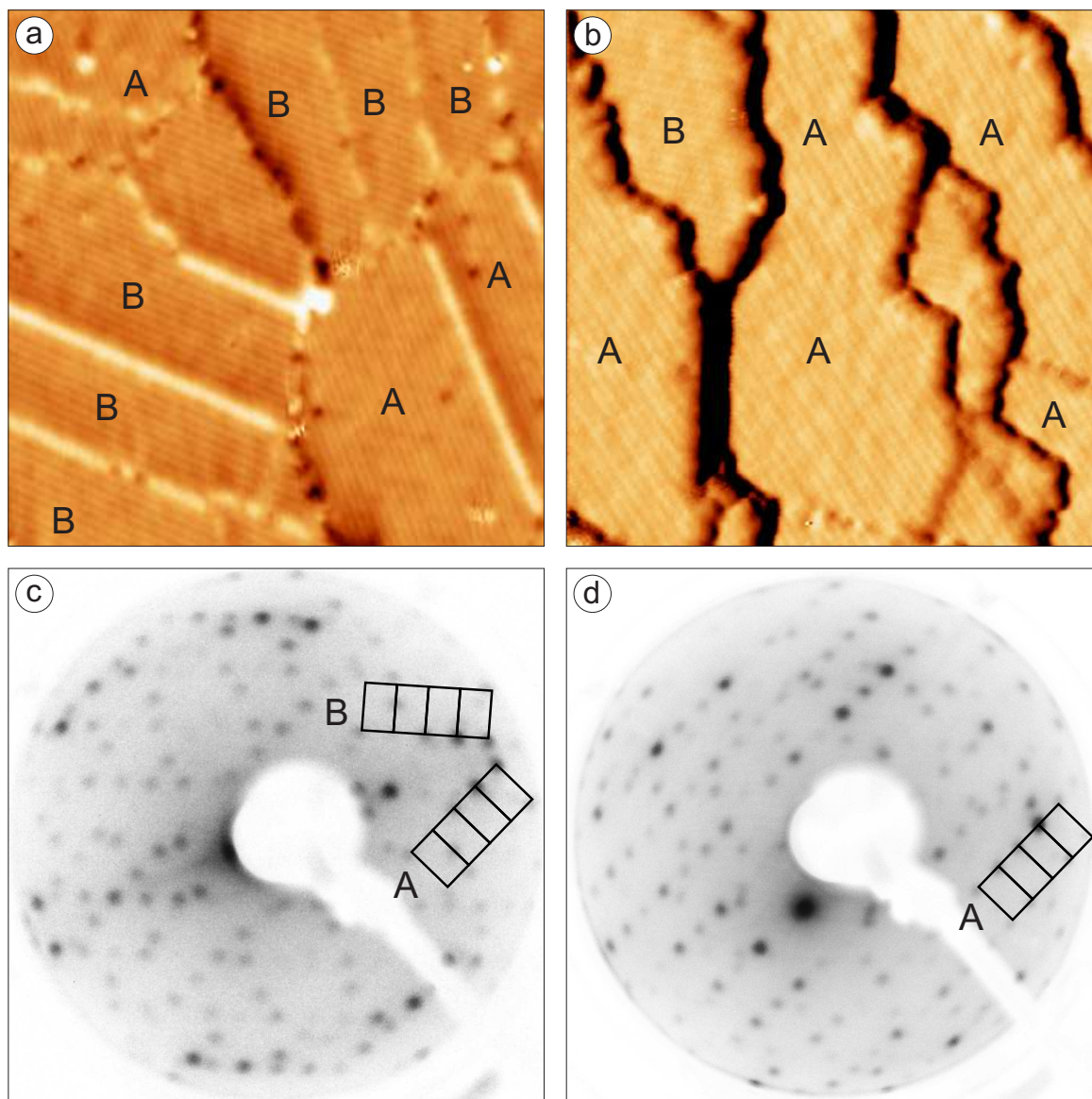


Figure 4.8 STM topographic images after oxidation with 1200 L O₂ and the corresponding LEED: (a) NiAl(1 1 0), 80 x 80 nm². (b) NiAl(16 14 1), 50 x 50 nm². (c) LEED of the sample (a) with indication of both oxide domains. (d) LEED of the sample (b) with one dominating reflection domain (A).

tern. It originates from two sets of rectangular arranged spots that form an angle of 48° , indicating the mis-orientation of the domains¹². Similar intensities for both set of spots indicate an equal occurrence of both domains on the surface [14]. In the case of the NiAl(16 14 1) substrate, the LEED image is dominated by the rectangular arranged spots of a single domain. Reflexes that belong to its counterpart are strongly suppressed, suggesting the preferential growth of one domain type on the vicinal surface. Inherent to the method, LEED data averages over larger areas and by moving the electron beam several mm across the sample surface it was verified that the findings are not just a local discrepancy. On this basis the utilization of STM for statistical purposes seems justified.

The STM measurements of fully oxidized NiAl(16 14 1) corroborate the results of the LEED study. Due to the absence of dislocation lines, the individual oxide domains are identified by a characteristic line pattern that follows the direction of the short unit-cell vector. Both orientations can easily be distinguished. The type A domain, which is the one where APDB align with the step orientation, is preferentially observed on the surface (Fig. 4.8b). From a statistical evaluation of STM images taken from different surface areas and preparation cycles follows that the fraction of the surface covered with domain A amounts to approximately 80% while the type B domains provide only 20% of the oxide film.

This obvious change in the domain distribution with a clear preference for type A supports our considerations that the step pattern influences the probability to form either domain A or B. The projection of the two oxide unit cells onto the step pattern provides an insight into the potential mechanism (Fig. 4.4). An array of 5 oxide unit cells with A orientation bridges a length of 89.5 \AA , a number very close to the typical APDB distance as well as to the average terrace width for the oxidized vicinal surface. At that distance, the accumulated strain due to the lattice mismatch along NiAl $[1 \bar{1} 0]$ needs to be released, which is accomplished by creation of the following step edge. In contrast, the other domain would have to form arrays of almost 10 unit cells to grow across the same terrace, by reason of the different orientation. For the A domain on NiAl(16 14 1), the dislocation lines can be substituted by step edges of regular orientation. Such relaxation mechanism is, however, ineffective for domain B, first because of the larger number of unit cells that are necessary to bridge a typical terrace, and second because of the mean step direction on the (16 14 1) surface not being compatible with the orientation of a type-B APDB. Consequently, B domains accumulate more strain when overgrowing the (1 1 0) planes of the vicinal NiAl surface, rendering their development thermodynamically less favorable. It is, in fact, likely that the sole reason for any occurrence of the B domain is the energetically expensive step derivation from the $[0 0 1]$ direction, which locally works against the step orientation resulting from the vicinal surface (Fig. 4.4).

The alignment of the oxide cells with the steps at the point of nucleation seems to

¹²The unit cell of the NiAl, which is much larger, is not indicated in the images.

be of no impact for the preferential growth of one domain. Even though one of the main crystallographic direction of A domains follows the initial step orientation on NiAl(16 14 1) and the unit cells being almost perfectly rectangular [128], both domains occur in similar quantities in the case of partial oxidation. Hence, the kinetics during growth are not further discussed here. The transition toward a single-domain oxide is thermodynamically driven by the elevated temperatures during the final sample annealing to attain the lowest surface free energy.

4.4 Conclusions

The preparation of thin alumina films on vicinal NiAl(16 14 1) is accompanied by strong modifications of the initial surface morphology. The sequence of adjacent (1 1 0) terraces transforms into larger planes separated by step bunches. The new terrace width corresponds to the characteristic spacing of straight dislocation lines in the alumina film on flat NiAl(1 1 0), which identifies mismatch-induced lattice strain in the oxide layer as the most prominent factor for the structural modifications. In addition, the new oxide film is almost defect free across the terraces, hence both the straight and zigzagged-type APDB become irrelevant for strain reduction. The periodic step pattern on the (16 14 1) surface favors the development of one reflection domain. Based on the geometry, a stress release via step edges becomes particularly efficient in this case.

Even though the impact of the stepped substrate on the oxide growth is profound, the desired result of a well ordered, patterned template was not achieved yet. The step edges on the vicinal alumina surface have a rather jagged and uneven character, which limits their utilization as template for the fabrication of ordered particle or nano-wire arrays. On the other hand, the homogeneous, basically defect free planes and a large band gap make the oxide film a perfect candidate for stabilization of well decoupled adsorbates.

Eventually, vicinal surfaces with slight variations compared to the present one need to be created and investigated. There is potential to fine-tune the underlying substrate in a way that it becomes ideal for forming evenly patterned surfaces. The consequent continuation of the project would be an exploration of the adsorption behavior, in particular for metal atoms, such as Rh and Pd. Further attention needs to be given to the one dimensional oxide. Because of the strong tendency to orient along the [001] direction, a crystal cut leading to steps along this orientation would be desirable. It is likely that the exposure to low amounts of oxygen then leads to arrays of short metallic terraces set apart by completely oxidized step edges. As a consequence, the preferential adsorption of deposits on the metal regions might result in the formation of perfect nano-wires.

5 A Size-Selective Adsorption Mechanism: Metal Atoms on SiO₂ Thin Films

5.1 Introduction

The adsorption properties of solid surfaces are to a large extent a function of the physical and chemical nature of the topmost atomic layer(s), while recessed sub-surface layers contribute very little. Generally this adsorption behavior is rather unspecific regarding the admission for exclusive molecular species to bind at specific surface sites. To the contrary, a high degree of selectivity is common to all biological systems, where certain species are repelled from the inert surface of a membrane and are permitted to interact or pass through only at distinct pores and channels.

A similar though less complex concept finds its application in material science. Two classes of materials that are used extensively as heterogeneous catalysts are microporous and mesoporous inorganic solids whose structures are dominated by distinct openings [134].

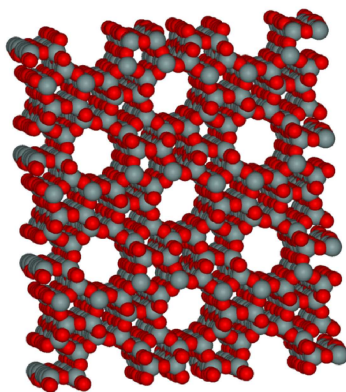


Figure 5.1 Model of a porous Zeolite surface.

According to the definition accepted by the International Union of Pure and Applied Chemistry, porous materials can be grouped into three classes based on their pore diameter (d): microporous when $d < 2.0$ nm, mesoporous for d ranging between 2.0 nm and 50 nm and macroporous if $d > 50$ nm [135]. The utility of these materials is rooted in their selective permeability which allow molecules to access large internal surfaces and cavities that enhance catalytic activity and adsorptive capacity [136–138].

A major subclass of the microporous materials is represented by the molecular sieves. These materials are exemplified by the large family of aluminosilicates known as zeolites, in which the uniformly-sized micropores of a $-\text{Si}-\text{Al}-\text{O}-$ network control whether or not a reactant can penetrate the opening and propagate

to the reaction site (Fig. 5.1) [138, 139]. The pores can accommodate single ions, molecules or atomic clusters that might participate in chemical reactions within the 3-dimensional matrix. The efficiency of such process depends strongly on the character of the reactant as it has to match the physical size of the pores or needs to be inert regarding potential bonds with ions inside the channels.

Recently, a two-dimensional analogon to the three-dimensional porous materials was developed [140, 141]. The new material consists of an ultra-thin silicon-dioxide film that is synthesized on a Mo(112) surface [142–144]. In correspondence with the 3-dim. silicates the building blocks of the film are Si-O tetrahedrons which form rings on the surface enclosing holes of 3-4 Å diameter. These openings provide access to small areas of the Mo-silica interface, which provide an attractive binding environment for metal atoms and small molecules [145, 146]. The oxide surface itself is chemically inert due to a high degree of bond saturation within the thin silica layer [147]. Therefore the adsorption attributes of the silica-molybdenum complex are dependent on the activity at the nano-pores and whether or not an adsorbate could permeate the oxide layer and reach a strong binding site at the interface. In the following, proof for this functionalization principle, which is unique to this oxide film, is presented.

The composition of the silica film itself has been debated in length, as initially two contradicting models were proposed [148]. While both descriptions were based on film formation from SiO₄ units, one model promoted an isolated-cluster arrangement and the other a two-dimensional corner-sharing network. In the end, the cluster-model was dismissed in favor of the 2-dim. network model [149, 150] which is fully supported by DFT calculations [151, 152].

5.2 Synthesis of Silicon Oxide on Mo(112)

5.2.1 Sample Preparation

The procedure for synthesizing atomically flat silica films has seen an evolution and refinement over time. Originally, Mo crystals with {100} orientation served as templates for the film growth [7, 153]. The substrate was held at room temperature during Si evaporation and annealed to 1400K after the deposition was completed. The Si evaporation itself was performed in the presence of a low-pressure oxygen background¹. After annealing the film would display the electronic and structural properties of vitreous silica.

Schroeder et al. were the first ones to identify Mo (112) to be a better suited template. Mo has bcc crystal structure and the (112) face is organized in close packed atomic rows with inter-atomic spacing: $a_1 = 2.73$ Å along the $[\bar{1}10]$ direction and rows with a spacing of $a_2 = 4.45$ Å in $[\bar{1}\bar{1}1]$ direction, with furrows in between (Fig.

¹The oxidative etching of the source produces SiO, the gas phase precursor for SiO₂.

5.2c). The original recipe for sample preparation² was modified into four cycles of Si deposition at 300K followed by oxidation at 800K in an $5 \cdot 10^{-6}$ mbar O_2 environment. Afterwards, the oxygen pressure was increased to $1 \cdot 10^{-5}$ mbar and the Mo crystal was annealed stepwise until a temperature in the range of 1000K - 1250K was reached. The annealing was terminated once the LEED-spots of the surface exhibited a $c(2 \times 2)$ -Mo(112) structure.

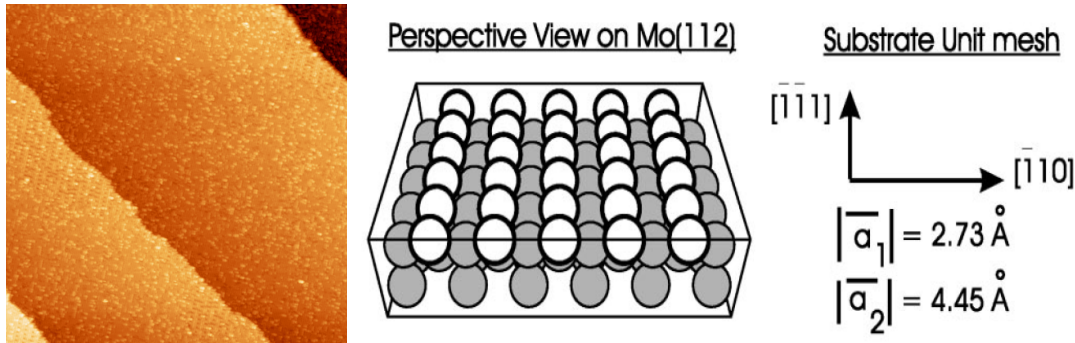


Figure 5.2 Topography and geometry of the pristine Mo(112) surface, left: STM (95×95 nm²; $U_B = +1310$ mV; $I_T = 42$ pA) middle: model of the atomic configuration of the topmost layers; right: corresponding unit cell vectors [140].

Chen et al. have introduced an intermediate step into the procedure by first exposing the pristine Mo (112) surface³ in a heated state (850K) to approximately 30L of O_2 [148], resulting in a $p(2 \times 3)O$ -Mo(112) surface that would be confirmed by LEED. Subsequently, several cycles of deposition were carried out, each cycle consisting of sub-monolayer amounts of Si deposition in UHV, followed by two annealing steps in $1 \cdot 10^{-7}$ mbar O_2 , the first one at 800K for 5 min and the second one at 1200K for an additional 5 min. The preparation was continued until AES indicated a constant Si/Mo ratio.

Within this work, the Mo crystal was initially cleaned by ion milling with Ar^+ ions at energies around 1200 eV. Later on, the sample would be cleaned by cycles of oxidation at 800K in $1 \cdot 10^{-8}$ mbar O_2 and subsequent annealing in UHV to 2100K (Fig. 5.2). The silica film preparation was similar to the procedure applied by Weissenrieder et al. [144]. Compared to the previous methods, this approach further simplifies the film synthesis to three steps: 1. Chemisorption of $2 \cdot 10^{-7}$ mbar O_2 at 850K to create a $p(2 \times 3)O$ -Mo(112) overlayer, 2. Deposition of approx. 1.2 ML Si while keeping the previous sample temperature and oxygen background pressure constant and 3. Annealing to 1250K in UHV for 180 s. The annealing step appeared to be crucial for

²Published by the Goodman group.

³It should be mentioned that the Mo(112) surface is very reactive and it is rather difficult to keep it clean for an extended period, hence, it was not until 2006 when Kuchowicz et al. presented atomically resolved images of the surface.

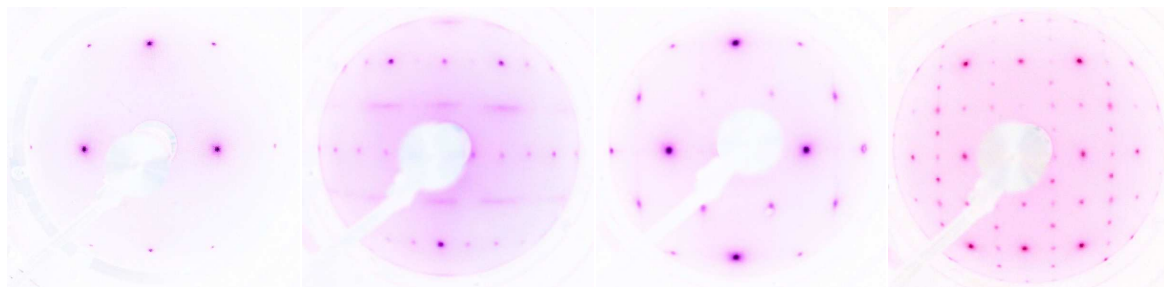


Figure 5.3 The Evolution of LEED during the silica preparation (electron energy 45-60 eV). Left to right: clean Mo(1 1 2); O₂ chemisorbed at 700 K; SiO₂-Mo(1 1 2); SiO₂-Mo(1 1 2) and MoO_x.

the final result, since the proper film flatness is achieved only within a very narrow temperature- and duration-window.

LEED

The evolution of the LEED pattern can be seen in Fig. 5.3. The clean Mo crystal reflexes form a simple rectangle in accordance with the surface unit cell and the real space lattice vectors $\bar{a}_1 = 2.73 \text{ \AA}$ and $\bar{a}_2 = 4.45 \text{ \AA}$ as shown in Fig. 5.2. During the second stage of sample preparation, the oxygen exposure results in a p(2x3) superstructure. Along the $[\bar{1} 1 0]$, the LEED displays sharp spots. Diffuse streaks along the $[\bar{1} \bar{1} 1]$ indicate a phase shift and, therefore, several possible positions with regards to the Mo lattice. The silica film displays a c(2x2)-Mo(1 1 2) diffraction pattern. The spots are clearly visible after annealing temperatures of approx. 950 K and gain sharpness with increasing temperatures even when Si-O clusters are still present. Above 1250 K the film starts to desorb and additional spots appear as a result of the formation of various MoO_x phases. Schroeder et al. executed a spot-profile analysis and identified two domains [140]. The domain boundaries propagate along the $[\bar{1} 1 0]$ direction.

The Film at the Limit of High Annealing Temperatures

A premises for imaging the silica surface with STM is an adequate flatness. During the film synthesis cluster formation occurs which prohibits stable tunneling. These undesirable features have to be removed by annealing the substrate up to 1250 K. Within a narrow temperature window of about 50 K the surface becomes atomically flat⁴. Higher annealing temperatures or prolonged heating times will result in partial or full desorption of the silicon oxide, leaving behind different molybdenum oxide phases. But even for annealing temperatures within the proper range the resulting silica film

⁴However, the film itself was found to be present already in its final structure even when the clusters still exist.

exhibits variations. At the upper end of the scale, the surface, while stoichiometric and atomically flat, starts to buckle (Fig. 5.4). Although the visibility of the buckling in the topographic images is rather faint, the cross-sectional view reveals an increase of the corrugation of $\Delta z \simeq 20$ pm with a lateral frequency of approx. 5 nm in average. The buckling is assigned to a relaxation at the interface between the molybdenum substrate and the silicon-oxide. A lattice mismatch of 8 % accounts for strain that is released once the temperature increases the mobility of the interface Mo atoms.

Most interestingly, the relaxation correlates to a change in the electronic structure of the oxide-film. Fig. 5.4 displays a series of conductance maps acquired at energies in the vicinity of the conduction-band (CB) onset. Starting at 1.2 eV, the local conductance is flat with no recognizable features. Raising the energy to 1.8 eV, differences start to develop, indicating a correlation to the topography. At 2.8 eV, the conductance exhibits a clear maximum, substantiating the conduction band onset⁵. The differences in LDOS gradually decrease until they almost entirely vanish around 3.7 eV. At that point an inversion begins to appear, shifting the increased conductance towards the area that previously had a lower LDOS. The final spectroscopic map of the series was acquired at 4.3 eV. At this energy the LDOS has reached a new maximum for those areas that did not display the CB onset previously. The local differences of the electronic structure are a new finding and have not yet been mentioned in the literature. Based on the fact that the non-perturbed areas are coherent with the CB onset for regular films, the difference is assigned to a change of the Mo–SiO₂ hybridization at the interface, which in turn acts on the silica band onsets.

5.2.2 Atomic and Electronic Structure of the Silica Film

Scanning Tunneling Microscopy

When areas in the range of some 100 nm² are imaged, the surface is atomically flat with steps occurring only occasionally. Their height of 1.2 Å corresponds to mono-atomic steps of the underlying Mo substrate. It is remarkable though, that the frequency and orientation of the steps differ between different preparations. While Wallace et al. [154, Fig. 1b] and Weissenrieder et al. [144, Fig. 1a] observed the silica steps closely related to the pristine Mo surface in frequency and orientation, Chen et al. [148, Fig. 2a] and this author found the silica steps being rather unrelated to the original substrate topography (see Fig. 5.2 and Fig. 5.4). While the steps in [148] seem to be randomly oriented, almost all images taken within this work displayed some preferential, silica related step orientation (see Fig. 5.4-derivative). Given the amount of evidence for the silicon oxide to be a monolayer in nature, the conclusion must be that under certain conditions during the preparation the Mo substrate adjusts its surface to the ad-layer. It is noteworthy that exactly the same behavior was observed for the thin alumina-film on a NiAl(16 14 1) substrate (see Cha. 4 and [123]). To ensure the premises of the

⁵In accordance with Fig. 5.9.

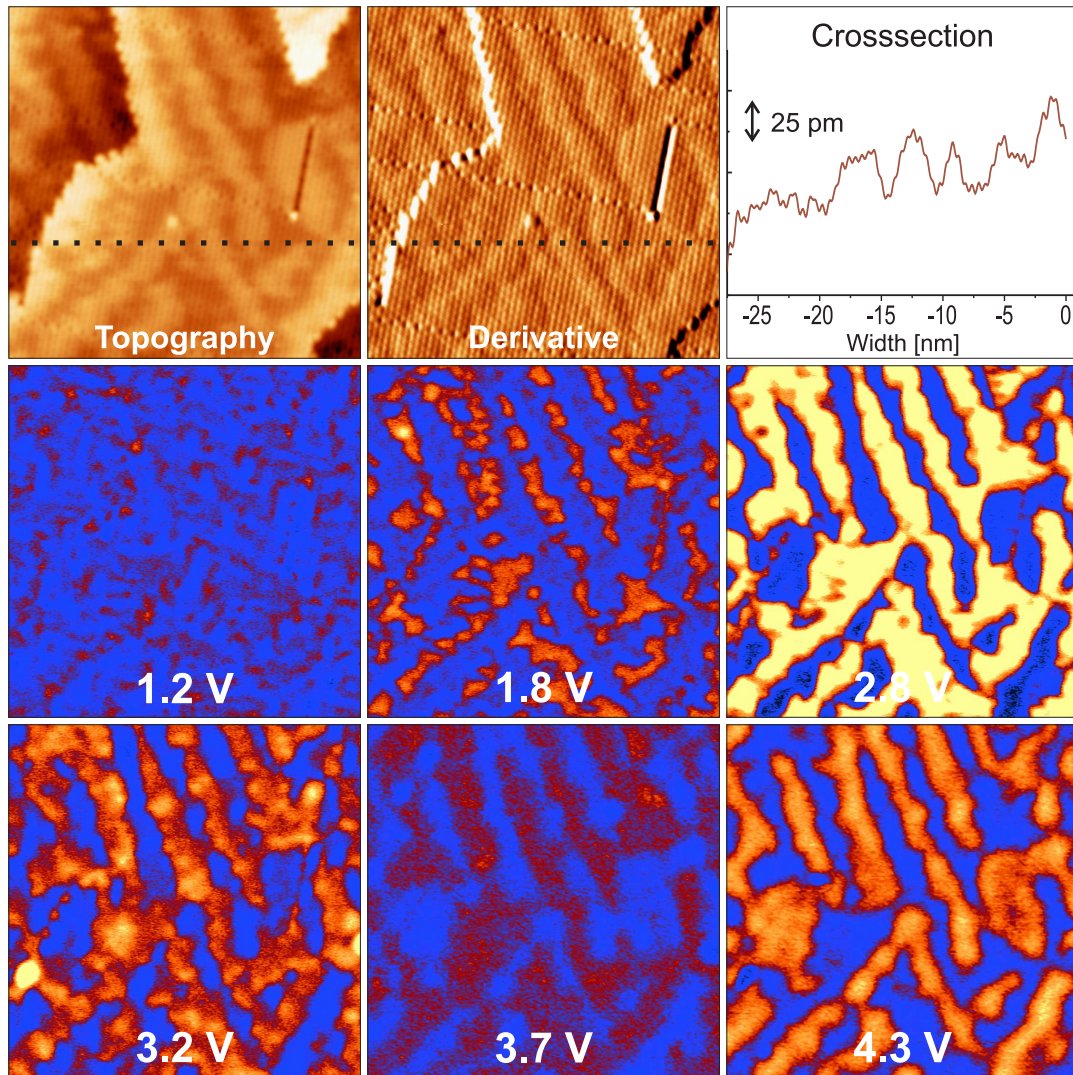


Figure 5.4 Structural and LDOS changes of the silica surface after annealing to 1280K for 300 s. Topography: 30 x 30 nm²; U_B = + 300 mV; I_T = 52 pA. The cross section along the dotted line illustrates the film buckling. Middle and lower row: conductance maps of the same surface area at bias voltages from + 1.2 V to + 4.3 V. For color code see appendix.

silica being a single layer, both field-emission resonances (FER) and STS data were acquired at various positions on the surface to identify potential differences. The FER change with the work function which by itself would change with the film thickness (see Sec. 2.2). However, no differences for measurements at the lower/upper side of the steps were found, indicating the same nature of different oxide terraces.

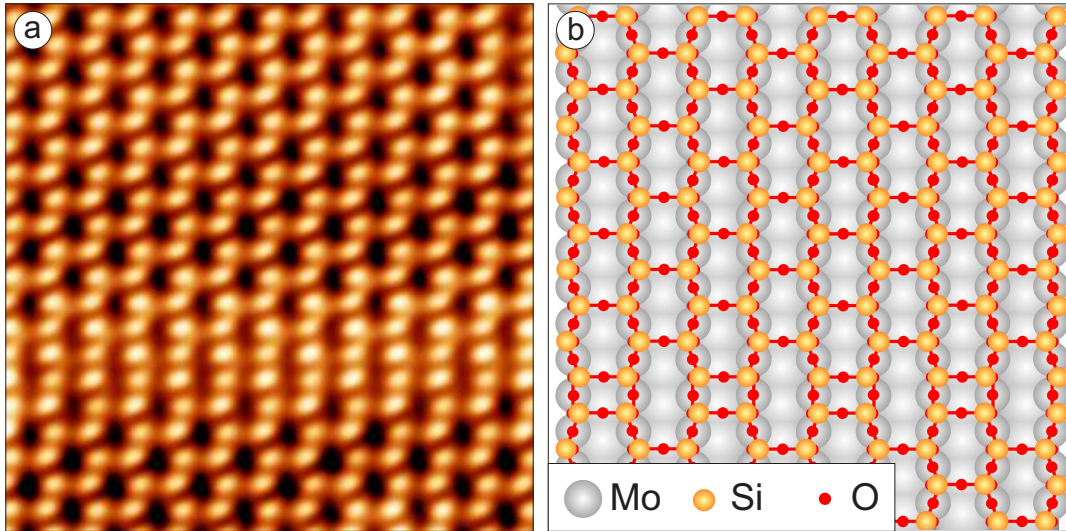


Figure 5.5 High resolution STM image and model of silica grown on Mo(112): (a) $5.2 \times 5.2 \text{ nm}^2$; $U_B = +990 \text{ mV}$; $I_T = 40 \text{ pA}$ (b) Model of the atomic arrangement within the silica layer according to [144].

At higher resolution the surface displays a honeycomb-like structure. The openings within the oxide-film appear periodically with a distance of approx. 5.5 \AA along the $[\bar{1}\bar{1}1]$ direction and approx. 5.2 \AA along the $[\bar{3}11]$ direction⁶, respectively. This periodic arrangement is conform with the $c(2 \times 2)$ pattern that was observed in LEED. While the images of the atomic array can differ dependent on the tunneling conditions (Fig. 5.6), the basic configuration is mainly as shown in Fig. 5.5a. Within the established model this surface is described as being composed of a network of corner-sharing SiO_4 tetrahedrons (Fig. 5.5b). Each Si atom (yellow) is connected via bridging O atoms (red) to three Si atoms in plane and to the Mo substrate below. The resulting structure consists of $-\text{Si}-\text{O}-$ hexagons with inner openings of approx. 3 \AA which represent micro-pores that provide access to the oxide-substrate interface. Respectively, the protrusions in Fig. 5.5a are associated with Si atoms. The film is commonly referred to as SiO_2 , although each Si atom shares three of the four O atoms it binds to

⁶The $[\bar{3}11]$ direction lies in the plane spanned by the $[\bar{1}\bar{1}1]$ and the $[\bar{1}10]$ directions but unlike the $[\bar{1}10]$ it indicates a main direction of the honeycomb with the smallest possible spacing between the micro-pores (see [144, Fig. 1c]).

with other Si atoms. Thus, the resulting stoichiometry is actually Si₂O₅ and doesn't naturally occur in bulk silica.

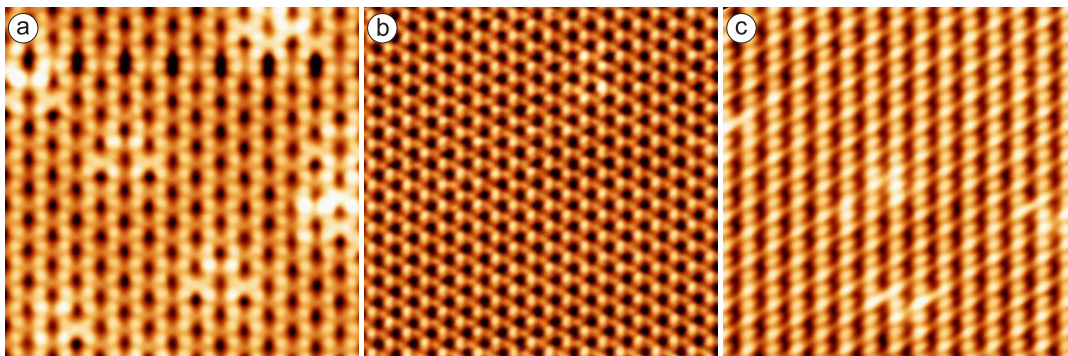


Figure 5.6 Additional representations of the SiO₂-Mo(112) surface at varying imaging conditions. (a) 6.7 x 6.7 nm²; U_B = + 30 mV; I_T = 65 pA (b) 8.9 x 8.9 nm²; U_B = + 2074 mV; I_T = 40 pA (c) 6.2 x 6.2 nm²; U_B = - 510 mV; I_T = 11 pA.

Varying the tunnel conditions leads to the promotion of different features of the surface, for example the oxygen atoms along the $[\bar{1}\bar{1}1]$ oriented Mo rows (Fig. 5.6a and red dots in Fig. 5.6b). The bridging oxygen between the rows are not visible in these images but have been observed by Kaya et al. [155]. The contrast mechanism is not conclusively identified. Several groups have acquired similar images under different tunneling conditions and different images under similar tunneling conditions. Hence, it is most likely that the atomic species at the tip-apex, which can be Pt, O, Si or some SiO_x nano-particle, is a major factor. Sierka et al. showed that additional oxygen can be incorporated into the film at the silica-molybdenum interface by altering the annealing conditions during preparation from UHV to a low-pressure O₂ environment [151]. The presence of these additional species, located at the silica-molybdenum interface, does not alter the STM images at all.

Surface Defects

The structure model in Fig. 5.5 elucidates that links of the silica units to the Mo are unspecific regarding an offset of one atomic position along the $[\bar{1}\bar{1}1]$ direction and of one row along the $[\bar{1}10]$ direction, respectively. Assuming a limited long-range mobility of the SiO₂ deposits during the growth process, the expanding oxide-patches will meet either in phase or out of phase.

Fig. 5.7b shows an APDB that has frequently been observed by Goodman's and Shaikhutininov's groups as well as within this work. The mechanism is well understood: two patches that are set apart along the $[\bar{1}\bar{1}1]$ direction are linked together by 8-membered rings instead of the usual 6-membered rings. This structural element with enlarged pore size provides an increased access to the Mo surface and plays a crucial

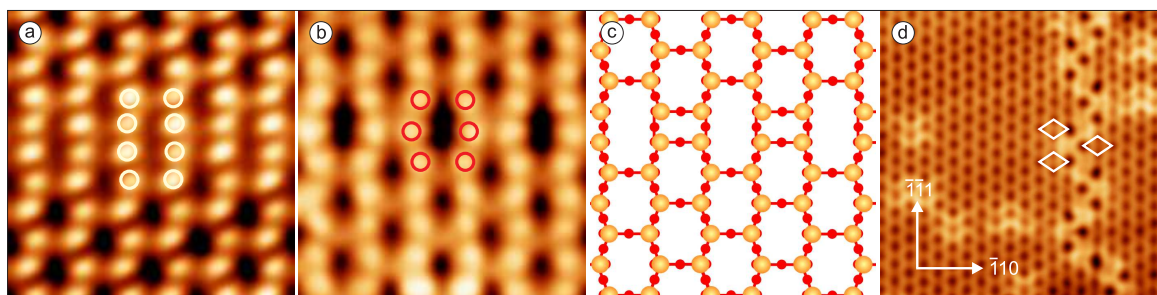


Figure 5.7 Typical defects of the $\text{SiO}_2\text{-Mo}(112)$ surface. (a) Domain boundaries along the $[\bar{1}10]$ direction representing the Si atoms ($2.9 \times 2.9 \text{ nm}^2$; $U_B = +990 \text{ mV}$; $I_T = 40 \text{ pA}$) (b) APDB similar to (a) representing the O atoms instead ($2.9 \times 2.9 \text{ nm}^2$; $U_B = +30 \text{ mV}$; $I_T = 65 \text{ pA}$) (c) Model for (a+b), Si atoms show in yellow, O atoms in red (d) Domain boundaries along the $[\bar{1}\bar{1}1]$ with unresolved atomic structure; diamonds indicate the preservation of the pore geometry ($8.9 \times 8.9 \text{ nm}^2$; $U_B = +990 \text{ mV}$; $I_T = 21 \text{ pA}$).

role in the adsorption experiments hereafter. A second APDB type, which is expected from the geometrical relationship of the Mo and silica lattice, was observed rather seldom (Fig. 5.7d). An out-of-phase growth along the $[\bar{1}10]$ direction results in the necessity to bridge two trenches of the Mo substrate, which can not be achieved by mere continuation of the regular silica assembling. The detailed atomic structure of these film-features could not be resolved yet. Nevertheless, the well visible pores appear to have two main characteristics. First, they are positioned where a pore in the undisturbed film would be expected (see diamond-shapes in Fig. 5.7d). Second, they are arranged in groups of three, like triangles that alternately change the orientation by 180° when moving along the $[\bar{1}\bar{1}1]$ direction.

Comparison of the STM Results with Other Methods

While STM can elucidate the surface morphology, it is mostly incapable to distinguish different atomic species. With a typical energy range of some hundred eV, XPS is focusing on the electronic core levels, and with this it is specific to the chemical composition and stoichiometry of the sample surface. Any chemical bond results in a new equilibrium configuration not only of the valence electrons but of all wavefunctions. Consequently the core levels adjust according to the oxidation state of the metal cations. In addition, the localization of species in the surface is possible as well, despite the probing depth of XPS, by applying the irradiation at an angle to the surface normal.

The application of XPS to the silica film concentrates on Si $2p$, O $1s$ and Mo $3d$ levels (Fig. 5.8). The data from the Si $2p$ region displays a single peak at approx. 103 eV. In full agreement with the 2D-network model, this feature was assigned to tetrahedrally coordinated Si in the nominal oxidation state +4, as it is well documented in the

literature [156, 157]. Within the energy range typical for the oxygen 1s level, two maxima were observed⁷, both indicating the presence of at least two different oxygen species. Min concluded that the lower binding-energy (BE) feature relates to the Si–O–Si bonds and the higher BE reflects the Si–O–Mo bonds. Additional angular-dependent XPS measurements with synchrotron radiation taken by Weissenrieder et al. and the theoretical framework provided by Todorova manifested the two species as Si–O–Si bonds (532.5 eV) at the surface and Si–O–Mo bonds (531.2 eV) at the interface, the latter showing reduced intensity for grazing incident angles. Annealing the deposited silicon in the presence of small oxygen pressures instead of UHV leads to additional incorporation of O atoms at the molybdenum/silica interface. This results in an additional XPS feature at 530.6 eV for the O1s levels. Concurrently, the Mo 3d region displays a shoulder at the higher BE side due to the additional charge transfer by the O–Mo bonds.

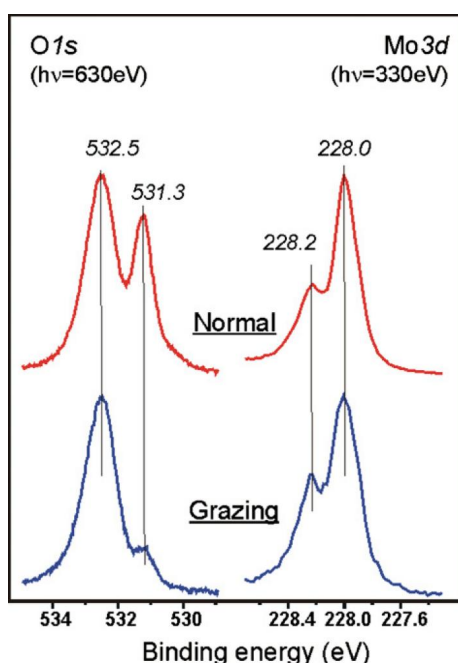


Figure 5.8 Photo-electron spectra of the SiO₂-Mo(112) film for the O 1s and the Mo 3d regions acquired with beam energies of 630 eV and 330 eV, respectively. The upper (red) curve shows the result for an incident beam normal to the surface. The lower (blue) curve was measured at a beam angle of 80° with regards to the surface normal [149, Fig. 4]

Another method suitable to identify surface species and configurations is infrared reflection absorption spectroscopy (IRAS). The technique focuses on the phonon spectrum which itself is a function of symmetry and bonds. Not all modes that are present can be detected though. The dipole selection rules require that the vibrations are symmetric with respect to all symmetry-operations of the surface symmetry group, since only those possess a dynamic dipole moment perpendicular to the metal surface that will contribute to the IR absorption. Three significant dips are present in the IRAS spectra, at 1059 cm⁻¹ (131 meV), at 771 cm⁻¹ (96 meV) and at 675 cm⁻¹ (84 meV). In

⁷Schroeder et al. [140] reported them at 532.0 eV/530.3 eV, while Min et al. reported peaks at 532.2 eV/530.7 eV [143].

accordance with the *cmm* symmetry group of the silica-film based on the 2D-model, these features are assigned to the asymmetric Si-O-Mo stretching, the Si-O-Si symmetric stretching coupled with Si-O-Si bending and a coupling of Si-O-Si bending modes with O-Mo vibrations at the interface, respectively [144].

Though the STM was generally found to be suitable for vibrational spectroscopy (see Fig. 3.15), the attempt by the author to acquire some IETS data within the relevant energy range of 80-140 meV was not successful.

Scanning Tunneling Spectroscopy

The identification of the local density of states was performed by tunneling spectroscopy. The results are presented in Fig. 5.9. The dI/dV plot shows the (convolution of the) tunneling currents rise with increasing $|U_{\text{Bias}}|$ and the contribution from states within the surface layer. An onset of increasing conductance translates into a peak of the derivative (Sec. 2.2). On this basis, the upper limit of the valence band was determined to -3.8 eV and the onset of the conduction band to +2.9 eV. For regularly annealed silica-films, these numbers were consistent across the sample surface and for different sample preparations. The Mo *d*-band, which energetically lies within the surface band gap, plays no significant role at the surface. The total width of the band gap amounts to 6.7 eV, a number much smaller than the comparable bulk values of 8.9 eV for α -quartz and 8 eV for β -cristobalite. This is not surprising, given that ultra-thin films of wide-gap oxides require two or three layers to develop the properties of the bulk materials and their respective surfaces [158]. Model calculation deliver band-gaps of 6 eV [159] and 5.3 eV [158] and are supposed to be underestimating, as it is common for DFT results.

Several experimental studies are available for comparison with the STS results⁸. Ref. [142, 149, 160, 161] describe the valence-band structure with a focus on its main features. Kim et al. give a specific value of - 4.4 eV for the VB edge. While none of the other studies gives an exact number the PES data from [160] seems to have the valence band onset close to 4 eV, while [161] and [149] indicate a value closer to 5 eV.

It is obvious from Fig. 5.9 that the band edges are lying asymmetrically with respect to the Fermi level. This phenomenon has also been observed previously for other supported thin-film oxides, including TiO₂, MgO and Al₂O₃. A similar, though much more pronounced effect was found for Li-atom adsorption at the Mo(112)-SiO₂ interface, where charge transfer from Li to Mo induces an interface dipole that bends the bands downward and lowers the work function [162].

⁸No other method allows such easy access to both conduction- and valence-band states at energies close to E_F . Alternative methods measure either occupied or unoccupied states and only combined give a complete description of the band structure. At larger energies, though, STS becomes unsuitable, partially because of the general increase of the LDOS with energy and partially because once vacuum energy has been reached, vacuum resonances (FER) begin to dominate the conductivity.

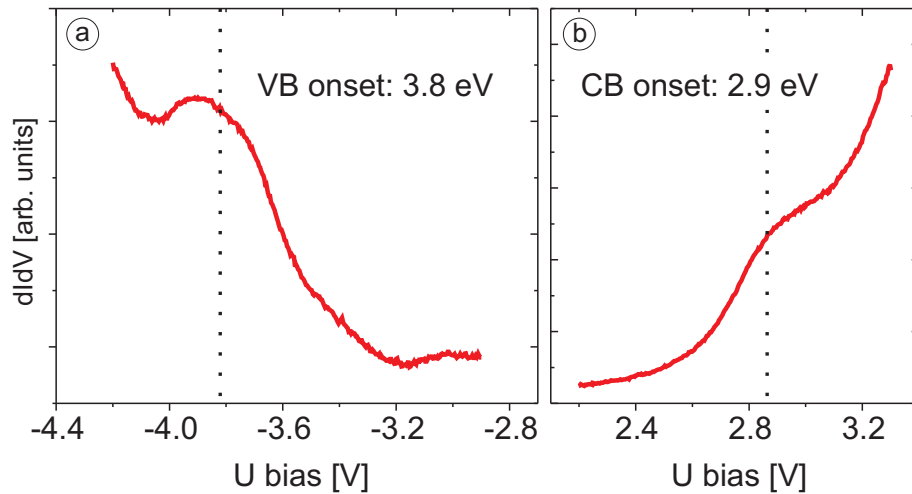


Figure 5.9 Tunnel-spectroscopy of the band-gap region of the SiO₂-Mo(112) surface, probing (a) the valence band, made up from O $2p$ states and (b) the conduction band, made up from Si $3s, p$ states. The signal between - 2.8 V and + 2.3 V did not indicate the presence of additional states and has therefore been omitted in the graph.

According to the STS measurements of the thin silica film the bands are shifted downwards by 0.45 eV with respect to the symmetric position. An earlier theoretical study suggested that the bands would shift upwards instead [163]. Within this analysis, an emphasis was put on the fact that bonds are formed at the SiO₂-Mo(112) interface between the Si-O dangling bonds of the silica structure and the Mo surface. Charge flows from Mo to interface oxygen atoms which leads to an interface dipole that is negative on the oxide side. Another theoretical study that compares the band structure of the SiO₂-Mo(112)-complex with α -quartz (surface and bulk) [158] places the CB edge closer to the Fermi level, which divides the band-gap by a ratio of $\approx 4:3$ for the empty to filled part.

Band positions are not only a result of the interface-dipole and the respective charge-transfer. Direct chemical interactions like the formation of interface states and metal-induced gap states (MIGS)⁹ are also a relevant factor [164]. Therefore it is possible for the bands to down-shift despite the charge transfer. Support for this description is obtained from NEXAFS measurements, the only other experimental data available on the unoccupied states [149]. The study focuses on transition from the oxygen K-edge into unoccupied O $2p$ states, in accordance with the dipole selection-rules. The results are shown in Fig. 5.10 (from [149, Fig. 6]). The most prominent feature is an absorption band in the range of 5-10 eV. A smaller feature appears at ≈ 2.4 eV. Both, position and height of this feature might indeed indicate the presence of a MIGS [164].

⁹MIGS occur at metal-semiconductor or metal-insulator contacts, whereat the metal wave functions penetrate into the semiconductor, leading to the formation of new electronic states.

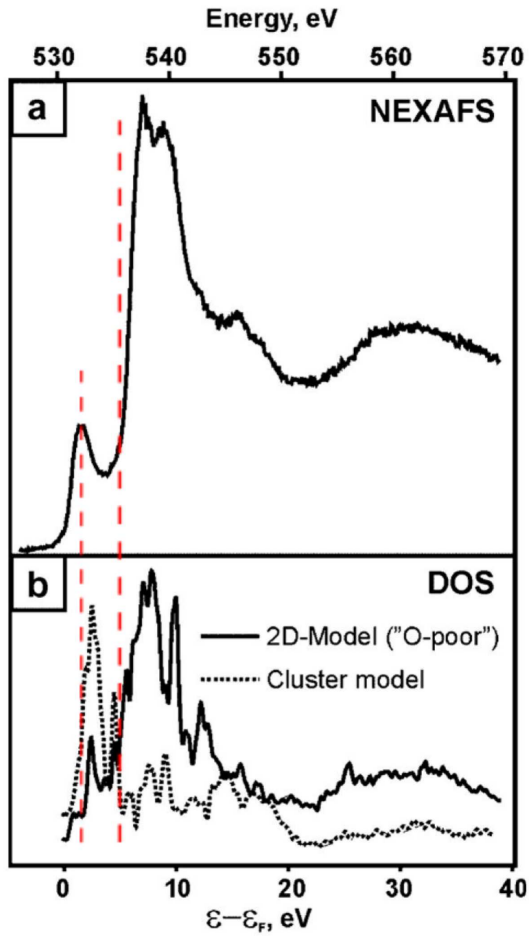


Figure 5.10 (a) NEXAFS spectrum of the silica film at energies of the oxygen K-edge. The E-field vector of the synchrotron light was parallel to the $[\bar{1}10]$ direction. (b) Model calculations of unoccupied states. Within this work, only the 2D-network model has been considered. Both, the measured and the computed spectra display an onset at around 2.5 eV, followed by a larger peak ranging from approx. 4.5 eV to 10 eV.

Considering the uncertainty of extracting these numbers the agreement of the values with the STS data is acceptable.

Finally it shall be noticed that the conductance maps of the highly-annealed and buckled films coincide with the above explanation. The buckling leads to sections where the film is in close proximity to the metal surface and displays the state at 2.9 eV. In other sections, where the film is assumed to have an increased distance to the Mo-support and the influence of metal induced state is weaker, therefore the 2.9 eV feature vanishes.

5.3 Application of an Ultra-thin Silica Film as Atomic Sieve

The focus of this chapter is the study of the adsorption characteristics of the ultra-thin silica film on Mo(112). In particular the binding behavior of low-density deposits of Pd, Ag and Au atoms was investigated experimentally and compared to the results of density functional theory (DFT) calculations. These three species were chosen because (i) they exhibit either comparable van-der-Waals radii (Pd and Au) or (ii) similar electronic properties (Ag and Au). (iii) Previous research showed that the cluster formation of Pd and Au on ultra-thin silica deviates from the findings for other oxide supports and needs in-depth analysis of the initial nucleation mechanism, ideally at the single-atom level.

All experiments were carried out with the newly-build STM that was described in detail in Chapter 3. In addition to the topographic characterization of the surfaces via tunneling-microscopy, the electronic properties of the samples were investigated by scanning tunneling spectroscopy and conductance mapping (see Sec. 2.1 and 2.2). The typical temperature during the measurements was 9.5 K. Spin-polarized DFT calculations, performed by Pacchioni's group, were done by applying the generalized gradient approximation as implemented in the VASP code, the PW 91 exchange-correlation functional and a plane-wave basis set (energy cut-off 400 eV) [165–167]. The electron-ion interaction was described by the projector augmented wave method [168]. The regular sites in the silica film were modeled with a (4 x 2) super-cell containing 7 Mo layers ($\text{Mo}_{56}\text{Si}_8\text{O}_{20}$), while a (5 x 2) cell with 4 Mo layers was used for the anti-phase domain boundaries (APDB) ($\text{Mo}_{40}\text{Si}_{10}\text{O}_{25}$). The slabs were separated by 10 Å of vacuum. Penetration barriers were determined by moving the adsorbed metal atoms along the surface normal into the oxide-pore and relaxing the metal/oxide complex for each vertical distance. The computed barriers do not correspond to a real transition state and slightly overestimate the actual barrier height [169]. STM images for comparison with the experimental data were simulated using the Tersoff-Hamann approach, that assumes an *s*-like wave-function as outermost probe-orbital [58].

Adsorption Behavior of Single Metal Atoms

In these experiments the silica samples were prepared as described above, pre-cooled on the manipulator to approx. 100 K and transported into the cold STM. The thermal link of the sample-holder inside the STM is rather weak and the time for cooling can take several hours. Once the drift between the tunnel electrodes vanishes the STM and the sample are assumed to be in thermal equilibrium. The metal deposits Pd, Ag and Au were evaporated from high purity (99.95%) wire onto the cold sample. Due to the infrared radiation of the evaporation sources and the room-temperature

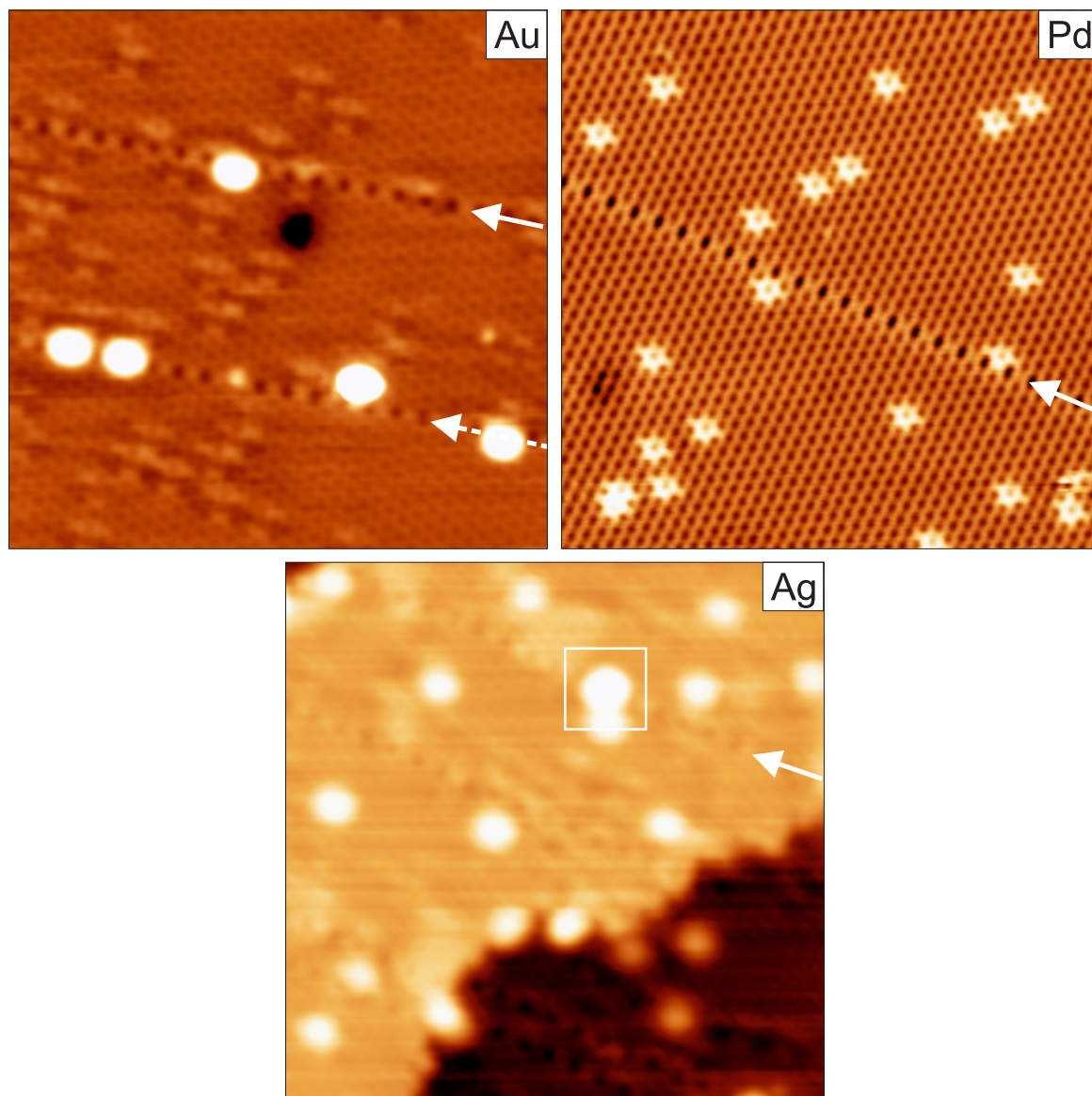


Figure 5.11 Characteristic appearance of the silica surface after the deposition of Au (left), Pd (right) and Ag (middle). Displayed are **Au**: 20 x 20 nm², U_B = +1800 mV, I_T = 20 pA, **Pd**: 22 x 22 nm², U_B = +1124 mV, I_T = 40 pA, **Ag**: 20 x 20 nm², U_B = +2000 mV, I_T = 20 pA.

background¹⁰, the sample temperature increases to approx. 20K for the duration of the deposition. The thermal energy of the incoming metal atoms is with $E = kT \simeq 100$ meV very high, which ensures transient diffusion into their equilibrium adsorption site. Two different sources were employed. Pd wire was heated inside of an alumina crucible, while Ag and Au wires were wrapped around tungsten filaments and directly heated. E-beam heating was deliberately avoided since the acceleration of the metal ions has a sputtering effect on the target.

The impact of the evaporated species on the oxide morphology is instantaneously visible in the STM images (Fig. 5.11). The nominal coverage was the same for all three materials and amounted to 5×10^{12} atoms/cm². In each case the adsorbates appear as bright protrusions, but shape and location of the features differ noticeably for the individual species. Each image within Fig. 5.11 includes at least one APDB indicated by white arrows to illustrate differences of the adsorption between the regular and the altered film.

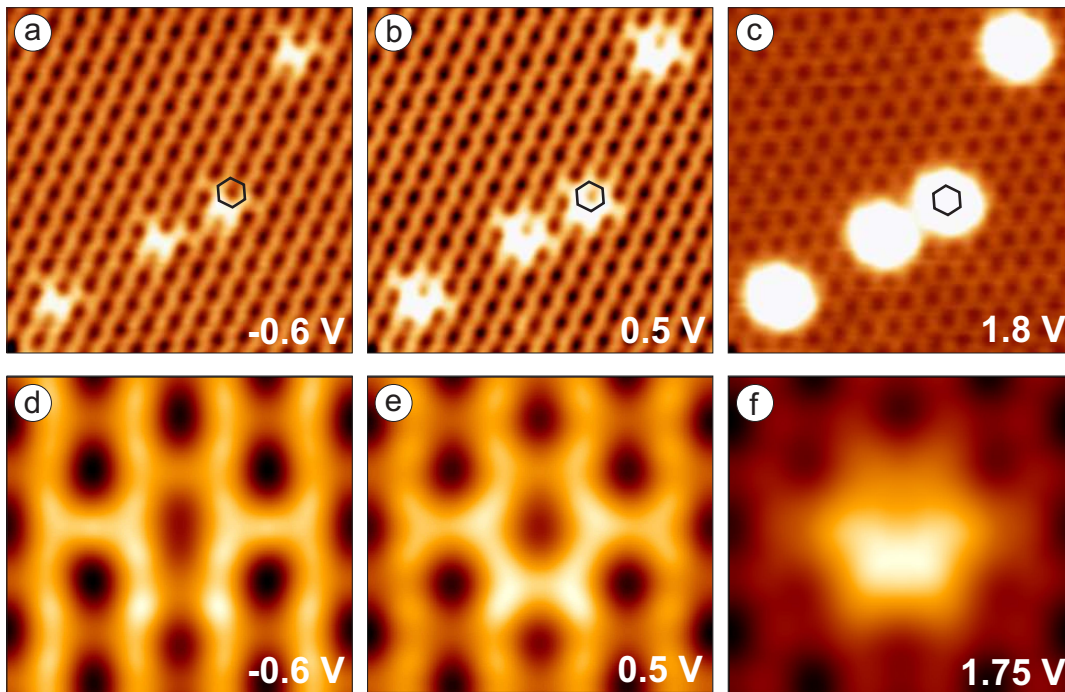


Figure 5.12 Pd: Bias dependent topography for Pd on the silica film. (a-c) STM images (6.5×6.5 nm², $I_T = 40$ pA) acquired at three different bias voltages. (d-f) Computed images (1.8×1.5 nm²) based on the Tersoff-Haman method for the same voltages.

¹⁰ $\lambda(300\text{ K}) \simeq 9.6\mu\text{m}$

Palladium: The Pd-related features have a unique, star-like shape that in its form and extension resembles a part of the structure of the silica film itself but with an increased topographic height. The atoms are randomly distributed over the surface with no preference for a specific site. The presence of a domain boundary does not alter the appearance of the Pd features at all. The fact that two Pd are located in the immediate vicinity of the APDB without being placed directly on it indicates that this surface feature has no significance in the adsorption process. Complementary information was generated by measuring the dependence of the Pd features on the bias-voltage (energy) and by comparing the data with model calculations based on the Tersoff-Hamann approach. The results are shown in Fig. 5.12. The upper row displays experimentally acquired STM images for three bias voltages. For one specific location a hexagon was superimposed to indicate the position of the six Si-atoms that surround a Pd related feature. At small negative energies (-0.6 V) the overall corrugations is low with a slightly increased conductivity being located between adjacent pores along the $[\bar{1}\bar{1}1]$ direction. Changing the polarity to small positive voltages (+0.5 V) leaves the corrugation of the regular surface basically unchanged. The appearance of the adsorbate-hosting region has evolved though, displaying the distinct, star-like shape that was already visible in Fig. 5.11. The pores of the silica film are seemingly unchanged and the increased contrast is located within the silica network that surrounds the opening. Only for higher positive bias voltages (+1.8 V) the features increase in width and height and now have a topographic maximum in the center. This distinct contrast progression indicates the penetration of Pd atoms through the holes inside the silica film and their attachment to the Mo surface. Most probably the binding takes place at two-fold bridge sites of the lower Mo rows [146]. The fact that these sites are not in the the center of the silica-pores but offset along the $[\bar{1}\bar{1}1]$ (see the model in Fig. 5.17) is consistent with the asymmetric appearance of the protrusions in Fig. 5.12a. The calculated images (Fig. 5.12d-f) display an area of $2 \times 2 \text{ nm}^2$ and include a Pd atom in the described adsorption site. The corrugation follows exactly the same evolution as in the measured images. In particular the increased DOS within the silica film is reproduced very well.

Silver: The Ag species are easily distinguishable from the regular silica film and are like the Pd randomly distributed across the surface (Fig. 5.11 bottom). The size of the features is very homogeneous, indicating that the species are of single-atomic nature. The only exception is an adsorbate that is obviously located within an APDB and appears to be larger. The image includes a step and though several features are located directly on the edge, no particular preference for this site is indicated. Compared to Pd, the Ag atoms are more pronounced in the topography at similar bias voltages, that is the Ag atoms contribute more to the LDOS around E_F . Fig. 5.13 compares measured STM images (a+b) to simulated ones (c+d) at several bias voltages. At -0.25 V a star-like feature appears in the topography, very similar to the Pd related feature

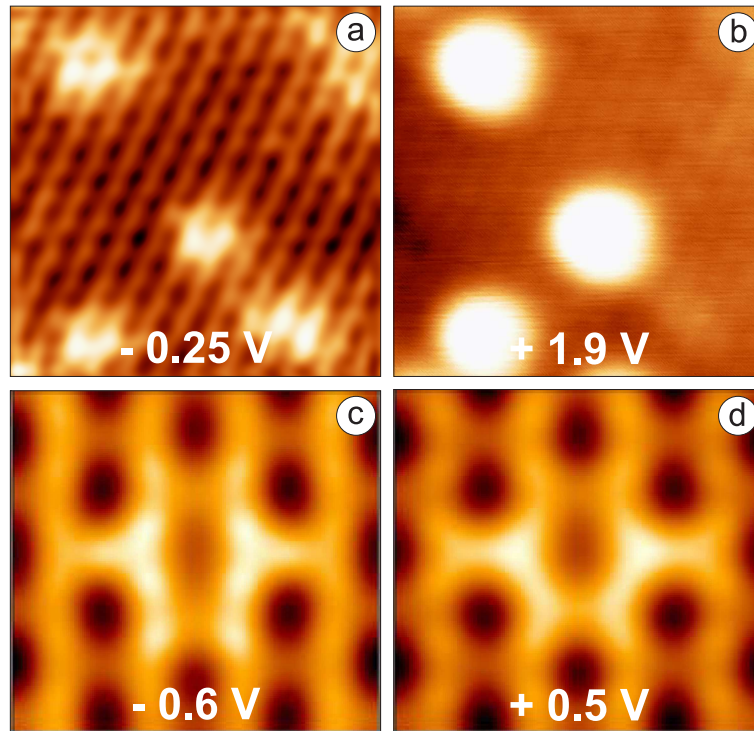


Figure 5.13 Ag: Bias dependent topography for Ag on the silica film. (a-b) STM images ($6.5 \times 6.5 \text{ nm}^2$, $I_T = 30 \text{ pA}$) acquired at two different bias voltages. (c-d) Computed images ($1.8 \times 1.5 \text{ nm}^2$) for small negative and positive bias voltages.

at small positive voltages. Though the simulated image in Fig. 5.13c is based on a slightly lower voltage, the resemblance of the experimental data is unambiguous. As in the previous case, the presence of the pronounced hexagons indicates that the Ag-species are able to penetrate the holes of the $-\text{Si}-\text{O}-$ hexagons. For voltages ranging from -0.5 V to $+0.5 \text{ V}$ little variation of the topography is observed. Once the bias voltage exceeds $\simeq 1 \text{ V}$, the Ag features become round, pronounced protrusions with the highest corrugation in the center. Contrary to the Pd species, the Ag atoms display a certain affinity to interact with the APDB (see arrow in Fig. 5.11). Not only is an Ag atom placed there (square) but its appearance has changed as well, giving it an increased pronunciation in the topography. Based on the analysis of several STM images, the overall fraction of Ag atoms bound to APDB was determined to be approx. 5%. Considering that only 2% of all available binding sites are located along the domain boundaries, the probability to find Ag in defective $-\text{Si}-\text{O}-$ octagons is 3-5 times higher than in regular hexagons, suggesting a lower penetration barrier at the APDB.

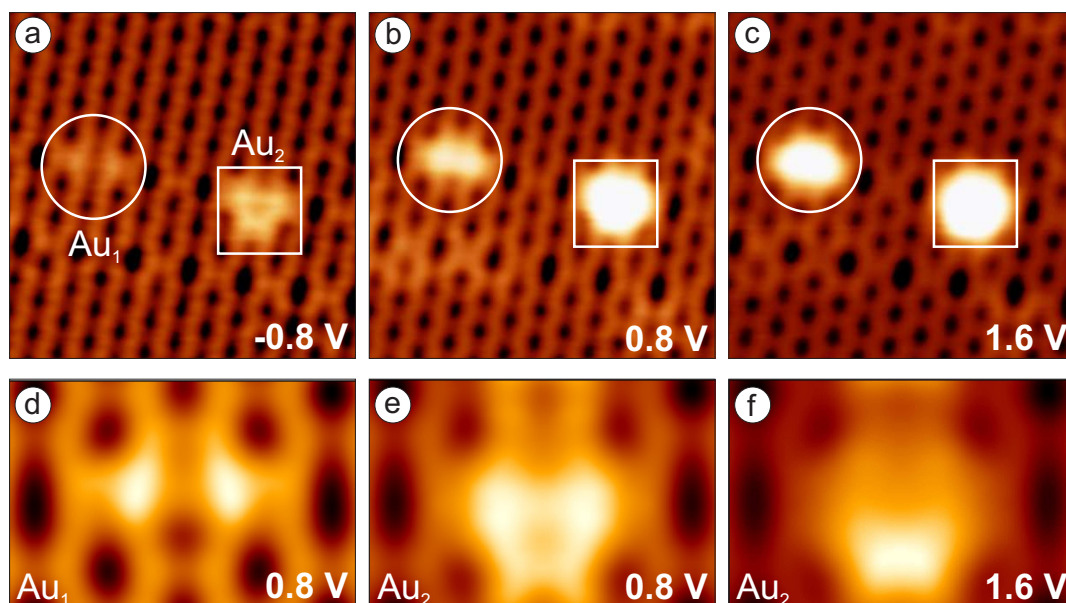


Figure 5.14 Au: Bias dependent topography for Au on the silica film. (a-c) STM images ($5.5 \times 5.5 \text{ nm}^2$, $I_T = 32 \text{ pA}$) acquired at three different bias voltages. The circle indicates a singly and the square a doubly filled oxide pore. (d-f) Computed images ($2.2 \times 1.3 \text{ nm}^2$) with $V_B = 0.8 \text{ V}$ for the Au₁ and with $V_B = 0.8 \text{ V}/1.6 \text{ V}$ for the Au₂ species.

Gold: The adsorption of Au on the silica surface follows a distinctively different pattern (Fig. 5.11 right). Most of the surface area remains unchanged after the deposition, a phenomenon that does not change even for higher deposition amounts. The absence of gold atoms across the defect-free surface areas suggests that they are unable to pass the holes in the $-\text{Si}-\text{O}-$ hexagons and in addition do not bind atop the surface either. Apparently the penetration barrier exceeds the thermal energy of the Au atoms at their arrival on the surface ($kT \approx 90 \text{ meV}$, based on the sublimation temperature). Instead, the Au-related features are exclusively found directly on the domain boundaries, as pointed out in Fig. 5.11. The fact that Au aggregates line up along these APDB indicates the ability to interact with the wider, eight membered $-\text{Si}-\text{O}-$ rings. The exact positions with reference to the octagon-shaped openings show minor variations. Within the extension of the the enlarged pores several binding sites along the $[\bar{1}\bar{1}1]$ direction are seemingly possible. Fig. 5.14 shows a set of high resolution STM (a-c) and simulated images (d-f). The domain-boundaries are clearly visible across the center region of the image, as is the incorporation of Au atoms within this surface feature. At small bias voltages, the pores stay visible and additionally a confined region in close proximity to the opening along the $(\bar{1}\bar{1}1)$ direction displays increased contrast. As deduced from DFT calculations, this characteristic contrast substantiates a structural distortion of the $-\text{Si}-\text{O}-$ octagon to allocate more space for

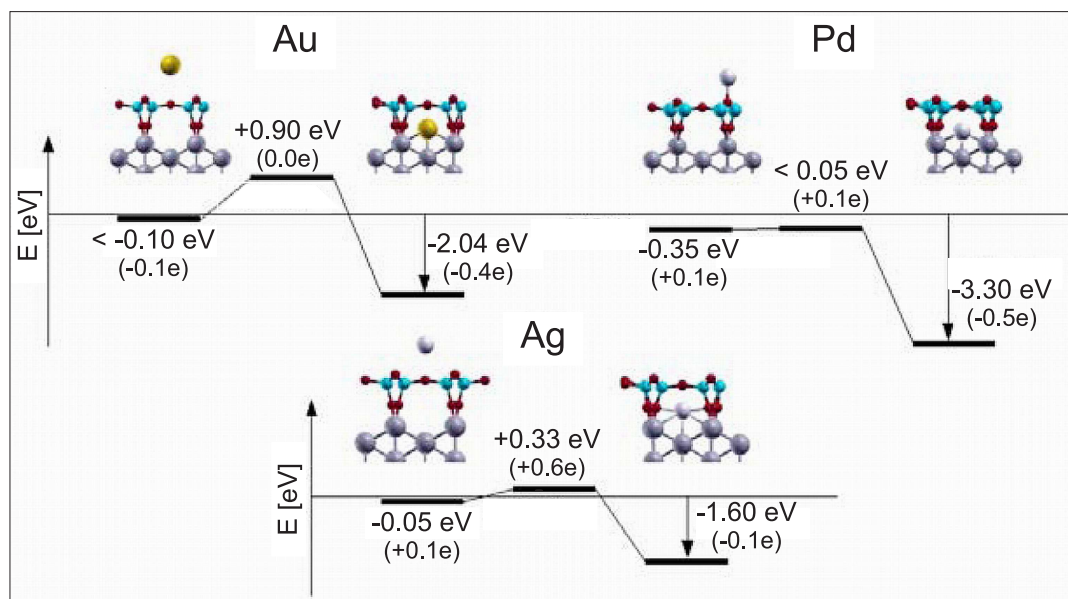


Figure 5.15 Potential-energy curves describing the energetic conditions at different stages of the adsorption process for Au (left), Pd (right) and Ag (middle). Each curve starts to the left with the binding energy on top of the oxide surface, followed by the potential barrier for film penetration and ending with the binding at the interface. All energies are given with respect to a gas-phase atom. For each element, models of two binding configurations are inserted at the upper part of the image: on top of the film (left) and at the interface (right). The Bader charges that occur during the penetration are added in parenthesis.

the incorporation of the Au atom. A comparison between the STM data Fig. 5.14b acquired at +0.8 V with the corresponding calculated images Fig. 5.14d+e, allows to differentiate between a single- (circle) and a double-occupancy (square) of the octagonal holes. The deposited amount of Au would make it likely that more sites along the APDB are hosting individual atoms. Instead, based on the appearance of the Au aggregates at increased bias voltages (Fig. 5.14c+f), the majority of adsorption sites is at least doubly occupied. It is unlikely that the Au atoms form dimers or trimers while still above the surface. Hence, a single atom inserted into an eight-membered ring already forms the critical nucleus for Au aggregation and initiates the growth of small particles [143], that are clearly revealed in Fig. 5.11.

The experimentally determined adsorption behavior of the three atomic species was compared to DFT calculations. Fig. 5.15 illustrates the computational energy profiles for the insertion of Pd, Ag and Au atoms into regular six-membered rings of the silica film. The energy values of each plot denote the binding energy on top of the film on the left, inside the film on the right and within the barrier for penetration. All energies are given with respect to a gas-phase atom. The binding configurations of

the different atoms above and below the silica film are shown in the insets (Mo: large gray, Si: medium blue and O: small red spheres).

The lowest barrier height to pass the regular $-\text{Si}-\text{O}-$ hexagons was found for Pd atoms. The value is less than 0.05 eV and therefore nearly negligible. Once an atom has overcome the barrier it binds to the Mo interface at a bridge-site with 3.3 eV. According to a Bader analysis¹¹, the Pd remains neutral during penetration ($4d^{10}5s^0$ configuration), but becomes slightly negatively charged (- 0.5 e) in its final binding arrangement. The energies for penetration and binding are similar for both ring-types, hexagons and octagons, which explains the non-preferential distribution of Pd atoms across the silica surface. Even in the vicinity of the APDB the Pd incorporation appears to be unaffected (Fig. 5.11).

The energy barrier for penetration of Ag atoms into the six-membered $-\text{Si}-\text{O}-$ hexagons is with 0.33 eV much higher than for Pd (Fig. 5.15 bottom). Assuming an Arrhenius behavior, thermal Ag atoms have a 30 times lower penetration probability than Pd atoms. However, this is still enough to lead to measurable amounts of incorporated species under the given experimental conditions. The Ag atoms are able to overcome this barrier only at the moment of impact. After thermalization, the atoms are weakly trapped in a physisorbed state (≈ 0.1 eV) and diffuse across the surface until they reach an adjacent domain boundary where penetration is still possible. The ability to remain mobile on the surface for a short time might be responsible for the higher adsorption rate of Ag atoms at APDB with respect to regular oxide hexagons. Once the micro-pore is passed, Ag binds to the SiO_2 -Mo(112) interface with 1.6 eV and remains in a neutral ($4d^{10}5s^1$) configuration similar to the state above the surface. The binding energy is substantially lower for Ag compared to Pd due to the chemically inactive nature of the energetically low-lying Ag $4d$ states.

In the case of Au atoms the penetration barrier increases to 0.9 eV. The probability to reach a high-binding site at the SiO_2 -Mo(112) interface is therefore four orders of magnitudes lower than for the Pd atoms, which explains the complete absence of Au adsorbates in defect-free film-regions. The lack of admittance into the six-membered $-\text{Si}-\text{O}-$ rings is not only kinetically induced. The binding energy of Au to the silica surface is with 0.1 eV much lower than the penetration barrier. Hence, an increased sample temperature would lead to desorption rather than admittance. Along the domain-boundaries where the pores are elongated and high-binding sites at the interface are accessible without any significant barrier, Au atoms are able to pass through the oxide surface. While they are in a neutral state above the silica film ($5d^{10}6s^1$ configuration), they become partially negative charged (- 0.4 e) at the interface due to electron transfer from the Mo substrate.

¹¹The Bader analysis determines the charge distribution in chemical bonds, leading to (hypothetical) partial charges. The method assumes the separation of the binding partners by an inter-atomic surface $S(r_s)$ with zero-flux $\nabla\rho(r_s) \cdot \vec{n}(r_s) = 0$.

Analysis of the Selective Binding Behavior

The origin of the different penetration barriers and the significantly different values for each of the three metals shall be discussed next. An initial assumption would link the barrier height to the size of the respective gas-phase atoms, as given by their van-der-Waals radius [170]. Following this model, smaller atoms should exhibit a lower barrier height than larger ones. This trend is indeed observed for Pd and Ag with increasing van-der-Waals radii of 163 pm and 172 pm, respectively. However, the penetration barrier for Au is substantially higher, in spite of the fact that its van-der-Waals radius is due to the relativistic contraction of the Au orbitals relative small. With 165 pm, the value for Au lies between the ones for Pd and Ag. Accordingly, the atomic radius is an inadequate parameter to explain the observed sequence of increasing barrier heights. In a more sophisticated model, the permeation process is linked to the repulsion that is exerted by the charge density of the oxide on an incoming atom. The main source for this repulsion are the occupied O $2p$ -states. This type of interaction is dominated by the spatially most expanded ad-atom orbital, that is to say the s -like valence state.

Due to its unfilled nature, the Pd $5s$ orbital induces a weak repulsion and the resulting penetration barrier is only small. In comparison, the half-filled Ag $5s$ and Au $6s$ orbitals interact much stronger with the surface O $2p$ states during the ingress. Nevertheless, the difference between the two latter species is even larger than between Pd and Ag. The surprising result that the energy barrier for Ag is three times lower than for Au can be explained by a transient positive charge of the Ag atoms during passage of the oxide plane. In the course of admission, the Ag atoms transfer charge density from their $5s$ orbitals into the Mo states. This effect is clearly resembled in the computed Bader charge of $+0.6 e$ for an Ag atom when being inside the plane of the oxide ions. A similar mechanism is not available for Au atoms. They are strongly electro-negative species and rather accumulate excess-electrons into the Au $6s$ orbital than transferring charge to the adjacent atoms [171,172]. Consequently, Au remains neutral when passing through the oxide pore in the silica film. Another way to facilitate an easier passing through the oxide surface would be an internal charge redistribution by promoting the $6s$ electron into a state with leaner orbitals. The $6p_z$ state for instance is less extended with its electron density being localized in line with the ingress trajectory. But the reconfiguration is inhibited by the high activation energy for the $s - p$ transition of the Au $6s$ electron of 4.6 eV [173]. The Au atoms are therefore unable to lower the repulsive interaction with the oxide surface electrons and hence, the penetration barrier remains high.

Electronic Properties of the Metal-Atom Adsorbates

Finally, the electronic characteristics of the incorporated metal-atoms should be described in more detail. Fig. 5.16 shows conductance-maps of Pd (top) and Ag (bottom)

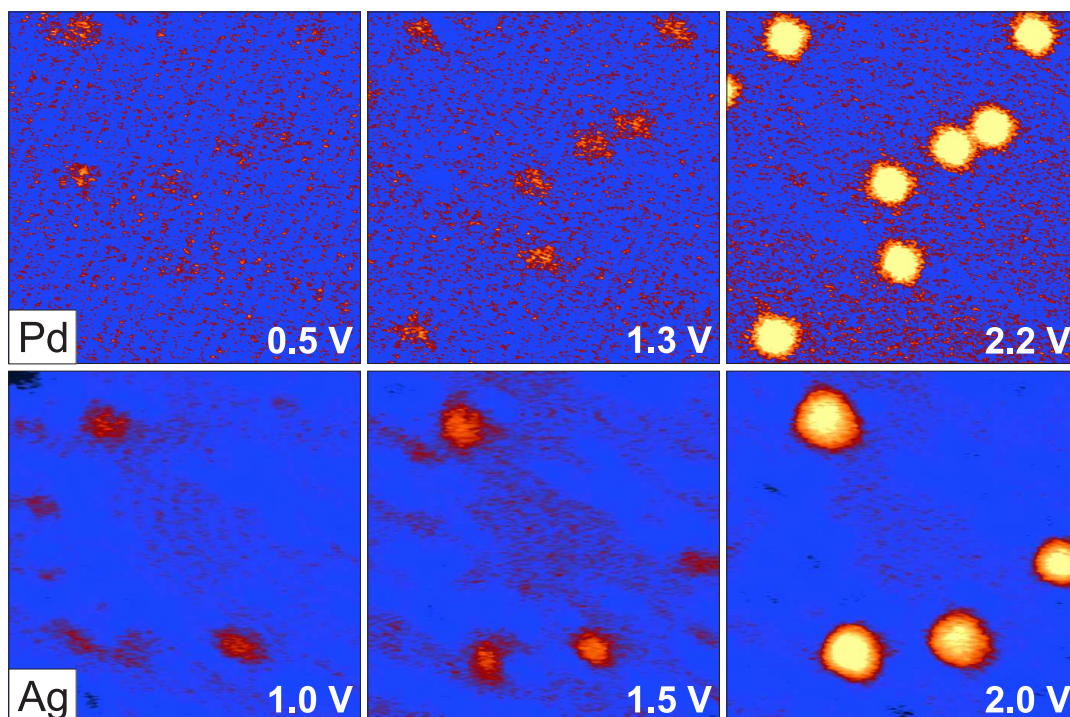


Figure 5.16 Conductance maps of Pd (top, $13 \times 13 \text{ nm}^2$, $I_T = 50 \text{ pA}$) and Ag (bottom, $12 \times 12 \text{ nm}^2$, $I_T = 32 \text{ pA}$) after incorporation into the silica surface, each at three different bias voltages. Pd reaches the maximum of the conductance at $U_B = + 2.2 \text{ V}$. For Ag, the maximum is with $U_B = + 2.0 \text{ V}$ at a slightly lower energy. No features were observed for spectroscopy at negative bias voltages. For color code see appendix

for three positive bias voltages. All maps are contrast-adjusted and cover the same dI/dV signal range¹². Equally for both metals, no significant electronic features were observed at negative bias voltages. The series for Pd starts at $U_B = 0.5 \text{ V}$ and appears to be electronically flat, indicating that the conductance is a function of the oxide film and the underlying support alone. With increasing voltage (1.3 V) several sections begin to stand out and continue to increase in contrast until they reach a pronounced contrast maximum at 2.2 V. This phenomenon is attributed to an unoccupied state of the Pd at this energy. A similar bias progression was applied to a sample with Ag adsorbates. At the starting point of $U_B = 1.0 \text{ V}$ the conductance appears featureless. Raising the bias voltage causes a raise at exactly those positions of the silica film that host the Ag atoms. The contrast peaks at 2.0 V and is, likewise Pd, associated with an unoccupied state of the Ag.

An in-depth analysis of the electronic features was done on the basis of model

¹²Since conductance maps measure relative changes of the conductivity the reference scale is taken from the map with the largest signal range, in this case Ag at 2.0 V.

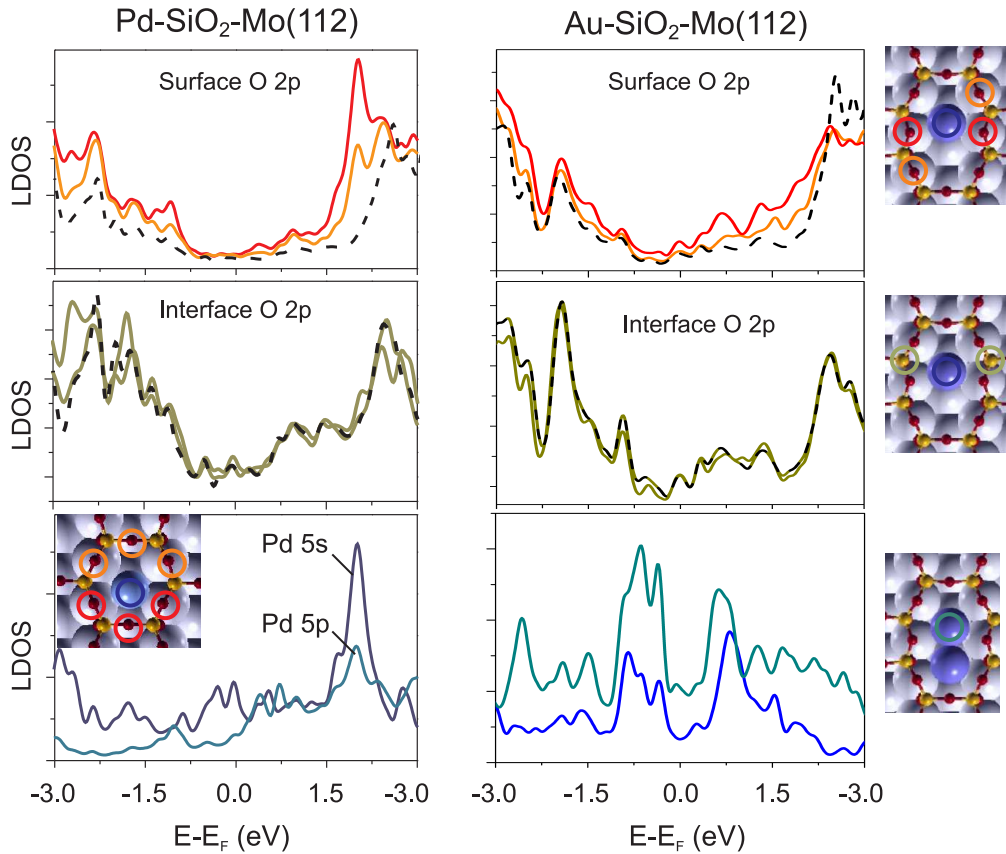


Figure 5.17 DFT calculations of the LDOS for the Pd-SiO₂-Mo(1 1 2) system (left) and the Au-SiO₂-Mo(1 1 2) system (right). Each series displays the LDOS layer by layer, starting with the results for the surface oxygen (top), followed by the interface oxygen (middle row) and the Mo-interface (bottom). The proximity of the surface O 2*p* states and the Pd 5*s* state result in a hybridization that leads to the characteristic contrast in STM images. The position of the Pd at the interface is shown in the insert. The scenario is very different for the Au species. The 6*s* states overlap very little with any of the oxide states which leads to a small hybridization that does not contribute significantly to the LDOS. The situation is the same for either a singly or doubly occupied oxide pore (lower right). The binding positions and the respective color-code are given in the upper two inserts for Au₁ and in the lower one for Au₂ species.

calculations. Fig. 5.17 shows DFT results for the LDOS of the individual silica levels with respect to Pd (left) and Au (right) adsorbates. Included are the depictions of the binding configurations that were considered for the computation. The Pd atom is placed in a two-fold bridge site at the SiO₂-Mo(112) interface. In this bridging geometry, the proximity of the LDOS of the interface oxygen and the Pd 5s orbital leads to a high probability for hybridization. More precise, the Pd 5s orbital hybridizes with the O 2p states of the six oxygen atoms that are positioned in the Pd-hosting –Si–O– ring. The availability of these Pd-induced states for tunneling is responsible for the star-like appearance of embedded Pd species in the STM images. It is only at higher bias voltages above + 2 V that the Pd 5s itself becomes directly accessible for tunneling electrons and the contrast localizes at the ring center (Fig. 5.12c and f).

The interaction of the incorporated Ag atoms (not shown) with the surrounding oxide film is similar. The largest change in the electronic structure is the formation of an O 2p-Ag 5s hybrid state with a maximum at $U_B = + 1.6$ eV and an extension towards lower energies down to the Fermi level (compare Fig. 5.19). Electron tunneling into this tail produces the star-like appearance in the topography, reflecting the increased LDOS of the six oxygen atoms of the hosting silica ring (Fig. 5.13).

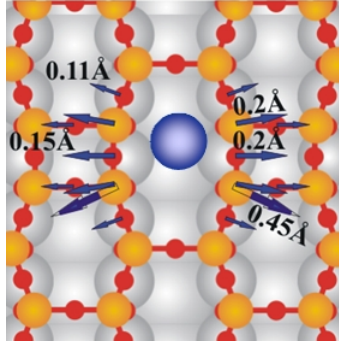


Figure 5.18 Incorporation of Au into the defective oxide opening. The –Si–O– octagon is widened by a reduced hybridization of the Si and O states, which leads to the characteristic contrast in STM. The computed rearrangement of the individual atoms upon Au adsorption is indicated in the image.

From an electronic point of view, the Au atoms bound to APDBs behave differently than their Pd and Ag counterparts. The Au 6s orbital strongly couples to the Mo *d*-states that lie in the region of the oxide band-gap, while hybridization with states of the oxide itself is negligible due to the large energy mismatch. Whereas the Pd and Ag induced states have a substantial density probability even above the oxide surface, the Au 6s-derived states are localized at the molybdenum-silica interface and consequently not accessible by CM or STS. The imaging contrast of Au atoms hosted inside of APDB results mostly from a structural distortion of the silica lattice. Upon Au incorporation the octagon widens which is accompanied by a reduced hybridization within the oxide itself (Fig. 5.18).

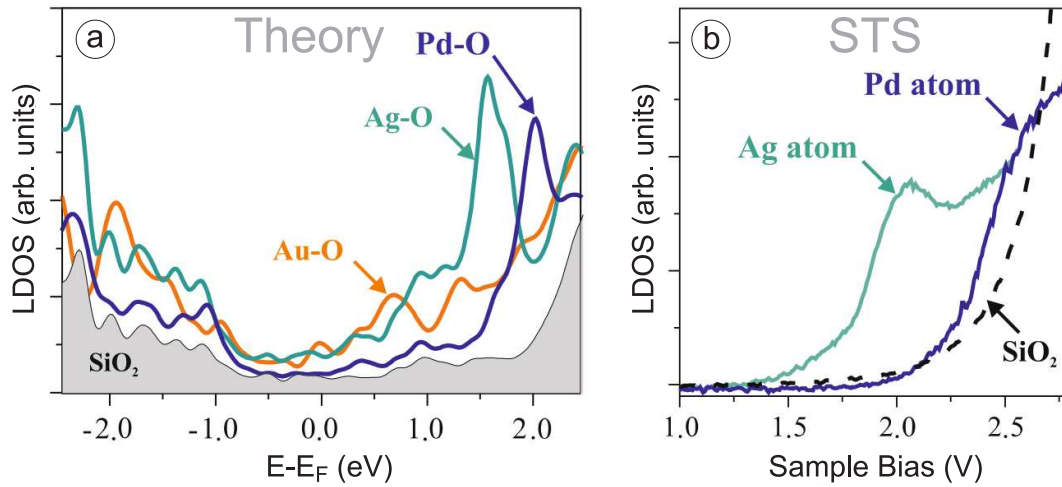


Figure 5.19 (a) Calculated LDOS of the pristine silica film (gray) and of the hybrid states formed between the respective s -orbitals of incorporated Pd, Ag and Au atoms and the O $2p$ states of the surface oxygen. (b) Tunneling spectroscopy performed in the energy range between 1.0 eV and 3.1 eV, showing the dI/dV spectra of the pristine oxide film and the states resulting from Pd and Ag insertion. The Pd-induced state appears less pronounced due to the increased LDOS of the silica-film itself.

The observations of Fig. 5.16 are also reflected in the STS measurements and the respective model calculations. Figure 5.19a depicts the calculated total LDOS of the pristine film (lower region, gray) and the hybrid states that form between s -orbitals of incorporated Pd, Ag and Au atoms and O $2p$ states of the surface oxygen atoms. The correlating experimental dI/dV data is shown in Fig. 5.19b for the pristine silica film (dashed) and at the adsorption sites of Pd and Ag atoms¹³. The peaks are less pronounced in the spectroscopic measurements since the features are not discriminated from the LDOS of the $\text{SiO}_2\text{-Mo}(1\ 1\ 2)$ complex.

¹³No meaningful data could be acquired for Au, though it was attempted to identify the potential unoccupied state at positive bias voltages and especially the occupied state of Au_1 at negative U_B

5.4 Creating Anchoring Sites for Metal Atoms on the Silica Film

The functionalization of an oxide surface is not limited to the selective adsorption properties that were observed for three elements in the previous section (Sec. 5.3). Even more interesting is the formation of adsorption complexes that create functional centers on top of the surface. Other than ad-atoms that bind to the oxide/metal-support interface, the stabilization of single atoms or small aggregates in an exposed position allows reactants that approach the surface to interact with them. The combination of an inert oxide surface with small reactive centers might allow for the creation of surfaces with entirely new and well controlled properties.

The experiments regarding the adsorption properties of metal atoms on the silica film have shown that between the three elements that were investigated, Pd has the lowest penetration barrier and binds strongest to the interface. In a different set of experiments performed with higher flux rates Pd was found to anchor strongly to the $\text{SiO}_2/\text{Mo}(112)$ interface even at temperatures as high as 300 K [174]. This motivated the attempt to create adsorption systems by inserting well defined binding sites into the otherwise inert oxide surface. The approach is similar to doping of oxide materials with impurities or point defects as a way to create potential binding sites. Ref. [143, 145, 175–177] reported significant changes of the adsorption behavior for Lithium- and Titanium- doped SiO_2 and MgO films containing oxygen vacancies. Doping, however, changes the chemical and electronic properties of an oxide film at a broader scale. In comparison, the insertion of single-atom anchors alters the binding characteristics only locally. In the following, experimental results are presented together with model calculations done by Martinez et al. [178] that describe the binding of single metal atoms to the silica film via Pd anchors.

None of the elements that were probed previously has a considerable binding strength atop the silica surface. Though Pd could theoretically remain outside the pores, it was not observed in such position with STM. This makes Pd, Ag and Au good candidates for the following investigations. Each set of experiments started out with the exposure of a cold sample ($T = 9.5$ K) to the Pd source to deposit approximately $1\text{--}3 \times 10^{13}$ atoms/cm². The successful incorporation of the Pd atoms into the film was verified by STM before either Pd, Ag or Au were deposited in an additional step¹⁴. The identification was easy, since Pd atoms appear as bright protrusions with a distinct, star-like shape at positive bias voltages above 1 V. The contrast which originates from hybridization between the Pd 5s and the O 2p states when Pd atoms have penetrated the silica micro-pores provides proof for a binding position at the $\text{SiO}_2/\text{Mo}(112)$ interface as described in Sec. 5.3. Those sub-surface Pd adsorbates are referred to as Pd_{sub} in the following.

Fig. 5.20 shows topographic images of consecutively deposited Pd–Pd, Pd–Ag and

¹⁴The experimental setup and conditions were the same as described in Sec. 5.3.

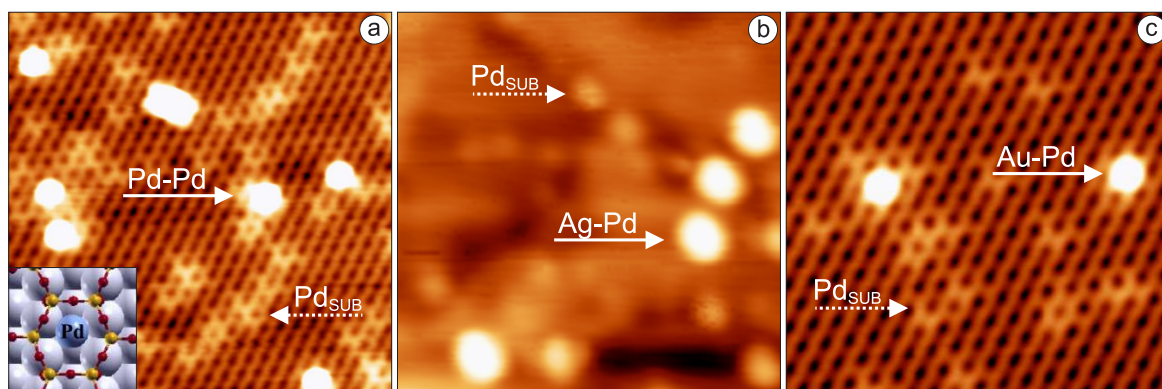


Figure 5.20 Topographic images of SiO₂/Mo(112) after successive deposition of Pd and (a) Pd, 14 x 14 nm², U_B = + 550 mV, I_T = 26 pA, (b) Ag, 20 x 20 nm², U_B = + 3390 mV, I_T = 33 pA, (c) Au, 10 x 10 nm², U_B = - 325 mV, I_T = 34 pA. For each case new features become visible, marked by arrows, that differ significantly from the deposition of a single element only. The insert in (a) shows the model of the initial Pd incorporation.

Pd–Au after the completion of both steps. In all three cases new features appear, which distinctively differ from the Pd anchors in height and shape. By taking the Pd_{sub} as reference, the density of Pd was determined to be about 15–20%, while this percentage for Ag and Au was with 8–10% much smaller.

The bias dependence of the corrugation differs appreciable from the anchor's contrast. Already at lower bias voltages, the new features display a significant height and a circular shape, while the incorporated Pd atoms have very little contrast to the silica film (Fig. 5.20). The comparison with Fig. 5.11 shows that the new species are not compatible with single Ag or Au atoms either. This is supported by DFT calculations finding that both species interact only weakly with the oxide film¹⁵ and rapidly diffuse even at low temperatures [145, 146]. As was shown in Sec. 5.3, Ag atoms are able to pass through the pores formed by the –Si–O– hexagons, resulting in an appearance similar to Pd_{sub} species, while Au atoms are too large to penetrate and hence exclusively bind at the larger openings that form at domain boundaries. Neither of those characteristics are found for the new species. It is especially well illustrated for the case of Pd–Au, where the resolution of the silica film allows to proof the absence of any APDB (Fig. 5.20c). Accordingly, the adsorbates that occur after Pd–Pd, Pd–Ag and Pd–Au deposition can be discriminated from individual Pd, Ag and Au atoms with certainty.

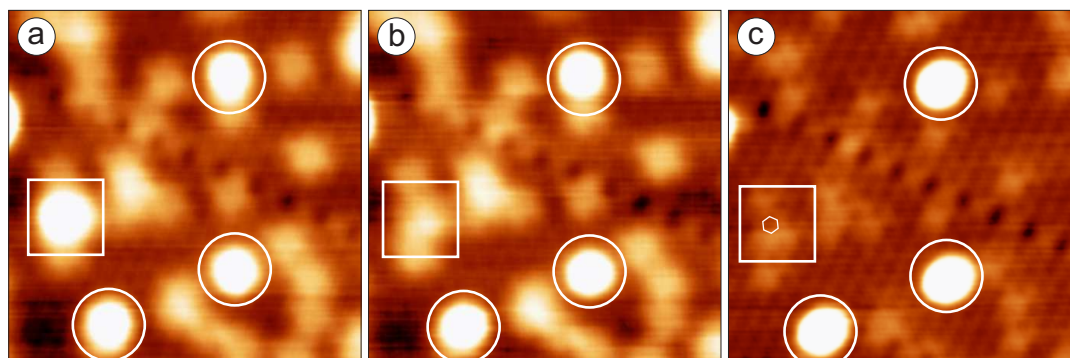


Figure 5.21 Dissociation of a Pd-Pd dimer by a voltage pulse applied with the STM tip. (a) Initial topography, displaying four Pd dimers. $10 \times 10 \text{ nm}^2$, $U_B = +1360 \text{ mV}$, $I_T = 31 \text{ pA}$. (b) The same surface section after application of $U_B = +4.5 \text{ V}$ for 10 ms to the feature marked by the square. The dimer disappeared, and an area with several embedded Pd appears. (c) The same image taken at a lower bias voltage (+ 1010 mV). The reduced contrast allows to pinpoint the adsorption site which is evidently on top of a Pd_{sub} .

Identification of the Adsorption Site

The localized nature of the alteration in the electronic structure of the silica by the Pd anchors makes it likely that the attachment of atomic species to the $\text{SiO}_2/\text{Mo}(112)$ surface is directly linked to the Pd_{sub} . To find further evidence for this hypothesis, it was attempted to identify the exact adsorption site of the new ad-species. Fig. 5.21 depicts a series of images that were taken after consecutive Pd-Pd deposition. Initially, four new features are present in the topography (Fig. 5.21a). Next, the STM tip was positioned right above the feature that is labeled by a square and exposed to a voltage pulse of $\simeq +5 \text{ V}$ for 10 ms. After the manipulation, the protrusion has disappeared (Fig. 5.21b). By lowering the bias voltage the characteristic signature of embedded Pd_{sub} becomes visible. Evidently the procedure removed the ad-species without any impact on the surroundings (Fig. 5.21c), indicating that the anchoring is indeed paramount to the stabilization of ad-atoms on the surface.

Electronic Properties of the Ad-Species

To further characterize the properties of the ad-species, changes of the LDOS were probed locally by tunneling spectroscopy (dI/dV)¹⁶. Figure 5.22b displays the dI/dV response of the Pd and Au ad-atoms. The Ag species could not be measured reliably

¹⁵Adsorption energies are around 50 meV.

¹⁶The lock-in settings for all measurements were 10 mV RMS modulation at 1137 Hz. A prime was chosen to minimize the chance for higher harmonics occurring as artifacts.

due to a quick desorption even at moderate current levels of a few pA¹⁷. Embedded Pd_{sub}-atoms are easily distinguishable from the silica film due to an increased local conductance at +2.3 eV [146]. The results for the Pd-Pd_{sub} compounds are considerably different. The local maximum related to an unoccupied state formed by hybridization of the Pd 5s and the silica surface oxygen has vanished. Instead, a new state occurs at lower energies that now lies at +1.75 eV. The change for the case of Pd-Au adsorption is even more significant. While no changes in the LDOS were measurable for Au atoms when directly deposited into the domain boundaries of the silica film, the pre-deposition of Pd not only leads to ad-species apart from domain boundaries but also to a feature in the dI/dV spectrum. The conductance peak of an unoccupied state is energetically located above the ones for Pd-Pd_{sub} and lies at 1.9 eV.

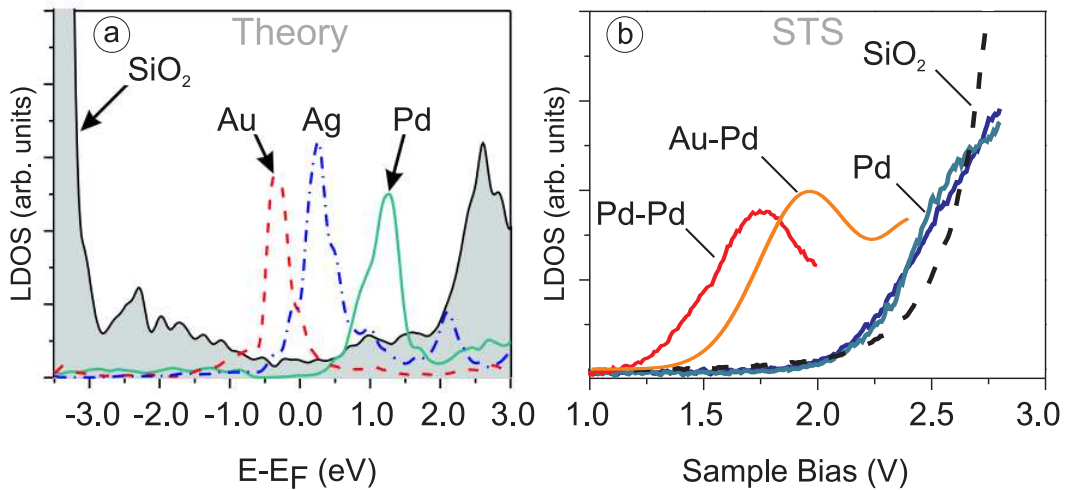


Figure 5.22 (a) Calculated LDOS of the pristine silica film (gray) and the respective dimers (colored lines). The spectra depict the contribution of the Au 6s (red), the Ag 5s (blue) and the Pd 5s (green) to the hybrid state that forms with the O 2p orbitals, when the respective ad-atom binds to the Pd_{sub}-anchor. (b) Spectroscopic results for the energy range between 1.0 - 2.8 eV, showing dI/dV spectra of a Pd-Pd_{sub} complex (red), an Au-Pd_{sub} complex (orange), the Pd_{sub} anchors (blue/green) and the plain oxide film (dashed line)

The formation of Pd/Ag/Au-Pd_{sub} dimers was supported by DFT calculations performed by the group of G. Pacchioni (Fig. 5.22a). The calculations were carried out with the generalized gradient approximation using the PW91 exchange-correlation functional and a plane wave basis set as implemented in the VASP code, with an energy cutoff at 400eV [166, 167]. The electron-ion interaction was included by the projector-augmented-wave method [168]. The Mo (112) substrate was described by

¹⁷The preliminary data indicates an unoccupied state at approx. +3.6 eV

seven Mo layers, whereby the three bottom layers were a priori static in their bulk positions during geometry optimization. The silica film was modeled with (4 x 2) and (6 x 4) super-cells corresponding to a stoichiometry of $\text{Mo}_{14}\text{Si}_2\text{O}_5$ and $\text{Mo}_{24}\text{Si}_6\text{O}_{15}$, respectively [169]. The modeling was able to verify the formation of covalent bonds between the ad-atoms and Pd_{sub} which are placed inside the oxide pores.

There is a noticeable difference between the calculated and the measured positions of the electronic dimer-states. The theory finds the Pd-Pd_{sub} dimer state to have with $\approx +1.2$ eV the highest energy, the Ag-Pd_{sub} dimer state lies about 1 eV below and the occupied Au-Pd_{sub} state lies 0.5 eV below E_F (Fig. 5.22a). A conclusive interpretation of this discrepancy is lacking. A potential explanation might be found in the spatial extension of the electronic states (see next section) which could be responsible for domination of the STS signal by the (shifting) Pd_{sub} LDOS.

The binding energies are substantially different for each of the three species. The strongest interaction was found for Pd ad-atoms, which bind with 1.16 eV to the Pd_{sub}. The bond length amounts to 2.66 Å. Without the presence of a surface anchor, the binding strength decreases to 0.35 eV and the atoms spontaneously penetrate the holes inside of the –Si–O– hexagons. The adsorption energies of the noble-metal atoms are considerably smaller with values of 0.19 eV for Ag-Pd_{sub} and of 0.35 eV for Au-Pd_{sub} complexes. The weak binding of Ag-Pd_{sub} might be responsible for the electron-induced desorption during STS experiments. The inter-atomic bond lengths are with 2.85 Å for Ag-Pd_{sub} and 2.54 Å for Au-Pd_{sub} surprisingly similar to the Pd-Pd_{sub} units and even close to the values of the corresponding gas-phase dimers (Pd-Pd 2.54 Å, Au-Pd 2.68 Å).

The short inter-atomic distances of the dimer-components would have indicated higher binding energies than the ones calculated with DFT. Apparently, the dimer configurations on the silica surface are resulting from two competing interaction mechanisms. On one hand the ad-atoms are forming strong, covalent bonds with the Pd_{sub} anchors. On the other hand this attractive component is counterbalanced by the Pauli repulsion that is exerted on the ad-atoms mainly by the filled 2*p* states of the surface oxygen. The repulsion is governed by the spatially most extended atomic orbital, which is the 5*s* in case of Pd and Ag and the 6*s* in case of Au. Those frontier orbitals hybridize with the O 2*p* states upon adsorption, forming new states with anti-bonding character (Fig. 5.22a). The strength of the repulsion and respectively the ad-atom-surface interaction is now controlled by the number of electrons filling these hybrid states.

The Pd_{top} 5*s*–O 2*p* hybrid state is located at +1.25 eV above the Fermi level (E_F) and therefore empty, which reduces the repulsion from the oxygen states and allows the formation of strong Pd-Pd_{sub} bonds. The binding energy is even higher than for the gas phase Pd₂ dimer, reflecting the stabilization effect of the Mo support. The position of the Pd_{top} 5*s*-derived state above E_F manifests the charge neutrality of the ad-atom in equivalence to the gas-phase situation. The difference between the measured hybrid state peaking at +1.75 V in the dI/dV experiments (Fig. 5.22b) and

the calculated value of +1.25 eV is small enough to support the proposed mechanism.

The hybrid state formed between the Ag_{top} 5s orbital and the O 2s states is located at + 0.1 eV and therefore singly occupied. In contrast, the same state forged between the Au_{top} 6s orbital and the O 2p states is doubly occupied, as deduced from the calculated energy position of - 0.3 eV. (Fig. 5.22a). Neither one of these states could be identified within dI/dV-spectra, potentially because of the vicinity to E_F . We note however, that the enhanced signal in the conductance map of Au-Pd_{sub} complexes around - 0.2 eV might indicate tunneling into the Au 6s state (Fig. 5.24). The electrons in the noble-metal–oxygen states induce substantial Pauli repulsion with the silica LDOS, which partially compensates the attractive interaction with the Pd_{sub} anchors and leads to the small net-binding energies of Ag and Au atoms. The effect is more pronounced for Au because its valence s-orbital is doubly occupied ($6s^2$ configuration) as a result of charge transfer from the Mo support. The formation of anionic Au species has been observed for other oxide films too, and underscores the strong electronegative character of gold [18,172]. On the contrary, the Ag ad-atoms remain charge-neutral on the silica surface since their 5s orbitals carry only a single electron similar to Ag in the gas-phase. The occurrence of comparable adsorption energies for Ag and Au atoms, in spite of different repulsive terms, can be explained by the balancing influence of the metal *d*-states. While the Au 5*d*-states strengthen the Au-Pd_{sub} interaction considerably, the Ag 4*d*-states are too low in energy to participate in the bond formation.

Spatial Extension of the Electronic States

Besides the nature of the local electronic structure, its spatial extension and the differences to the supporting silica film are of relevance. This information can be accessed with scanning conductance mapping (CM). Figure 5.23 shows a topographic image as reference and CM of the Pd-Pd_{sub} dimers for three different energies. At a bias voltage of -0.5 V, the features are easily visible in the topography (Fig. 5.23a). On the contrary, the differential conductance is almost featureless for negative bias and positive voltages up to 1.2 V (Fig. 5.23/1.2 V). As the energy increases the conduction in the region of the dimers becomes larger. It is noteworthy, though, that at an energy of + 1.6 eV most of the electronic contrast is concentrated at the edge of the feature with a negligible change within the center area. Compared to the atomic structure of the underlying silica film the spatial extension of this electronic state appears to be too extended to be a feature of the adsorbate only (Fig. 5.23/1.6 V). When U_B reaches at 1.8 V the value of the feature in STS, the conductance map displays a strong maximum with most of the conductance related contrast centered on the dimers.

The spatial distribution of the electronic states for the Au-Pd_{sub} is even more remarkable in its appearance. A complete series of conductance maps ranging from $U_B = -0.4$ V to + 2.2 V is shown in Figure 5.24. The first image at the upper left corner shows a topographic image that serves as reference. It contains two different features,

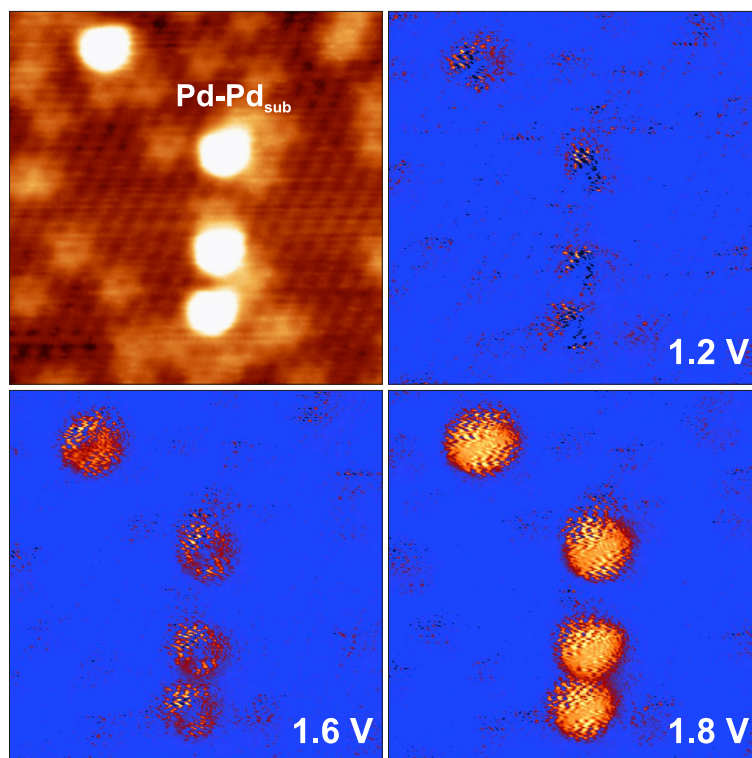


Figure 5.23 Topography and conductance map series of a Pd-Pd_{sub} complex. The topography is shown at the upper left corner (10 x 10 nm², U_B = - 500 mV, I_T = 32 pA). The conductance maps show an increase in the corona region of the feature between 1.4 V and 1.6 V and a pronounced maximum at \approx 1.8 V.

one Au-Pd_{sub} dimer indicated by the square frame and one Pd_{sub} atom in their typical configuration. Starting at -0.4 V, the conductance is low and barely distinguishable from the background. At -0.3 V the current through the dimer is substantially increased in a confined area in the center region, much smaller than the topographic appearance. With increasing bias voltage, the conductance vanishes until at approx. 1.3 V a ring-like corona appears. In a range of approx. 0.2 V the highest dI/dV signal is found within this area (Fig. 5.24 middle row). At 1.8 V the dimer appears at full brightness while the conductance of the single Pd_{sub} just starts to increase. At the end of the series, the single Pd atom displays the already known conductance maximum at 2.2 V, but the differential conductance of the dimer has vanished. In the CM the previous protrusion now appears as depression, a phenomenon that typically appears after a local maximum of the conductance has been exceeded (Fig 5.24, last image).

Evidently the different ad-species exhibit dI/dV characteristics that distinctively deviate from the spectroscopic identity of the inserted single atoms. The dimer formation on the silica surface is obviously the result of a tight interaction between electronic

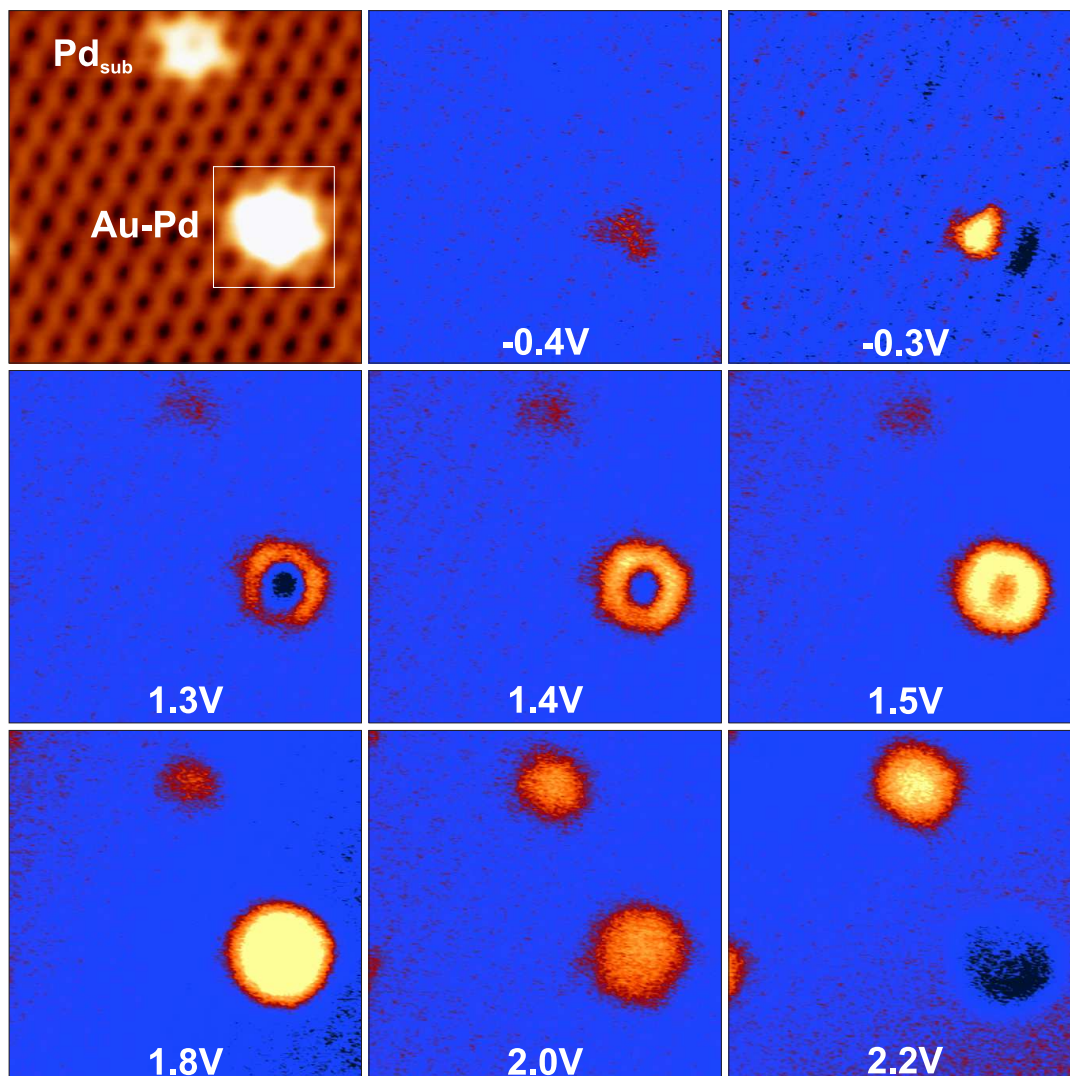


Figure 5.24 Topography and conductance map series of an Au-Pd_{sub} complex. The topography is shown at the upper left corner (6 x 6 nm², U_B = + 1210 mV, I_T = 35 pA). In addition to the Au-Pd_{sub} feature, the presence of a Pd_{sub} is indicated to serve as reference. The conductance maps present the most significant changes in the range from -0.4 V to + 2.2 V. The increase of the conductance at -0.3 V and + 1.6 V in the center region of the Au feature denotes the occurrence of two intrinsic states, while the ring-like conductance enhancement between \approx 1.0 V and 1.5 V originates from the widening of the oxide pore upon Au adsorption.

states of the ad-atoms, the Pd_{sub} anchors, the silica film and the Mo support. Respectively, the bonds within the dimer-surrounding silica film respond to the new situation. Upon ad-atom attachment the –Si–O– hexagons that host the Pd_{sub} relax to reduce the steric repulsion. The effect is most pronounced for the Au-Pd_{sub} dimers due to the double occupancy of the Au 6s-O 2p hybrid state.

According to DFT calculations, the opening of a –Si–O– hexagon enlarges by several tenths of an Å ($\approx 5\%$) and thus enables the Au to approach the Pd_{sub} anchor. As a result the Au binding energy increases from 0.14 eV for a static geometry to 0.35 eV after the structural relaxation. The widening of the ring is accompanied by a reduction of the silica LDOS in proximity to the Au-Pd_{sub} binding site, which reflects the decreased Si-O orbital overlap within the enlarged hexagon. In response to the outward relaxation of the hexagon, the surrounding film region has to be compressed. This variation of the density of states is most likely the underlying mechanism for the ring-like conductance feature that occurs between 1.2 V and 1.5 V in the dI/dV maps (Fig. 5.24). While the center of the ring exhibits a reduced LDOS (darker) the corona region displays an increased LDOS (lighter). The ring diameter is approx. 10 Å, indicating that mainly the immediate neighbors outside the filled nano-pore are affected by the compressive stress. Albeit less pronounced, the same pattern can be seen in the conductance map of the Pd-Pd_{sub} dimer (Fig. 5.23, 1.6 V).

5.5 Conclusions

Based on the here presented results, the possibility to functionalize the ultra-thin silica film was unambiguously illustrated. The oxide surface acts like an atomic sieve with a distinct, material-specific interaction. It was shown that the probability for penetrating the thin silica film is primarily dependent on the extension of the electron orbitals and not on the size of an atom given by its van-der-Waals radius. A pre-doped film changes the adsorption properties significantly. By inserting Pd atoms into the film, adsorption anchors are created that can stabilize additional ad-atoms on the SiO₂/Mo(112) surface in a way that is not possible without those anchors.

This work lays the foundation for a new approach to utilize an oxide film grown on a crystalline metal substrate. Future studies should focus on alterations of the main functional elements: (i) The film thickness. So far the crystalline form of the silica film could be obtained as a mono-layer only. Thicker films grow amorphous on Mo(112) and therefore lose the aspired properties. (ii) The element type of the adsorbates should be expanded. Of particular interest are alkali metals due to their expectedly strong interaction at the support-oxide interface accompanied by a change of the work function. (iii) The amount of Au that can be stabilized on the Pd pre-doped surface needs to be determined. (iv) The occurrence and frequency of APDB can potentially be manipulated or even eliminated by introducing a stepped metal substrate.

At the time of these writings, further experiments were already successfully per-

formed. Löffler et al. have been able to grow a double-layer SiO₂ on a Ru(0001) support [179]. The film is formed by two layers of corner-sharing SiO₄ tetrahedron bonded together by oxygen bridges. The plane that contains the intermediate oxygen constitutes a symmetry plane that literally mirrors the congruent monolayers. The SiO₂ binds only weakly to the substrate in two possible orientations dependent on the oxygen amount at the Ru surface. The hexagonal Si arrangement results in openings that potentially give access to the SiO₂/Ru(0001) interface but adsorption experiments regarding this system have not been published yet.

Jerratsch et al. have conducted adsorption experiments with Li and Fe on a SiO₂-Mo(112) surface. It was shown that Li atoms are able to penetrate the oxide layer and bind in two distinct configurations at the metal-oxide interface [162,180]. Upon adsorption, Li⁺ cations are formed that induce a positive surface dipole which reduces the work function of the silica film. The work function decrease is accompanied by a down-shift of the silica conduction band. Li-doped silica is suitable for the adsorption of electronegative species like Au⁻, as the reduced work function promotes charge-transfer out of the film.

The ultra-thin SiO₂/Mo(112) film is also capable of stabilizing monomeric Fe in a two-dimensional array [181]. The Fe atoms penetrate the openings in the silica surface and bind strongly to the metal-oxide interface. Once adsorbed, the diffusion and agglomeration is inhibited at temperatures as high as 300K and above. The magnetic character of the interfacial Fe atoms is preserved and leads to the formation of a hybrid state between the localized Fe 3d states that carry the magnetic moment and the sp-state continuum of the Mo. This Kondo-resonance is located at the Fermi level and gives rise to a distinct Fano-type conductance spectra which was indeed measured with STS.

Bibliography

- [1] Ertl, G. & Rau, P. Chemisorption and catalytic reactions of oxygen and carbon monoxide on palladium (110). *Surf. Sci.* **15**, 443 (1969).
- [2] Kahn, D. R., Petersen, E. E. & Somorjai, G. A. Hydrogenolysis of cyclopropane on a platinum stepped single crystal at atmospheric pressure. *J. Catal.* **34**, 294 (1974).
- [3] Christmann, K., Ertl, G. & Pignet, T. Adsorption of hydrogen on a Pt(111) surface. *Surf. Sci.* **54**, 365 (1976).
- [4] Diebold, U. The surface science of titanium dioxide. *Surf. Sci. Rep.* **48**, 53 (2003).
- [5] Jaeger, R. *et al.* Formation of a well-ordered aluminum oxide overlayer by oxidation of NiAl(110). *Surf. Sci.* **259**, 235 (1991).
- [6] Schintke, S. & Schneider, W. Insulators at the ultrathin limit: electronic structure studied by scanning tunneling microscopy and spectroscopy. *J. Phys.: Condens. Matter* **16**, R49 (2004).
- [7] He, J.-W., Xu, X., Corneille, J. & Goodman, D. X-ray photoelectron spectroscopic characterization of ultra-thin silicon oxide films on a Mo(100) surface. *Surf. Sci.* **279**, 119 (1992).
- [8] Henry, C. Surface studies of supported model catalysts. *Surf. Sci. Rep.* **31**, 231 (1998).
- [9] Freund, H.-J. *et al.* Bridging the pressure and material gaps between catalysis and surface science: clean and modified oxide surfaces. *Top. Catal.* **15**, 201 (2001).
- [10] Freund, H.-J. Models for oxidation catalysts: Characterization and reaction at the atomic level. *Catal. Today* **117**, 6 (2006).
- [11] Freund, H.-J. & Goodman, D. *Handbook of Heterogeneous Catalysis* (WILEY-VCH Verlag, 2008).
- [12] Freund, H.-J. Metal-supported ultrathin oxide film systems as designable catalysts and catalyst supports. *Surf. Sci.* **601**, 1438 (2007).

- [13] Nilius, N., Rienks, E., Rust, H.-P. & Freund, H.-J. Self-Organization of Gold Atoms on a Polar FeO(111) Surface. *Phys. Rev. Lett.* **95**, 066101 (2005).
- [14] Libuda, J. *et al.* Structure and defects of an ordered alumina film on NiAl(110). *Surf. Sci.* **318**, 61 (1994).
- [15] Bäumer, M. & Freund, H.-J. Metal deposits on well-ordered oxide films. *Prog. Surf. Sci.* **61**, 127 (1999).
- [16] Kulawik, M., Nilius, N. & Freund, H.-J. Influence of the Metal Substrate on the Adsorption Properties of Thin Oxide Layers: Au Atoms on a Thin Alumina Film on NiAl(110). *Phys. Rev. Lett.* **96**, 036103 (2006).
- [17] Freund, H.-J. & Pacchioni, G. Oxide ultra-thin films on metals: new materials for the design of supported metal catalysts. *Chem. Soc. Rev.* **37**, 2224 (2008).
- [18] Sterrer, M. *et al.* Control of the Charge State of Metal Atoms on Thin MgO Films. *Phys. Rev. Lett.* **98**, 096107 (2007).
- [19] Cho, A. Connecting the Dots to Custom Catalysis. *Science* **299**, 1684 (2003).
- [20] Schalow, T. *et al.* Oxygen Storage at the Metal/Oxide Interface of Catalyst Nanoparticles. *Angew. Chem. Int. Ed.* **44**, 7601 (2005).
- [21] Jaklevic, R. & Lambe, J. Molecular Vibration Spectra by Electron Tunneling. *Phys. Rev. Lett.* **22**, 1139 (1966).
- [22] Khanna, S. & Lambe, J. Inelastic Electron Tunneling Spectroscopy. *Science* **220**, 1345 (1983).
- [23] Binnig, G., Garcia, N. & Rohrer, H. Conductivity sensitivity of inelastic scanning tunneling microscopy. *Phys. Rev. B* **32**, 1336 (1985).
- [24] Stipe, B., Rezaei, M. & Ho, W. Single-Molecule Vibrational Spectroscopy and Microscopy. *Science* **280**, 1732 (1998).
- [25] Lauhon, L. & Ho, W. Single-molecule vibrational spectroscopy and microscopy: CO on Cu(001) and Cu(110). *Phys. Rev. B* **60**, R8525 (1999).
- [26] Hahn, J., Lee, H. & Ho, W. Electronic Resonance and Symmetry in Single-Molecule Inelastic Electron Tunneling. *Phys. Rev. Lett.* **85**, 1914 (2000).
- [27] Wallis, T., Chen, X. & Ho, W. Single molecule vibrational spectroscopy and microscopy: Cu(II) etioporphyrin-I on Cu(001). *J. Chem. Phys.* **113**, 4837 (2000).

-
- [28] Lee, H. & Ho, W. Single-Bond Formation and Characterization with a Scanning Tunneling Microscope. *Science* **286**, 1719 (1999).
- [29] Lee, H. & Ho, W. Structural determination by single-molecule vibrational spectroscopy and microscopy: Contrast between copper and iron carbonyls. *Phys. Rev. B* **61**, R16347 (2000).
- [30] Nilius, N., Wallis, T. & Ho, W. Vibrational spectroscopy and imaging of single molecules: Bonding of CO to single palladium atoms on NiAl(110). *J. Chem. Phys.* **117**, 10947 (2002).
- [31] Wallis, T., Nilius, N. & Ho, W. Single molecule vibrational and electronic analyses of the formation of inorganic complexes: CO bonding to Au and Ag atoms on NiAl(110). *J. Chem. Phys.* **119**, 2296 (2003).
- [32] Gawronski, H., Mehlhorn, M. & Morgenstern, K. Imaging Phonon Excitation with Atomic Resolution. *Science* **319**, 930 (2008).
- [33] Tsuji, K., Hasegawa, Y., Wagatsuma, K. & Sakurai, T. Detection of X-ray Induced Current Using a Scanning Tunneling Microscope and its Spatial Mapping for Elemental Analysis. *Jpn. J. Appl. Phys.* **37**, L1271 (1998).
- [34] Hasegawa, Y., Tsuji, K., Wagatsuma, K. & Sakurai, T. X-ray source combined ultrahigh-vacuum scanning tunneling microscopy for elemental analysis. *J. Vac. Sci. Technol. B* **18**, 2676 (2000).
- [35] Matsushima, T. *et al.* Development and trial measurement of a synchrotron-radiation-light-illuminated scanning tunneling microscope. *Rev. Sci. Instrum.* **75**, 2149 (2004).
- [36] Reihl, B. & Gimzewski, J. Field Emission Scanning Auger Microscope. *Surf. Sci.* **189/190**, 39 (1987).
- [37] Palmer, R., Eves, B., Festy, F. & Svenson, K. Scanning probe energy loss spectroscopy. *Surf. Sci.* **502-503**, 224 (2002).
- [38] Coombs, J., Gimzewski, J., Reihl, B., Sass, J. & Schlitter, R. Photon emission experiments with the scanning tunneling microscope. *J. Microsc.* **152**, 325 (1988).
- [39] Gimzewski, J., Reihl, B., Coombs, J. & Schlitter, R. Photon emission with the scanning tunneling microscope. *Z. Phys. B* **72**, 497 (1988).
- [40] Berndt, R. *et al.* Photon Emission at Molecular Resolution Induced by a Scanning Tunneling Microscope. *Science* **262**, 1425 (1993).

- [41] Nilius, N. *Lichtemission aus einzelnen, oxidgetragenen Metallpartikeln im Rastertunnelmikroskop*. Ph.D. thesis, Humboldt-Universität zu Berlin (2001).
- [42] Young, R., Ward, J. & Scire, F. Observation of Metal-Vacuum-Metal Tunneling, Field Emission, and the Transition Region. *Phys. Rev. Lett.* **27**, 922 (1971).
- [43] Young, R., Ward, J. & Scire, F. The Topographiner: An Instrument for Measuring Surface Microtopography. *Rev. Sci. Instrum.* **43**, 999 (1972).
- [44] Binnig, G., Rohrer, H., Gerber, C. & Weibel, E. Surface Studies by Scanning Tunneling Microscopy. *Phys. Rev. Lett.* **49**, 57 (1982).
- [45] Shantyr, R. *Scanning tunneling microscopy/spectroscopy on growth, atomic and electronic structure of Co oxide and Mn oxide films on Ag(001)*. Ph.D. thesis, Martin-Luther-Universität Halle-Wittenberg (2004).
- [46] Hamers, R., Tromp, R. & Demuth, J. Scanning tunneling microscopy of Si(001). *Phys. Rev. B* **34**, 5343 (1986).
- [47] Stroscio, J., Feenstra, R. & Fein, A. Electronic Structure of the Si(111)2x1 Surface by Scanning-Tunneling Microscopy. *Phys. Rev. Lett.* **57**, 2579 (1986).
- [48] Eigler, D. & Schweizer, E. Positioning single atoms with a scanning tunneling microscope. *Nature* **344**, 524 (1990).
- [49] Stroscio, J. & Eigler, D. Atomic and Molecular Manipulation with the Scanning Tunneling Microscope. *Science* **254**, 1319 (1991).
- [50] Bartels, L., Meyer, G., Meyer, K., Rieder, K.-H. Basic steps involved in the lateral manipulation of single CO molecules and rows of CO molecules. *Chem. Phys. Lett.* **273**, 371 (1997).
- [51] Bartels, L., Meyer, G. & Rieder, K.-H. Controlled vertical manipulation of single CO molecules with the scanning tunneling microscope: A route to chemical contrast. *Appl. Phys. Lett.* **71**, 231 (1997).
- [52] Wiesendanger, R., Guentherodt, H.-J., Guentherodt, G., Gambino, R. & Ruf, R. Observation of Vacuum Tunneling of Spin-Polarized Electrons with the Scanning Tunneling Microscope. *Phys. Rev. Lett.* **65**, 247 (1990).
- [53] Elrod, S., deLozanne, A. & Quate, C. Low-temperature vacuum tunneling microscopy. *Appl. Phys. Lett.* **45**, 1240 (1984).
- [54] Smith, D. & Binnig, G. Ultrasmall scanning tunneling microscope for use in a liquid-helium storage Dewar. *Rev. Sci. Instrum.* **57**, 2030 (1986).

-
- [55] Valden, M., Lai, X. & Goodman, D. Onset of Catalytic Activity of Gold Clusters on Titania with the Appearance of Nonmetallic Properties. *Science* **281**, 1647 (1998).
- [56] Freund, H.-J. Clusters and islands on oxides: from catalysis via electronics and magnetism to optics. *Surf. Sci.* **500**, 271 (2002).
- [57] Bardeen, J. Tunneling from a many-particle point of view. *Phys. Rev. Lett.* **6**, 57 (1961).
- [58] Tersoff, J. & Hamann, D. Theory and Application for the Scanning Tunneling Microscope. *Phys. Rev. Lett.* **50**, 1998 (1983).
- [59] Tersoff, J. & Hamann, D. Theory of the scanning tunneling microscope. *Phys. Rev. B* **31**, 805 (1985).
- [60] Chen, C. *Introduction to Scanning Tunneling Microscopy* (Oxford Science Publications, 2008).
- [61] Selloni, A., Carnevali, P., Tosatti, E. & Chen, D. Voltage-dependent scanning-tunneling microscopy of a crystal surface: Graphite. *Phys. Rev. B* **31**, 2602 (1985).
- [62] Feenstra, R., Stroscio, J. & Fein, A. Tunneling Spectroscopy of the Si(111)2x1 Surface. *Surf. Sci.* **181**, 295 (1987).
- [63] Lang, N. Spectroscopy of single atoms in the scanning tunneling microscope. *Phys. Rev. B* **34**, 5947 (1986).
- [64] Oelsen, L. *et al.* Apparent Barrier Height in Scanning Tunneling Microscopy Revisited. *Phys. Rev. Lett.* **76**, 1485 (1996).
- [65] Yoshikawa, J., Kurokawa, S. & Sakai, A. Barrier-height imaging of Cs-adsorbed Si(111). *Appl. Surf. Sci.* **169-170**, 202 (2001).
- [66] Rienks, E., Nilius, N., Rust, H.-P. & Freund, H.-J. Surface potential of a polar oxide film: FeO on Pt(111). *Phys. Rev. B* **71**, 241404 (2005).
- [67] Schuster, R., Barth, J., Wintterlin, J., Behm, R. & G, E. Distance dependence and corrugation in barrier-height measurements on metal surfaces. *Ultramicroscopy* **42-44**, 533 (1992).
- [68] Garcia, N. Theory of scanning tunneling microscopy and spectroscopy: Resolution, image and field states, and thin oxide layers. *IBM J. Res. Develop.* **30**, 533 (1986).

- [69] Gundlach, K. Zur Berechnung des Tunnelstroms durch eine trapezförmige Potentialstufe. *Solid. State Electron.* **9**, 949 (1966).
- [70] Coombs, J. & Gimzewski, J. Fine structure in field emission resonances at surfaces. *J. Microsc.* **152**, 841 (1988).
- [71] Persson, B. & Demuth, J. Inelastic Electron Tunneling from a Metal Tip. *Solid State Commun* **57**, 769 (1986).
- [72] Scalapino, D. & Marcus, S. Theory of Inelastic Electron-Molecule Interactions in Tunnel Junctions. *Phys. Rev. Lett.* **18**, 459 (1967).
- [73] Persson, B. & Baratoff, A. Inelastic Electron Tunneling from a Metal Tip: The Contribution from Resonant Processes. *Phys. Rev. Lett.* **59**, 339 (1987).
- [74] Gata, M. & Antoniewicz, P. Resonant tunneling through adsorbates in scanning tunneling microscopy. *Phys. Rev. B* **47**, 13797 (1993).
- [75] Nilius, N. *E6 Light emission spectroscopy with the STM* (Verlag, 2007).
- [76] Berndt, R. Photon Emission from the Scanning Tunneling Microscope. In Wiesendanger, R. (ed.) *Scanning Probe Microscopy: Analytical Methods* (Springer, 1998).
- [77] Persson, B. & Baratoff, A. Theory of Photon Emission in Electron Tunneling to Metallic Particles. *Phys. Rev. Lett.* **68**, 3224 (1992).
- [78] Berndt, R., Gimzewski, J. & Johansson, S. Electromagnetic interactions of metallic objects in nanometer proximity. *Phys. Rev. Lett.* **71**, 3493 (1993).
- [79] Johansson, P., Monreal, R. & Apell, P. Theory for light emission from a scanning tunneling microscope. *Phys. Rev. B* **42**, 9210 (1990).
- [80] Berndt, R., Gimzewski, J. & Johansson, P. Inelastic tunneling excitation of tip-induced plasmon modes on noble-metal surfaces. *Phys. Rev. Lett.* **67**, 3796 (1991).
- [81] Berndt, R. & Gimzewski, J. The role of proximity plasmon modes on noble metal surfaces in scanning tunneling microscopy. *Surf. Sci.* **269**, 556 (1992).
- [82] Downes, A. & Welland, M. Photon emission from Ag and Au clusters in the scanning tunneling microscope. *Appl. Phys. Lett.* **72**, 2671 (1998).
- [83] Nilius, N., Ernst, N. & Freund, H.-J. Photon Emission Spectroscopy of Individual Oxide-Supported Silver Clusters in a Scanning Tunneling Microscope. *Phys. Rev. Lett* **84**, 3994 (2000).

-
- [84] Alvarado, S. *et al.* Luminescence in scanning tunneling microscopy on III-V nanostructures. *J. Vac. Sci. Technol. B* **9**, 409 (1991).
- [85] Chizhov, I., Lee, G., Willis, R., Lubyshev, D. & Miller, D. Luminescence from GaAs(100) surface excited by a scanning tunneling microscope. *J. Vac. Sci. Technol. A* **15**, 1432 (1997).
- [86] Ortsiefer, M. *et al.* STM-excited and spectrally resolved luminescence of epitaxial GaN and AlGaN layers grown by MBE. *Appl. Phys. A* **66**, S371 (1998).
- [87] Qui, X., Nazin, G. & Ho, W. Vibrationally Resolved Fluorescence Excited with Submolecular Precision. *Science* **299**, 542 (2003).
- [88] Cavar, E. *et al.* Fluorescence and Phosphorescence from Individual C₆₀ Molecules Excited by Local Electron Tunneling. *Phys. Rev. Lett.* **95**, 196102 (2005).
- [89] Besocke, K. An easily operable Scanning Tunneling Microscope. *Surf. Sci.* **181**, 145 (1987).
- [90] Santra, A., Kolmakov, A., Yang, F. & Goodman, D. Growth of Au on TiO₂(110) on a Cluster-by-Cluster Basis. *Jpn. J. Appl. Phys.* **42**, 4795 (2003).
- [91] Schulz, R. & Rossel, C. Beetle-like scanning tunneling microscope for ultrahigh vacuum and low-temperature applications. *Rev. Sci. Instrum.* **65**, 1918 (1994).
- [92] Meyer, G. A simple low-temperature ultrahigh-vacuum scanning tunneling microscope capable of atomic manipulation. *Rev. Sci. Instrum.* **67**, 2960 (1996).
- [93] Stipe, B., Rezaei, M. & Ho, W. A variable-temperature scanning tunneling microscope capable of single-molecule vibrational spectroscopy. *Rev. Sci. Instrum.* **70**, 137 (1999).
- [94] Voigtländer, B., Zinner, A. & Weber, T. High temperature scanning tunneling microscopy during molecular beam epitaxy. *Rev. Sci. Instrum.* **67**, 2568 (1996).
- [95] Emundts, A. *et al.* Combination of a Besocke-type scanning tunneling microscope with a scanning electron microscope. *Rev. Sci. Instrum.* **72**, 3546 (2001).
- [96] Pertaya, N., Braun, K.-F. & Rieder, K.-H. On the stability of Besocke-type scanners. *Rev. Sci. Instrum.* **75**, 2608 (2004).
- [97] Park, S.-I. & Quate, C. Theories of the feedback and vibration isolation systems for the scanning tunneling microscope. *Rev. Sci. Instrum.* **58**, 2004 (1987).
- [98] Hansma, P. & Tersoff, J. Scanning tunneling microscopy. *J. Appl. Phys.* **61**, R1 (1987).

- [99] Test measurement Fa. Bilz (1998).
- [100] Ternes, M. *Scanning Tunneling Spectroscopy at the Single Atom Scale*. Ph.D. thesis, École Polytechnique Fédérale de Lausanne (2006).
- [101] Berndt, R. *et al.* Atomic Resolution in Photon Emission Induced by a Scanning Tunneling Microscope. *Phys. Rev. Lett.* **74**, 102 (1995).
- [102] Berndt, R., Schlitter, R. & Gimzewski, J. Photon emission scanning tunneling microscope. *J. Vac. Sci. Technol. B* **9**, 573 (1991).
- [103] Sakurai, M., Thirstrup, C. & Aono, M. Optical Selection Rules in Light Emission from the Scanning Tunneling Microscope. *Phys. Rev. Lett.* **93**, 046102 (2004).
- [104] Thirstrup, C., Sakurai, M., Stokbro, K. & Aono, M. Visible Light Emission from Atomic Scale Patterns Fabricated by the Scanning Tunneling Microscope. *Phys. Rev. Lett.* **82**, 1241 (1999).
- [105] Nilius, N., Cörper, A., Bozdech, G., Ernst, N. & Freund, H.-J. Experiments on individual alumina-supported adatoms and clusters. *Prog. Surf. Sci.* **69**, 99 (2001).
- [106] Hoffmann, G., Kröger, J. & Berndt, R. Color imaging with a low temperature scanning tunneling microscope. *Rev. Sci. Instrum.* **73**, 305 (2002).
- [107] Downes, A. & Dumas, P. Chemical analysis and optical properties of metallic nanoclusters. *App. Surf. Sci.* **212-213**, 770 (2003).
- [108] Nazin, G., Qiu, X. & Ho, W. Atomic Engineering of Photon Emission with a Scanning Tunneling Microscope. *Phys. Rev. Lett.* **90**, 216110 (2003).
- [109] Jung, T., Himpfel, F., Schlitter, R. & Gimzewski, J. Chemical Information from Scanning Probe Microscopy and Spectroscopy. In Wiesendanger, R. (ed.) *Scanning Probe Microscopy: Analytical Methods* (Springer, 1998).
- [110] Tomitori, M., Terai, H. & Arai, T. Energy spectrum of backscattered electrons excited by a far field emission scanning tunneling microscope with a build-up [111]-oriented W tip. *Appl. Surf. Sci.* **144-145**, 123 (1999).
- [111] Hansen, H. *et al.* Surface waves on NiAl(110). *Phys. Rev. B* **63**, 115421 (2001).
- [112] Blyholder, G. Molecular Orbital View of Chemisorbed Carbon Monoxide. *J. Phys. Chem.* **68**, 2772 (1964).
- [113] McClelland, J., R.E., S., E.C., P. & Celotta, R. Laser-Focused Atomic Deposition. *Science* **262**, 877 (1993).

-
- [114] Wong, K., Johansson, S. & Kasemo, B. Nanofabricated model catalysts. Manufacturing and model studies. *Faraday Discuss.* **105**, 237 (1996).
- [115] Avouris, P. Manipulation of Matter at the Atomic and Molecular Levels. *Acc. Chem. Res.* **28**, 95 (1995).
- [116] Gambardella, P. *et al.* Oscillatory Magnetic Anisotropy in One-Dimensional Atomic Wires. *Phys. Rev. Lett.* **93**, 077203 (2004).
- [117] Neel, N., Kröger, J. & Berndt, R. Fullerene nanowires on a vicinal gold surface. *Appl. Phys. Lett.* **88**, 163101 (2006).
- [118] Brune, H., Giovannini, M., Bromann, K. & Kern, K. Self-organized growth of nanostructure arrays on strain-relief patterns. *Nature* **394**, 451 (1998).
- [119] Becker, C. *et al.* Al₂O₃-films on Ni₃Al(111): a template for nanostructured cluster growth. *New J. Phys.* **4**, 75.1 (2002).
- [120] Silly, F. *et al.* Creation of an Atomic Superlattice by Immersing Metallic Adatoms in a Two-Dimensional Electron Sea. *Phys. Rev. Lett.* **92**, 016101 (2004).
- [121] Kramer, J., Tegenkamp, C. & Pfnür, H. Formation of surface color centers at differently coordinated sites: MgO/Ag(1,1,19). *Phys. Rev. B* **67**, 235401 (2003).
- [122] Benedetti, S. *et al.* Preparation and characterization of MgO stepped surfaces. *Surf. Sci.* **601**, 2636 (2007).
- [123] Ulrich, S., Nilius, N. & Freund, H.-J. Growth of thin alumina films on a vicinal NiAl surface. *Surf. Sci.* **601**, 4603 (2007).
- [124] Kresse, G. *et al.* Structure of the Ultrathin Aluminum Oxide Film on NiAl(110). *Science* **308**, 1440 (2005).
- [125] Schauermann, S., Johánek, V., Laurin, M., Libuda, J. & Freund, H.-J. Interaction of NO with alumina supported palladium model catalysts. *Phys. Chem. Chem. Phys.* **5**, 5139 (2003).
- [126] Sterrer, M., Fischbach, E., Risse, T. & Freund, H.-J. Geometric Characterization of a Singly Charged Oxygen Vacancy on a Single-Crystalline MgO(001) Film by Electron Paramagnetic Resonance Spectroscopy. *Phys. Rev. Lett.* **94**, 186101 (2005).
- [127] Kulawik, M., Nilius, N., Rust, H.-P. & Freund, H.-J. Atomic Structure of Antiphase Domain Boundaries of a Thin Al₂O₃ Film on NiAl(110). *Phys. Rev. Lett.* **91**, 256101 (2003).

- [128] Schmid, M. *et al.* Oxygen-Deficient Line Defects in an Ultrathin Aluminum Oxide Film. *Phys. Rev. Lett.* **97**, 046101 (2006).
- [129] Nilius, N., Kulawik, M., Rust, H.-P. & Freund, H.-J. Defect-induced gap states in Al₂O₃ thin films on NiAl(1 1 0). *Phys. Rev. B* **69**, 121401 (2004).
- [130] Eierdal, L., Besenbacher, F., Lzegsgaard, E. & Stensgaard, I. Interaction of oxygen with Ni(110) studied by scanning tunneling microscopy. *Surf. Sci.* **312**, 31 (1994).
- [131] Hildebrandt, S. *et al.* Real time scanning tunneling microscopy study of the initial stages of oxidation of Ni(111) between 400 and 470 K. *J. Vac. Sci. Technol. A* **18**, 1010 (2000).
- [132] Sykes, E., Han, P. & Weiss, J. Molecule/Metal Surface Interactions Evidenced Quantum Mechanically via Tip-Induced CS₂ Interaction with Friedel Oscillations on Au(111). *J. Phys. Chem. B* **107**, 5016 (2003).
- [133] Pierce, J. & McCarty, K. Self-assembly and dynamics of oxide nanorods on NiAl(110). *Phys. Rev. B* **71**, 125428 (2005).
- [134] Beck, J. *et al.* A New Family of Mesoporous Molecular Sieves Prepared with Liquid Crystal Templates. *J. Am. Chem. Soc.* **114**, 10834 (1992).
- [135] Corma, A. From Microporous to Mesoporous Molecular Sieve Materials and Their Use in Catalysis. *Chem. Rev.* **97**, 2373 (1997).
- [136] Breck, D. *Zeolite Molecular Sieves: Structure, Chemistry, and Use* (Wiley, New York, 1974).
- [137] van Bekkum, H., Flanigen, E. & Jansen, J. (eds.) *Introduction to Zeolite Science and Practice* (Elsevier, Amsterdam, 1991).
- [138] Bhatia, S. *Zeolite Catalysis: Principles and Applications* (CRC Press, Boca Raton, FL, 1990).
- [139] Cheetham, A., Ferey, G. & Loiseau, T. Anorganische Materialien mit offenen Gerüsten. *Angew. Chem.* **111**, 3466 (1999).
- [140] Schroeder, T. *et al.* Epitaxial Growth of SiO₂ on Mo(112). *Surf. Rev. Lett.* **7**, 7 (2000).
- [141] Stacchiola, D. *et al.* Synthese und Struktur eines ultradünnen Alumosilicatfilm. *Angew. Chem.* **118**, 7798 (2006).
- [142] Kim, Y., Wei, T. & Goodman, D. Identification of Defect Sites on SiO₂ Thin Films Grown on Mo(112). *Langmuir* **19**, 354 (2003).

-
- [143] Min, B., Wallace, W. & Goodman, D. Synthesis of a Sinter-Resistant, Mixed-Oxide Support for Au Nanoclusters. *J. Phys. Chem. B* **108**, 14609 (2004).
- [144] Weissenrieder, J. *et al.* Atomic Structure of a Thin Silica Film on a Mo(112) Substrate: A Two-Dimensional Network of SiO₄ Tetrahedra. *Phys. Rev. Lett.* **95**, 076103 (2005).
- [145] Giordano, L., Del Vitto, A. & Pacchioni, G. Au and Pd atoms adsorbed on pure and Ti-doped SiO₂/Mo(112) films. *J. Chem. Phys.* **124**, 034701 (2006).
- [146] Ulrich, S. *et al.* Evidence for a Size-Selective Adsorption Mechanism on Oxide Surfaces: Pd and Au atoms on SiO₂/Mo(112). *Chem. Phys. Chem.* **9**, 1367 (2008).
- [147] Giorgi, J., Schröder, T., Bäumer, M. & Freund, H.-J. Study of CO adsorption on crystalline-silica-supported palladium particles. *Surf. Sci. Lett.* **498**, L71 (2002).
- [148] Chen, M. & Goodman, D. The structure of monolayer SiO₂ on Mo(112): A 2-D [Si–O–Si] network or isolated [SiO₄] units? *Surf. Sci.* **600**, L255 (2006).
- [149] Kaya, S. *et al.* On the geometrical and electronic structure of an ultra-thin crystalline silica film grown on Mo(112). *Surf. Sci.* **601**, 4849 (2007).
- [150] Seifert, J., Blauth, D. & Winter, H. Evidence for 2D-Network Structure of Monolayer Silica Film on Mo(112). *Phys. Rev. Lett.* **103**, 017601 (2009).
- [151] Sierka, M. *et al.* Interplay between theory and experiment in the quest for silica with reduced dimensionality grown on a Mo(112) surface. *Chem. Phys. Lett.* **424**, 115 (2006).
- [152] Giordano, L., Ricci, D., Pacchioni, G. & Ugliengo, P. Structure and vibrational spectra of crystalline SiO₂ ultra-thin films on Mo(112). *Surf. Sci.* **584**, 225 (2005).
- [153] Xu, X. & Goodman, D. The preparation and characterization of ultra-thin silicon-dioxide films on a Mo(110) surface. *Surf. Sci.* **282**, 323 (1993).
- [154] Wallace, W., Min, B. & Goodman, D. The stabilization of supported gold clusters by surface defects. *J. Mol. Catal. A: Chem.* **228**, 3 (2005).
- [155] Kaya, S. *Structural and Catalytic Investigations on Vanadium Oxide Nanoparticles Supported on Silica Films Grown on a Mo(112) Substrate*. Ph.D. thesis, Humboldt-Universität zu Berlin (2007).
- [156] Moulder, J., Sticke, W., Sobol, P. & Bomben, K. *Handbook of X-ray Photoelectron Spectroscopy* (Perkin Elmer Corporation, 1992).

- [157] Grunthaner, F. *et al.* Local atomic and electronic structure of oxide/GaAs and SiO₂/Si interfaces using high-resolution XPS. *J. Vac. Sci. Technol.* **16**, 1443 (1979).
- [158] Freysoldt, C., Rinke, P. & Scheffler, M. Ultrathin Oxides: Bulk-Oxide-Like Model Surfaces or Unique Films? *Phys. Rev. Lett.* **99**, 086101 (2007).
- [159] Ricci, D. & Pacchioni, G. Structure of ultrathin crystalline SiO₂ films on Mo(112). *Phys. Rev. B* **69**, 161307 (2004).
- [160] Schröder, T., Giorgi, J., Bäumer, M. & Freund, H.-J. Morphological and electronic properties of ultrathin crystalline silica epilayers on a Mo(112) substrate. *Phys. Rev. B* **66**, 165422 (2002).
- [161] Wendt, S. *et al.* Electronic and vibrational properties of ultrathin SiO₂ films grown on Mo(112). *Phys. Rev. B* **72**, 115409 (2005).
- [162] Jerratsch, J.-F. *et al.* Lithium incorporated into a silica thin film: Scanning tunneling microscopy and density functional theory. *Phys. Rev. B* **80**, 245423 (2009).
- [163] Giordano, L., Cinquini, F. & Pacchioni, G. Tuning the surface metal work function by deposition of ultrathin oxide films: Density functional calculations. *Phys. Rev. B* **73**, 045414 (2005).
- [164] Kiguchi, M. & Saiki, K. Metal induced gap-states at insulator/metal interfaces. *e.-J. Surf. Sci. Nanotech.* **2**, 191 (2004).
- [165] Perdew, J. *et al.* Atoms, molecules, solids, and surfaces: Applications of the generalized gradient approximation for exchange and correlation. *Phys. Rev. B* **46**, 6671 (1992).
- [166] Kresse, G. & Hafner, J. *Ab initio* molecular dynamics for liquid metals. *Phys. Rev. B* **47**, 558 (1993).
- [167] Kresse, G. & Furthmüller, J. Efficient iterative schemes for *ab initio* total-energy calculations using a plane-wave basis set. *Phys. Rev. B* **54**, 11169 (1996).
- [168] Blöchl, P. Projector augmented-wave method. *Phys. Rev. B* **50**, 17953 (1994).
- [169] Ulrich, S. *et al.* Realization of an Atomic Sieve: Silica on Mo(112). *Surf. Sci.* **603**, 1145 (2009).
- [170] Linde, R. (ed.) *Handbook of Chemistry and Physics* (CRC Press, Boca Raton, FL, 1998).

- [171] Pacchioni, G., Giordano, L. & Baistrocchi, M. Charging of Metal Atoms on Ultrathin MgO/Mo(100) Films. *Phys. Rev. Lett.* **94**, 226104 (2005).
- [172] Nilius, N. *et al.* Counting Electrons Transferred through a Thin Alumina Film into Au Chains. *Phys. Rev. Lett.* **100**, 096802 (2008).
- [173] Moore, C. (ed.) *Atomic Energy Levels* (US-Gov. Print Office, Washington, 1952).
- [174] Lu, J. *et al.* Low temperature CO induced growth of Pd supported on a monolayer silica film . *Surf. Sci.* **600**, L153 (2006).
- [175] Wang, J. & Lunsford, J. Characterization of [Li+O] centers in lithium-doped magnesium oxide catalysts. *J. Phys. Chem.* **90**, 5883 (1986).
- [176] Wu, M., Truong, C. & Goodman, D. Electron-energy-loss-spectroscopy studies of thermally generated defects in pure and lithium-doped MgO(100) films on Mo(100). *Phys. Rev. B* **46**, 12688 (1992).
- [177] Sterrer, M. Interaction of Gold Clusters with Color Centers on MgO(001) Films. *Angew. Chem. Int. Ed.* **45**, 2630 (2006).
- [178] Ulrich, S. *et al.* Tailoring the Adsorption Properties of Inert Oxide Films by Inserting Controlled Anchor Sites. *Phys. Rev. Lett.* **102**, 016102 (2009).
- [179] Löffler, D. *et al.* Growth and Structure of Crystalline Silica Sheet on Ru(0001). *Phys. Rev. Lett.* **105**, 146104 (2010).
- [180] Martinez, U. *et al.* Tailoring the Interaction Strength between Gold Particles and Silica Thin Films via Work Function Control. *Phys. Rev. Lett.* **103**, 056801 (2009).
- [181] Jerratsch, J.-F. *et al.* Stabilizing Monomeric Iron Species in a Porous Silica/Mo(112) Film. *ACS Nano* **4**, 863 (2010).
- [182] Horcas, I. *et al.* WSXM: A software for scanning probe microscopy and a tool for nanotechnology. *Rev. Sci. Instrum.* **78**, 013705 (2007).

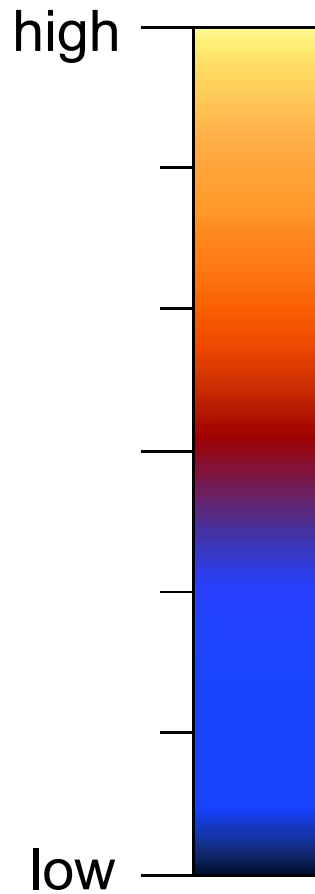
Appendix

1 List of Abbreviations

Å	–	Ångstrom
AES	–	Auger electron spectroscopy
CCT	–	Constant current tunneling
CM	–	Conductance map
CPS	–	Counts per second
DSP	–	Digital signal processor
ECD	–	Eddy-current damping
FWHM	–	Full width half maximum
HMA	–	Hemispherical mirror analyzer
IPES	–	Inverse photo-electron spectroscopy
IRAS	–	Infrared reflection absorption spectroscopy
ISS	–	Ion scattering spectroscopy
LDOS	–	Local density of states
LEED	–	Low-energy electron diffraction
LEEM	–	Low-energy electron microscopy
MBE	–	Molecular beam epitaxy
MIES	–	Metastable impact electron spectroscopy
MIGS	–	Metal-induced gap states
ML	–	Monolayer
NEXAFS	–	Near edge X-ray adsorption fine structure
OFHC	–	Oxygen-free high conductivity
SAM	–	Scanning Auger microscope
SEM	–	Scanning electron microscope
SPELS	–	Scanning probe energy loss spectroscopy
STM	–	Scanning tunneling microscope
TMP	–	Turbo molecular pump
UHV	–	Ultra-high vacuum
UPS	–	Ultraviolet photo-electron spectroscopy
UV	–	Ultraviolet
XPS	–	X-ray photo-electron spectroscopy

2 Conductance Maps Color Scheme

All STM images and conductance-maps in this work have been processed with WSxM [182]



Color-to-signal association of the conductance maps. For each data-set, the map with the largest signal-range served as reference and was by default adjusted to make use of the full color-scale.

3 Publications

The following parts of this work have been published:

Chapter 4

- *Growth of thin alumina films on a vicinal NiAl surface*, S.Ulrich, N. Nilius and H.-J. Freund. *Surf. Sci.*, 601, 4603-4607, 2007.

Chapter 5

- *Absorption of Au and Pd atoms on thin SiO₂ films*, M Baron, D. Stacchiola, S. Ulrich, N. Nilius, S. Shaikhutdinov and H.-J. Freund. *J. Phys. Chem. C*, 112, 3405-3409, 2008.
- *Evidence for a Size-Selective Adsorption Mechanism on Oxide Surfaces: Pd and Au atoms on SiO₂/Mo(112)*, S. Ulrich, N. Nilius, H.-J. Freund, U. Martinez, L. Giordano and G. Pacchioni. *Chem. Phys. Chem.*, 9, 1367-1370, 2008.
- *Realization of an atomic sieve: Silica on Mo(112)*, S.Ulrich, N. Nilius, H.-J. Freund, U. Martinez, L. Giordano and G. Pacchioni. *Surf. Sci.* 603, 093007, 2009

Chapter 6

- *Tailoring the Adsorption Properties of Inert Oxide Films by Inserting Controlled Anchor Sites*, S.Ulrich, N. Nilius, H.-J. Freund, U. Martinez, L. Giordano and G. Pacchioni. *Phys. Rev. Lett.* 102, 016102, 2009

4 Danksagung

Ganz herzlich möchte ich mich bei allen bedanken, die mir diese Arbeit ermöglicht haben und deren Unterstützung maßgeblich zum Erfolg beigetragen hat:

- Herrn Prof. Dr. Hans-Joachim Freund für die Auswahl des Themas und die Bereitstellung der Mittel, die für den Erfolg dieses Projektes erforderlich waren. Vielen Dank für die Möglichkeit, in dieser herausragenden Forschungseinrichtung mitarbeiten zu dürfen.
- Herrn Prof. Dr. Mario Dähne für die Bereitschaft zur Begutachtung dieser Arbeit.
- Herrn Dr. habil. Niklas Nilius ist mein aufrichtigster Dank geschuldet. Die aufmerksame Betreuung und geduldige Anleitung während aller Phasen dieser Arbeit waren wesentlich für das Gelingen. So habe ich fortwährend von ihrem Wissen und der Erfahrung profitieren können. Auch möchte ich die gute Atmosphäre in der Arbeitsgruppe loben, die den Laboralltag sehr bereichert hat.
- Dr. Umberto Martinez, Dr. Livia Giordano und Prof. Dr. Gianfranco Pacchioni vom Dipartimento di Scienza dei Materiali der Università di Milano-Bicocca. Mille grazie für die Zusammenarbeit und die Bereitstellung der Modellrechnungen zum Thema: Absorption von Metallatomen auf einlagiger Silica.
- Mein Dank richtet sich auch an Dr. Sarp Kaya, der mich großzügig mit detaillierten Informationen zur Synthese der Silica Filme versorgt hat.
- Den Mitgliedern der AG Nilius: Dr. Hadj-Mohammed Benija, Dr. Jan-Frederik Jerratsch, Dr. Phillip Myrach und Dr. Xiao Lin, für die angenehme Zusammenarbeit.
- Der Mechanischen Werkstätten des Fritz-Haber Institutes, insbesondere Herrn Horst Schwäricke und Herrn Hans-Peter Vogelgesang, die die für den Aufbau des neuen Rastertunnel-Mikroskops erforderlichen Teile schnell und in hervorragender Qualität hergestellt haben.
- Herrn Georg Heyne, Leiter des Elektroniklabors des FHI, der mir mit Geduld und Sorgfalt vermittelte, was beim Einrichten einer hochwertigen Messelektronik zu beachten ist.
- Meiner Frau Dr. Elizabeth Kattner-Ulrich, die mich über alle Maßen hinaus unterstützt und ermutigt hat.

Schlussendlich liegt es mir am Herzen, meine Mutter Helga Ulrich (*26.01.1937 - †10.06.2007) zu ehren. Sie hat mir ermöglicht, eine gute Ausbildung zu erhalten und mich gelehrt, die richtigen Entscheidungen zu treffen.

5 Selbständigkeitserklärung

Hiermit erkläre ich, die vorliegende Arbeit ohne fremde Hilfe verfaßt und ausschließlich die aufgeführte Literatur und die angegebenen Hilfsmittel verwandt zu haben.

Stefan Ulrich
Juli 2011